Nonlinear optical response: New *in silico* Methods and Features

by

Vladimir A. Goncharov

Dissertation

Submitted to the Faculty of the
Graduate School of Vanderbilt University
in partial fulfillment of the requirements
for the degree of

DOCTOR OF PHILOSOPHY

IN

PHYSICS

MAY 2014

NASHVILLE, TENNESSEE

APPROVED:

KALMAN VARGA, PHD

ANDREAS BERLIND, PHD

DAVID ERNST, PHD

RICHARD HAGLUND, PHD

SAIT UMAR, PHD

To Olga and Irene.

ACKNOWLEDGEMENTS

A number of people have contributed to my education over the past years, and I am grateful to them all. Let me first thank my undergraduate adviser Vladimir Rosenhaus. Although many years have past since we actively worked together, your scientific style and inquisitive spirit still inspire me. Meeting with Andreas Berlind almost turned me into an astrophysicist. Your lectures on the Large Structure of Universe were engaging and illuminating. Thank you for being on my dissertation committee. Your kindness and invariable support will not be forgotten. I will definitely miss the long conversations with Dave Ernst and the cheerful mood that comes with it. Thank you Dave for your eternal optimism. Thank you also for genuinely caring for the role of women and minorities in science, and more generally for all who do not have, what others take for granted. I also would like to thank Sait Umar for willingness to answer questions, give technical advice and support during the committee meetings. I think that it become more difficult for a student to ”lose direction” in the physics graduate program in the past few years. The program become better organized, with greater conformance to the official university rules and at the same more humane and inclusive. I attribute these changes in large part to Julia Velkovska, and hope that she will continue to be the director of the physics graduate program for many more years. Thank you Julia for sincerely caring for your students. The late night discussions and occasional outings with Thom Weiler are not easily forgotten. Your lively lectures on the General Relativity have kept the snooze at bay. Your phrase ” ... and now for this simple result you should have equally simple theory...” have been a guide for me ever since. Thank you Thom. I would also like to thank Kirill Bolotin, Sergey Avanesyan, Shane Hutson, Volker Oberacker, Soc Pantelides, Don Pickert and all others who one way or another participated in my education. Finally, I thank Olga and Irene. This work is dedicated to you.

LIST OF TABLES

LIST OF FIGURES

CONTENTS

Chapter 1

INTRODUCTION

1.1 Motivation

Most intriguing developments in modern nonlinear optics are related to systems with extraordinary high nonlinearities. In experiments with Rydberg Electromagnetically Induced Transparency (EIT) value of the optical Kerr nonlinear coefficient exceeds the conventional by a factor of 10^{12} [13, 14, 15]. Although exotic systems of ultra-cold atoms can not be of practical use, the EIT experiments stimulate engineers, chemists and material scientists who are working on finding ways to increase nonlinearity of known optical materials and creating new nonlinear optical materials.

Optical materials with enhanced nonlinearity are crucial for reducing size of electrooptical modulators and switches down to sub-micrometer size, and developing new, all optical processors and decoders [16, 17, 18, 19, 20, 21, 22, 23].

Main requirements for the new generation of optical processors are [24, 25]:

- Reduced operational voltage for reduced energy per bit processed.
- Reduced size to enable "on the chip" integration with conventional electronic processors.
- Ultra fast response to enable terahertz and all-optical processing with characteristic response time $\tau \sim 10^{-13}$ s.

Although there is a variety of designs, mechanism of a typical optical modulator depends on a phase shift $\Delta\phi$ which is related to induced change in refractive index $\Delta n(\lambda)$ (taken at wavelength λ) and the length of active wave guide L, where interaction occurs:

$$\Delta\phi = \frac{\pi\,\Delta n(\lambda) L}{\lambda}. \tag{1.1}$$

Change in refractive index is proportional to nonlinearity (nonlinear refractive index) n_2 and square of electric field $|E|^2$: $\Delta n = 2n_2|E|^2$ [26]. Another, more general way of accessing nonlinear characteristic of optical switch is the nonlinear waveguide parameter γ_A [27, 28, 29]:

$$\gamma_A = \frac{2\,\pi\,n_2}{\lambda\,A}, \tag{1.2}$$

where A is an effective area (footprint) where the interaction between photons and material occurs. Greater efficiency to which larger numerical values of γ_A correspond, require larger nonlinearity, and smaller size. It naturally follows from above that increasing nonlinearity is the direct way of reducing the size of optical processor and improving its effectiveness. At the same time, increasing nonlinearity of material normally leads to reducing operational electric field because nonlinear response is proportional to the nonlinearity and the square of electric field. Thus, two key characteristics are directly related to enhanced nonlinearity of optical material. The requirement of ultra-fast response could be superfluously satisfied if the chief mechanism of nonlinear response of the device is purely electronic, because its characteristic response time is on the order of a femto second $\tau_{electronic} \sim 10^{-15}$ [26]. Unfortunately, electronic nonlinear response in ordinary materials is relatively weak, in fact weaker by two orders of magnitude then response involving molecular re-orientation [26].

Thus, achieving all three key requirements is not a trivial task. The need for new nonlinear optical materials could be further illuminated if we compare nonlinear coefficients of conventional materials with the most advanced specimens and with what is actually needed for a hypothetical optical processor that could compete with modern integrated circuit. Let us assume that an all optical device could be constructed with characteristic size L=325 nm, operating at λ=L and pump intensity I$\sim 10^{12}$ (W/m^2). This will imply electric field strength $|E| \sim 10^{-3}$ (V/Å) and corresponding potential of $\sim$ 1 Volt. Modulation with maximum phase shift of $\Delta\phi = \frac{\pi}{2}$ will require change in refractive index $\Delta n \sim 1$, and corresponds to optical nonlinearity $n_2 \sim 10^{-12}$ (m^2/W). Conventional materials have n_2 nonlinearity within 10^{-23} to 10^{-20} (m^2/W). For example ordinary air has $n_2 = 5.0 \times 10^{-23}$ (m^2/W) and Al_2O_3 has 2.9×10^{-20} (m^2/W).

Specialized optical materials such as SF-59 glass (Schott) and As_2S_3 glass have $n_2 = 3.3 \times 10^{-19}$ (m^2/W) and $3.0 \times 10^{-17}\,(m^2/W)$ respectively. However, the highest n_2 currently measured in nanostructured plasmonic (meta)materials, such as patterned gold nanoparticles in glass $n_2 = 2.6 \times 10^{-14}\,(m^2/W)$ [26]. Therefore, there is both the need and the room to increase the nonlinearity of optical materials by factor of $\times 10^2$ to $\times 10^5$ [1].

The work presented in this thesis is aimed at developing new computational framework that can simplify and speed up the search for new nonlinear optical materials, and facilitate study of light-matter interactions from quantum mechanical principles. The work currently addresses two aspects. One is realistic modeling of interaction of light and material. The other is extraction of response functions from these simulations. Most of the nonlinear optical phenomena, such as Kerr effect, Two Photon Absorption (TPA), optical rectification (OR), Intensity Dependent Refractive Index (IDRI) and Second and Third Harmonic Generation (SHG and THG) have corresponding response functions. Optical response functions have many names: susceptibilities, polarizabilities, both linear and nonlinear, and hyperpolarizabilities. They provide a quantitative measure for the response of matter to electromagnetic field, enabling evaluation of material under study for prospective applications. If response function is known, then it can be used to model relevant processes that go beyond initial "experiment" from which it was obtained. In the next chapter we introduce basic terminology and highlight utility of the optical response functions.

1.2 Nonlinear optical phenomena in terms of response functions

The equation describing propagation of a monochromatic wave

$$\vec{E}(\vec{r},t) = \vec{E}(\vec{r})e^{\imath\omega t} + c.c. \tag{1.3}$$

---

[1] We have not discussed second order nonlinear materials that are utilized in Pockels effect based devices primarily because all-optical processing is not feasible in them. However, the situation with these materials is similar to what has been described: there is two to five orders of magnitude gap in nonlinearity that needs to be crossed in order to satisfy requirements of modern optoelectronics applications. In addition, the second order materials with the highest nonlinearity are organic polymers [21] that overwhelmingly suffer from thermal stability problems [30].

with wave number $k^2(\omega) = \frac{n(\omega)\omega}{c}$ in media with refractive index $n(\omega)$ and a time dependent source

$$\vec{P}^{(m)}(\vec{r}, t) = \vec{P}^{(m)}(\omega)e^{\imath\omega t - \imath\vec{k}\cdot\vec{r}} + c.c. \tag{1.4}$$

could be written as:

$$\nabla^2\vec{E}(\vec{r}) + k^2(\omega)\vec{E}(\vec{r}) = -4\pi\frac{\omega^2}{c^2}\vec{P}^{(m)}(\omega)e^{-\imath\vec{k}\cdot\vec{r}}. \tag{1.5}$$

Let the source be m^{th} term in decomposition of total polarization in powers of electric field $\vec{E}'$:

$$\vec{P}^{total}(\omega) = \sum_{i=1}^{N_{max}} \vec{P}^{(i)}(\omega, (\vec{E}')^i). \tag{1.6}$$

Then, equation (1.5) will be related to propagation of nonlinear polarization wave of m^{th} order. Its solution with appropriate boundary conditions gives mathematical description of specific nonlinear process of m^{th} order. The source term is the nonlinear polarization, which is expressed in terms of response functions. For monochromatic electric fields it could be written as:

$$P_i^{(m)} = \sum_{j\ldots k} \chi_{ij\ldots k}^{(m)} E_j \ldots E_k. \tag{1.7}$$

The coefficients $\chi_{ij\ldots k}^{(m)}$ are m^{th} order response functions, or susceptibilities. Their tensor nature plays key role in determining propagation of nonlinear wave. For example, in case of SHG, which is a second order process, orientational dependence of reflected second harmonic from crystal with $\overline{4}3m$ symmetry is found from [33, 34]

$$P_x^{(2)}(2\omega) = \chi_{xyz}^{(2)} E_y E_z,$$

$$P_y^{(2)}(2\omega) = \chi_{yzx}^{(2)} E_z E_x,$$

$$P_z^{(2)}(2\omega) = \chi_{zxy}^{(2)} E_x E_y.$$

When the electric vector is polarized along [111] crystal axis, all P-components are equal and P is in the same direction as E. When E is along [100], y and z components are absent and P is zero. Similarly along the [010] direction. For [011] direction, P has only x-component.

Magnitude of some nonlinear effects could be easily evaluated if corresponding susceptibility is known. For example, in case of IDRI, refractive index is calculated from third order susceptibility taken at fundamental frequency ω of propagating wave:

$$n(\omega) = n_0 + \frac{12\pi^2}{n_0^2 c}\chi^{(3)}(\omega)\, I,$$

where I is intensity of the wave, and n_0 is the linear refractive index.

In short, the main message of this section is that response functions are a compact way of describing key properties of many nonlinear optical processes and materials.

1.3 Adiabatic Local Density Approximation

Since the optical susceptibilities describe the light-matter interactions, their realistic evaluation at certain point requires solution of Schrödinger equation for a multi-electron system. All important results of this work were obtained by using time evolution of wavefunction under action of time dependent Hamiltonian in the Adiabatic Local Density Approximation (ALDA)[2]. In this approximation, the electron-electron interactions are described by effective density dependent potential $V_{eff}(\vec{r}, \rho(\vec{r}, t))$. The electronic density ρ is calculated from single particle orbitals ϕ:

$$\rho(\vec{r}, t) = \sum_{i=1}^{N} \phi_i^*(\vec{r}, t)\phi_i(\vec{r}, t), \tag{1.8}$$

where N - is a number of electrons. ALDA involves three important approximations. First, it represents multi electron wave function as a determinant composed of single particle orbitals. This step reduces electron-electron interactions to two parts, one of them is a local, density dependent Hartree potential $V_H(\vec{r}, t)$:

$$V_H(\vec{r}, \rho(\vec{r}, t)) = \int d^3r' \frac{\rho(\vec{r'}, t)}{|\vec{r} - \vec{r'}|}. \tag{1.9}$$

---

[2] A number of textbooks has been published on this topic [35, 36, 37]. In addition, appendix A contains more details.

Second, the exchange interaction is approximated by another local, density dependent potential $V_x(\vec{r}, \rho(\vec{r}, t))$:

$$V_x(\vec{r}, \rho(\vec{r}, t)) = -\frac{4}{3} C_x \rho(\vec{r}, t)^{\frac{1}{3}}, \tag{1.10}$$

where C_x is a constant. Third, a gamut of all correlations beyond spin exchange are represented by yet another local, density dependent correlation potential $V_c(\vec{r}, \rho(\vec{r}, t))$. This step modifies the first step in a way that the wavefunction now captures interactions that are not accessible to a single determinant states even with the exact exchange. As the result, electron-electron interactions in ALDA are represented by a sum of local density dependent potentials: Hartree and Exchange-Correlation.

$$V_{eff}(\vec{r}, t) = V_H(\vec{r}, \rho(\vec{r}, t)) + V_{xc}(\vec{r}, \rho(\vec{r}, t)). \tag{1.11}$$

Above, the exchange and correlation potentials are written as a single potential $V_{xc} = V_x + V_c$. The theoretical foundations of ALDA are rooted in Time Dependent Density Functional Theory (TDDFT) [38]. Two common variants of ALDA exchange-correlation potentials are based on works of J. P. Perdew and Alex Zunger [39], and S. H. Vosko, L. Wilk, and M. Nusair [40]. The potentials are named after them and are referred below as PZ and VWN. Next section introduces solution of time-dependent Schrödinger equation.

1.4 Real-Time Evolution

In order to obtain explicitly time dependent wavefunction on the level of TDDFT, one needs to solve time dependent single particle Schrödinger equation for a time-dependent Hamiltonian with external potential $V_{ext}(\vec{r}, t)$:

$$\hat{H}(t) = -\frac{\hbar^2}{2\, m_e} \Delta + V_{eff}(\vec{r}, t) + V_{ext}(\vec{r}, t). \tag{1.12}$$

The external potential $V_{ext}(\vec{r}, t)$ is a sum of two potentials. One represents interaction of electrons with external electromagnetic field $\vec{E}(\vec{r}, t)$ [3], and the other Coulomb

---

[3] Generally, it is a multipole interaction, but here, as later will be shown, it is taken in dipole approximation.

interaction of electrons and nuclei $V_{ion}(\vec{r},t)$. Calculations start with obtaining the ground state of the system. It is accomplished by solving the system of Kohn Sham equations:

$$\hat{H}(t_0)|\phi_i(t_0)\rangle = E_i|\phi_i(t_0)\rangle. \tag{1.13}$$

Starting from the ground state, orbitals are evolved in time under the action of the evolution operator $\hat{U}$:

$$|\phi_i(t)\rangle = \hat{U}(t,t_0)|\phi_i(t_0)\rangle. \tag{1.14}$$

The evolution operator is defined as time ordered exponential operator:

$$\begin{aligned} \hat{U}(t,t_0) = \hat{T}\exp(\frac{-i}{\hbar}\int_{t_0}^{t}\hat{H}(t')dt') = \\ = \sum_{n=0}^{\infty}\frac{(-i)^n}{\hbar^n}\frac{1}{n!}\int_{t_0}^{t}dt_1\ldots\int_{t_0}^{t}dt_n\hat{T}(\hat{H}(t_1)\ldots\hat{H}(t_n)) \end{aligned} \tag{1.15}$$

To utilize the multiplicative property $\hat{U}(t_2,t_0) = \hat{U}(t_2,t_1)\hat{U}(t_1,t_0)$ the finite time interval is broken into N_{time} small segments δt. The evolution operator becomes a product of operators applied at each $t_i + \delta t$:

$$\hat{U}(t,t_1) = \prod_{i=1}^{N_{time}}\hat{U}(t_i+\delta t,t_i). \tag{1.16}$$

Each δt corresponds to an evolution iteration at which Hamiltonian is taken constant with a value at that instant. Integral turns into a simple product:

$$\int_{t_i}^{t_i+\delta t}\hat{H}(t_i)dt \;\rightarrow\; \hat{H}(t_i)\delta t.$$

In addition, the infinite sum is truncated at some N_{Taylor} turning the exponential into a Taylor polynomial. Therefore, the evolution operator for "physically infinitesimal" segment δt becomes:

$$\hat{U}(t_i+\delta t,t_i) = \sum_{n=0}^{N_{Taylor}}\frac{1}{n!}\left(\frac{-i\,\hat{H}(t_i)\,\delta t}{\hbar}\right)^n. \tag{1.17}$$

There is a number of other representations for evolution operator including the Crank-Nicolson time propagation [41, 42]. With this section we conclude technical introduction. Additional background information is provided in Appendix A.

1.5 Overview

Chapter 2 gives detailed description of three different methods for extracting nonlinear susceptibilities from time dependent polarization. The methods are universal in a sense that they are applicable to atoms, molecules, nano clusters and solids. Method I is an original development by the author. It was used to calculate third order susceptibilities in crystal Silicon and Carbon diamond and appears in V.A. Goncharov, J.Chem.Phys. **139**, 084104 (2013). Method III is an original development by the author. It was used as one of alternative methods in calculations of hyperpolarizabilities of atoms and molecules. It appears in V.A. Goncharov and K. Varga, J.Chem.Phys. **137**, 094111 (2012). Method II has been used for calculations of susceptibilities of silver clusters and fullerenes. It is an original development by the author and has not appeared elsewhere. Sections 2 and 4 contain analysis of locality and polarization response of a model molecule and put forth conjecture that non-resonant nonlinear optical response under excitation with ultrashort (10-12 fs) Gaussian shaped electric pulses is identical to excitation with monochromatic pulse. This finding simplifies formalism and consequently analysis of nonlinear response and calculation of susceptibilities. It also advances a conjecture that decomposition of total polarization into a polynomial of electric fields is exact for quasi-monochromatic excitations for certain systems. The cases when the conjecture holds true are named Regular nonlinear response (RNR). This material has not appeared elsewhere.

Chapter 3 contains comparative tests of Method of Takimoto et al [31], its variant in frequency space, Method III and calculations based on Density Functional Perturbation theory. Tests were done on 3 noble gases and 9 molecules of different size and complexity for which hyperpolarizabilities were known from experiment. The chapter appears as part of V.A. Goncharov and K. Varga, J.Chem.Phys. **137**, 094111 (2012).

Chapter 4 is an application of the methods developed in chapter 2 to silver clusters.

Besides analysis of third order response it classifies the charge density excitations in Ag_{32} cluster and proposes mechanisms of contribution of these excitations to nonlinear response. In addition, it addresses question of transition to metallicity in large clusters. This material has not appeared elsewhere.

In chapter 5 author makes an attempt to enhance third order response of C_{60} fullerene. Based on insight from chapter 4, he adds a silver dimer into interior of the fullerene. The analysis of nonlinear response shows that enhancement exceeds a simple sum of the nonlinear response of separate molecules. Following charge density analysis, the enhancement is attributed to stabilization of electronic excitations of Ag_2 electrons inside the carbon cage of the fullerene. This material has not appeared elsewhere.

Chapter 6 is an application of the methods to crystalline solids. The methods of propagation and calculation of polarization are notably different from finite systems such as molecules and based on coupled Maxwell-Schrödinger dynamics described by K. Yabana,G. Bertch et. al [32]. It contains first *ab initio* calculations of third order susceptibilities in a semiconductor. Details specific to calculation of polarizability are presented and results are compared to experimental data. The material forms bulk of V.A. Goncharov, J.Chem.Phys. **139**, 084104 (2013).

Chapter 7 has been published as V.A. Goncharov and K. Varga, Phys. Rev. B, **83**, 035118(2011). It describes implementation of Domain Decomposition Approach within Real Time TDDFT (RT-TDDFT) and illustrates the method with applications to molecules and nanostructure.

Chapter 2

RESPONSE FUNCTIONS FROM REAL TIME TDDFT

2.1 Method I: Reduction to a linear system

The key characteristic of n^{th} order non-linear optical response is that it supplies a contribution to total polarization that depends on n^{th} power of electric field $\vec{E}^n$:

$$P_i = \sum_n \sum_{k \dots m} P^{(n)}_{ik \dots m}(\vec{E}^n). \tag{2.1}$$

The extraction procedure for $\chi^{(n)}$ in general would contain steps to decompose total polarization into sum of different orders (2.1) and then deduce $\chi^{(n)}$ from corresponding orders of nonlinear polarization $P^{(n)}$. The n^{th} order response in frequency domain takes the following form:

$$P^{(n)}_{ik \dots m}(\omega) = \mathcal{K} \int \chi^{(n)}_{ik \dots m}(-\omega;\, \omega_1, \dots, \omega - \sum_{j=1}^{n-1} \omega_j)\, E_k(\omega_1)\, \dots\, E_m(\omega - \sum_{j=1}^{n-1} \omega_j)\, d\omega_1 \dots d\omega_{n-1}. \tag{2.2}$$

$\mathcal{K}$ is a factor that depends both on order and specific non-linear process. Tables (2.1) and (2.2) list these factors for several common processes.

Table 2.1: $\mathcal{K}$-factors for third order processes: $\mathcal{K} = \frac{D}{2^l (2\pi)^m}$. D is number of non-equivalent permutations of inputs frequencies, m is one less than number of non-zero input frequencies, l is one if $\omega_\sigma = 0$, zero otherwise.

D	m	l	$(2\pi)^{-m}$	$-\omega_\sigma$	ω_1	ω_2	ω_3	$\mathcal{K}$	Process
1	0	1	1	0	0	0	0	1	static
6	1	1	$\frac{1}{2\pi}$	0	0	$-\omega$	ω	$\frac{3}{2\pi}$	
3	0	0	1	$-\omega$	0	0	ω	3	Kerr
3	2	0	$\frac{1}{4\pi^2}$	$-\omega$	ω	ω	-ω	$\frac{3}{4\pi^2}$	IDRI/TPA
1	2	0	$\frac{1}{4\pi^2}$	-3ω	ω	ω	ω	$\frac{1}{4\pi^2}$	THG
6	2	0	$\frac{1}{4\pi^2}$	$-\sum_i \omega_i$	ω_1	ω_2	ω_3	$\frac{3}{2\pi^2}$	$\omega_1 \neq \omega_2 \neq \omega_3$

Table 2.2: $\mathcal{K}$-factors for second order processes: $\mathcal{K} = \frac{D}{2^l(2\pi)^m}$. D is a number of non-equivalent permutations of inputs frequencies, m is one less than number of non-zero input frequencies, l is one if $\omega_\sigma = 0$, zero otherwise.

D	m	l	$(2\pi)^{-m}$	$-\omega_\sigma$	ω_1	ω_2	$\mathcal{K}$	Process
2	1	1	$\frac{1}{2\pi}$	0	$-\omega$	ω	$\frac{1}{2\pi}$	OR
2	0	0	1	$-\omega$	0	ω	2	Pokels
1	1	0	$\frac{1}{2\pi}$	-2ω	ω	ω	$\frac{1}{2\pi}$	SHG
2	1	0	$\frac{1}{2\pi}$	$-\sum_i \omega_i$	ω_1	ω_2	$\frac{1}{\pi}$	$\omega_1 \neq \omega_2$

The arguments of $\chi^{(n)}$ are customarily written as to yield a formal zero sum $-\omega + \omega_1 + \ldots + \omega_{n-1} + \omega - \sum_{j=1}^{n-1} \omega_j = 0$ to indicate (and enforce) the conservation of energy. Alternatively, a delta-function may be employed [1].

2.1.1 Time dependent density

The starting point is the modeling of interaction of electromagnetic field and a system of interest. The goal is to calculate a realistic density and polarization response to a model laser pulse. Time dependent density is obtained from time dependent Kohn -Sham orbitals that are propagated using Real-Time TDDFT method [2]:

$$\rho(\vec{r}, t) = \sum_k f(k) \phi_k^*(\vec{r}, t) \phi_k(\vec{r}, t), \tag{2.3}$$

where $f(k)$ - occupation numbers. Hamiltonian $\hat{H}(t)$ contains time dependent potential representing electric dipole interaction of electrons with electric field of external electromagnetic wave.

$$V_{ext}(t) = -e\vec{E}(t) \cdot \vec{r} \tag{2.4}$$

with

$$\vec{E}(t) = (\lambda \hat{i} + \mu \hat{j} + \nu \hat{k}) \sin(\omega t) e^{-\frac{(t-t_0)^2}{\sigma^2}}, \tag{2.5}$$

---

[1] See Appendix B for details

[2] Additional details are presented in chapter 3.

where $\lambda, \mu, \nu \in \mathbf{R}$ are amplitudes of corresponding Cartesian components of $\vec{E}$. Fourier transform of (2.5) could be obtained analytically, but keeping in mind a more general case we write it simply as

$$\vec{E}(\omega) = (\lambda\hat{i} + \mu\hat{j} + \nu\hat{k})g(\omega) \tag{2.6}$$

Total polarization is obtained from density and is time dependent:

$$\vec{P}^{tot}(t) = \int \vec{r}\delta\rho(\vec{r}, t)d^3r \tag{2.7}$$

An example of time dependent polarization for C_{60} fullerene is shown figure 2.1. It is

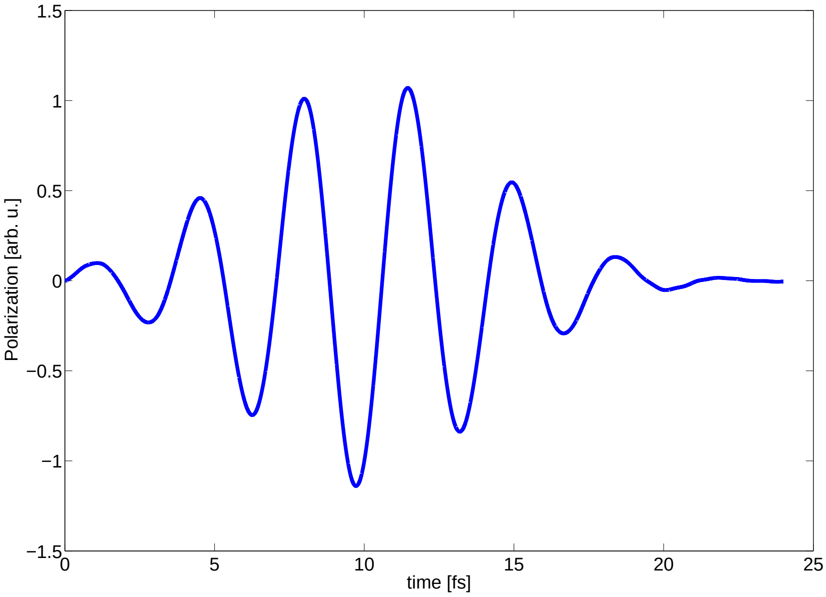

Figure 2.1: Time dependent polarization P^{tot}(t) of C_{60} fullerene propagated with PZ functional and external quasi-monochromatic field tuned to $\hbar\omega_0 = 1.17$ eV.

subsequently Fourier transformed:

$$\vec{P}^{tot}(\omega) = \int \vec{P}(t)e^{i\omega t}dt \tag{2.8}$$

Total polarization is a function of both frequency and strength of external electric field that is parametrized with (λ, μ, ν):

$$\vec{P}^{tot} = \vec{P}^{tot}(\omega, (\lambda, \mu, \nu)). \tag{2.9}$$

The quantities of interest are coefficients of Taylor expansion of $\vec{P}^{tot}(\omega, (\lambda, \mu, \nu))$ in respect to λ, μ, ν. The coefficients are found by converting several Taylor expansions of total polarization at different values of λ, μ, ν into a linear system.

2.1.2 Extraction in case of isotropic symmetry

As an illustration of the method consider a system with spherical (isotropic) symmetry, and a single frequency external wave. The second order processes will vanish, and in cases of linear and third order responses there will be only one independent component of susceptibility[3]. Suppose that we are interested in calculating $\chi^{(3)}_{xxxx}$. One would set μ, ν to zero, and propagate wavefunction three times, each with different value of $\lambda_1, \lambda_2, \lambda_3$. Next, one calculates three corresponding polarizations $\{P^{tot}_x(\lambda_i), i = 1, 2, 3\}$:

$$P^{tot}_x(\omega, \lambda) = \int\int x\delta\rho(\vec{r}, t)e^{i\omega t}d^3r dt, \tag{2.10}$$

and writes down three polynomial expansions:

$$P^{tot}_x(\omega, \lambda_i) = a(\omega)\lambda_i + b(\omega)\lambda_i^2 + c(\omega)\lambda_i^3. \tag{2.11}$$

By introducing a matrix of electric field strength $\hat{\Theta}$:

$$\hat{\Theta} = \begin{pmatrix} \lambda_1, \lambda_1^2, \lambda_1^3 \\ \lambda_2, \lambda_2^2, \lambda_2^3 \\ \lambda_3, \lambda_3^2, \lambda_3^3 \end{pmatrix}, \tag{2.12}$$

---

[3] In this case there exists the following relation between components of the third order susceptibility: xxxx = yyyy = zzzz = 3 xxyy = 3 xxyy = 3 yyxx = 3 zzyy = 3 zzxx

Table 2.3: Convolution integrals $\mathcal{G}$ for selected processes.

Process	$\mathcal{G}(\omega)$
SHG	$\int_0^\infty g(\omega')g(2\omega-\omega')d\omega'$
OR	$\int_0^\infty g(\omega')g^*(\omega')d\omega'$
THG	$\int_0^\infty \int_0^\infty g(\omega')g(\omega")g(3\omega-\omega'-\omega")d\omega' d\omega"$
IDRI/2-photon absorption	$\int_0^\infty \int_0^\infty g^*(\omega')g(\omega")g(\omega+\omega'-\omega")d\omega' d\omega"$

as well as vectors of polarizations $\vec{\mathcal{P}} = (P_x^{tot}(\omega,\lambda_1), P_x^{tot}(\omega,\lambda_2), P_x^{tot}(\omega,\lambda_3))$ and vector of coefficients $\vec{\mathcal{X}} = (a(\omega), b(\omega), c(\omega))$, a set of equations of type (2.11) is written as

$$\vec{\mathcal{P}} = \hat{\Theta}\vec{\mathcal{X}}. \tag{2.13}$$

After solving equation (2.13) for $\vec{\mathcal{X}}$, one gets $c(\omega)\,\lambda^3 = P^{(3)}_{xxxx}(\omega)$. Since $P^{(3)}_{xxxx}(\omega)$ is known, then $\chi^{(3)}_{xxxx}$ can be extracted from (2.2). $\chi^{(3)}$ appears in (2.2) in a non-local form. However, in case of quasi-monochromatic excitation the response is well localized in frequency domain, and $\chi^{(3)}$ could be pulled out of the integral[4] [43].

$$\mathcal{K}\int \chi^{(3)}_{xxxx}(-\omega;\,\omega",\omega',\omega-\omega"-\omega')\,\lambda^3\,g(\omega')\,g(\omega")\,g(\omega-\omega"-\omega')\,d\omega'\,d\omega" \sim$$
$$\sim \mathcal{K}\chi^{(3)}_{xxxx}(-\omega)\,\lambda^3\int g(\omega')\,g(\omega")\,g(\omega-\omega"-\omega')\,d\omega'\,d\omega" = \mathcal{K}\chi^{(3)}_{xxxx}(-\omega)\,\lambda^3\mathcal{G}(\omega). \tag{2.14}$$

The convolution $\mathcal{G}(\omega)$ depends on shape of external field and on the type of process, and is shown for four common processes in table (2.3). The second hyperpolarizability becomes:

$$\chi^{(3)}_{xxxx})(\omega) = \frac{c(\omega)}{\mathcal{K}\,\mathcal{G}(\omega)}. \tag{2.15}$$

Selecting appropriate $\mathcal{K}$ and $\mathcal{G}$ provides information about THG, IDRI and 2-photon absorption.

---

[4] The locality is further discussed in the next section.

2.1.3 Generalization

Off diagonal components of $\chi^{(n)}$ require more than one field. It depends on the symmetry of molecule (or crystal) which components are necessary to calculate. In case of molecules, hyperpolarizabilities are typically spatially averaged to account for the random orientation. This allows to compare the calculated and experimental results obtained from the gas phase. Tables (2.4) and (2.5) list components and selection of fields that are needed to obtain spatially averaged $\chi^{(2)}_{||}$ and $\chi^{(3)}_{||}$ in case when the molecular symmetry is neglected, or when molecule does not have any symmetry:

$$\chi^{(1)} = \frac{1}{3} \sum_{i=x,y,z} \chi^{(1)}_{ii} \tag{2.16}$$

$$\chi^{(2)} = \frac{1}{5} \sum_{i=x,y,z} \left(\chi^{(2)}_{zii} + \chi^{(2)}_{izi} + \chi^{(2)}_{iiz} \right) \tag{2.17}$$

$$\chi^{(3)} = \frac{1}{15} \sum_{i=x,y,z} \sum_{j=x,y,z} \left(\chi^{(3)}_{iijj} + \chi^{(3)}_{ijij} + \chi^{(3)}_{ijji} \right). \tag{2.18}$$

Generalization for off-diagonal components is simple. For compactness we re-label electric fields as

$$E_j(\omega) = \varepsilon_j \, g(\omega),$$

vector of coefficients as

$$\vec{\mathcal{X}} = (a^{(1)}_{11}, a^{(1)}_{12}, a^{(1)}_{13}, \ldots, a^{(2)}_{111}, a^{(2)}_{112}, a^{(2)}_{113}, \ldots, a^{(3)}_{1111}, a^{(3)}_{1112}, a^{(3)}_{1113}, \ldots), \tag{2.19}$$

vector of polarizations as

$$\vec{\mathcal{P}} = (P_1(\omega, \vec{E}(1)), P_2(\omega, \vec{E}(1)), P_3(\omega, \vec{E}(1)), \ldots, P_1(\omega, \vec{E}(\zeta)), P_2(\omega, \vec{E}(\zeta)), P_3(\omega, \vec{E}(\zeta))), \tag{2.20}$$

Table 2.4: Tensor components needed for evaluation of spatially averaged hyperpolarizabilities.

Degeneracy	Component	Field direction
1	zxx	x
1	zxx	y
1	zzz	z
2	xxz	x,z
2	yyz	y,z

and matrix of field strengths as

$$\hat{\Theta} = \begin{pmatrix} \varepsilon_1(1) & \varepsilon_2(1) & \varepsilon_3(1) & \dots & \varepsilon_1^2(1) & \varepsilon_1\varepsilon_2(1) & \varepsilon_1\varepsilon_3(1) & \dots & \varepsilon_1(1)^3 & \varepsilon_1(1)^2\varepsilon_2(1) & \dots \\ \dots & \dots & \dots & \dots & \dots & \dots & \dots & \dots & \dots & \dots & \dots \\ \varepsilon_1(\zeta) & \varepsilon_2(\zeta) & \varepsilon_3(\zeta) & \dots & \varepsilon_1^2(\zeta) & \varepsilon_1\varepsilon_2(\zeta) & \varepsilon_1\varepsilon_3(\zeta) & \dots & \varepsilon_1(\zeta)^3 & \varepsilon_1(\zeta)^2\varepsilon_2(\zeta) & \dots \end{pmatrix}, \tag{2.21}$$

where $k, l, m = 0, 1, 2, \dots$, $\eta = 1, 2, \dots, \zeta$ is a index labeling set of field amplitudes. In addition, $\hat{\Theta}$ is subject to

$$\det \left|\hat{\Theta}\right| \neq 0. \tag{2.22}$$

Then, similarly to (2.15), the response function $\hat{\chi}^{(n)}$ is:

$$\chi^{(n)}_{ik\dots m}(-\omega) = \frac{a^{(n)}_{ik\dots m}(\omega)}{\mathcal{K}\,\mathcal{G}(\omega)}. \tag{2.23}$$

Variants of the above method include "fitting" in either frequency or time domain. In these cases one sets up an overdetermined linear system, where $dim(\vec{\mathcal{P}}) > dim(\vec{\mathcal{X}})$, and formulate the problem as a linear least squares problem, where $\vec{\mathcal{X}}$ is sought as a minimum of

$$\|\hat{\Theta}\,\vec{\mathcal{X}} - \vec{\mathcal{P}}(\omega)\|_2. \tag{2.24}$$

However, the direct solution of (2.13) is preferable to "fitting", because it requires less data. Other approaches for extraction of $\chi^{(k)}$ exist, in particular numerical differentiation in frequency domain [43].

Table 2.5: Tensor components needed for evaluation of spatially averaged second hyperpolarizabilities.

Degeneracy	Component	Field direction
1	xxxx	x
1	yyyy	y
1	zzzz	z
3	xxyy	x,y
3	yyxx	x,y
3	yyzz	y,z
3	zzyy	y,z
3	xxzz	x,z
3	zzxx	x,z

2.2 Locality of nonlinear response under monochromatic excitation

The possibility of factoring $\chi^{(n)}$ out of integral (2.2) depends on how rapidly $\chi^{(n)}$ changes in a range of frequencies that makes contribution to the convolution integral $\mathcal{G}$ appearing in (2.14) [5]. We do not make any assumptions on how $\chi^{(n)}$ behaves, except that it is continuous in some frequency region $\Omega^{\chi}_{n-1} \in \mathbf{R}^{n-1}, \Omega^{\chi}_{n-1} = [\omega'_1, \omega_1] \otimes [\omega'_2, \omega_2"] \otimes \ldots$. However, we are free to define the shape of external electric fields. Setting fields to delta function would collapse the convolution integral entirely, which is equivalent of using purely monochromatic excitation. It is not practically possible to simulate a purely monochromatic pulse within RT-TDDFT. Instead one may use a Gaussian shaped field as a model of quasi monochromatic laser pulse.

For quasi monochromatic excitation with frequency ω_0 the absolute value of $|E(\omega)|$ asymptotically decreases outside of a small interval of frequencies centered at ω_0. If one sets a threshold $\varepsilon_M > 0$, then one may say that $E(\omega')$ is localized within interval Ω_1 if $\forall\ \omega' \in \Omega_1 \Rightarrow |E(\omega')| \leq \varepsilon_M$. For example, $E(\omega) = \lambda \int \sin(\omega_0 t) e^{-\frac{(t-t_0)^2}{4\sigma^2}} e^{i\omega t} dt$ is localized at $\Omega_1 = [\omega_0 - \Delta(\sigma, \varepsilon_M), \omega_0 + \Delta(\sigma, \varepsilon_M)]$, where

$$\Delta(\sigma, \varepsilon_M) = \frac{1}{|\sigma|} \sqrt{|\ln \frac{\varepsilon_M}{2\lambda\sigma\sqrt{\pi}}|}. \tag{2.25}$$

---

[5] See examples of $\mathcal{G}$ in table 2.3.

The products of electric fields $E(\omega')E(2\omega_o - \omega'$ and $E(\omega')E^*(\omega')$ have the same localization as $E(\omega)$, while $E(\omega')E(\omega")E(3\omega_o - \omega' - \omega")$ and $E(\omega')E^*(\omega")E(\omega_o - \omega' + \omega")$ have $\Omega_2 \approx \Omega_1 \otimes \Omega_1$. Moreover, for higher harmonic generation of n^{th} order $\Omega_{n-1} \approx \Omega_1 \otimes \Omega_1 \otimes \Omega_1 \ldots \approx [\Omega_1]^{n-1}$. The size of Ω_n is controlled by parameter σ, and could always be made smaller. Thus, as long as $\chi^{(n)}(\omega_1, \omega_2 \ldots, \omega_n)$ is continuous on Ω_{n-1}, one can adjust σ to make change in $\chi^{(n)}$ smaller then a threshold ε_χ:

$$|\chi^{(n)}(\omega_1, \omega_2 \ldots, \omega_n) - \chi^{(n)}(\omega_1', \omega_2' \ldots, \omega_n')| < \varepsilon_\chi \quad \forall \omega_i, \omega_i' \in \Omega_{n-1}. \tag{2.26}$$

Therefore, if $\chi^{(n)}$ is continuous on Ω_{n-1}, then it can be made local (factorable from the integral) on $\Omega_{n-1}^{\chi} \subset \Omega_{n-1}$. Presence of finite number of poles in Ω_{n-1} breaks Ω_{n-1} into regions Ω_{n-1}', where locality of $\chi^{(n)}$ can be re-established: $\Omega_{n-1}^{\chi'} \subset \Omega_{n-1}'$. For example, in case of second order process presence of a resonance ω_R on Ω_1 will break it into two frequency intervals. Calculations of $\chi^{(2)}$ then will proceed by approaching ω_R from left $\omega_R - \delta$ and right $\omega_R - \delta$ and progressively increasing σ.

Now, we turn to the analysis of polarization response in frequency domain under quasi-monochromatic excitation. We use Gaussian shaped external electric field pulse tuned to $\hbar\omega_0$ =1.79 eV to probe response of H_2O molecule[6]. At this frequency the optical interaction is lossless and dispersionless. The molecule was propagated and total polarization was calculated as described above. Total polarization was decomposed into the sum of first three orders using Method I (a.k.a. Linear Reduction method) described in the previous section. Figure 2.2 shows that linear polarizability and electric field have practically identical shapes. This is only possible if susceptibility is a real constant, since in frequency domain linear polarization is proportional to both electric field and generally frequency dependent susceptibility : $P(\omega) = \chi^{(1)}(\omega)E(\omega)$. Indeed this is the case in the small frequency interval near 1.79 eV, because interaction is lossless and dispersionless. Polarization vanishes outside of [1.1-2.44] eV range. This agrees with 0.1% localization range of ±0.95 eV. Now we turn to higher orders. Figure 2.3 shows second order polarization for H_2O

---

[6] Similar results are obtained for other small organic molecules such as carbon monoxide, hydrogen fluoride etc..

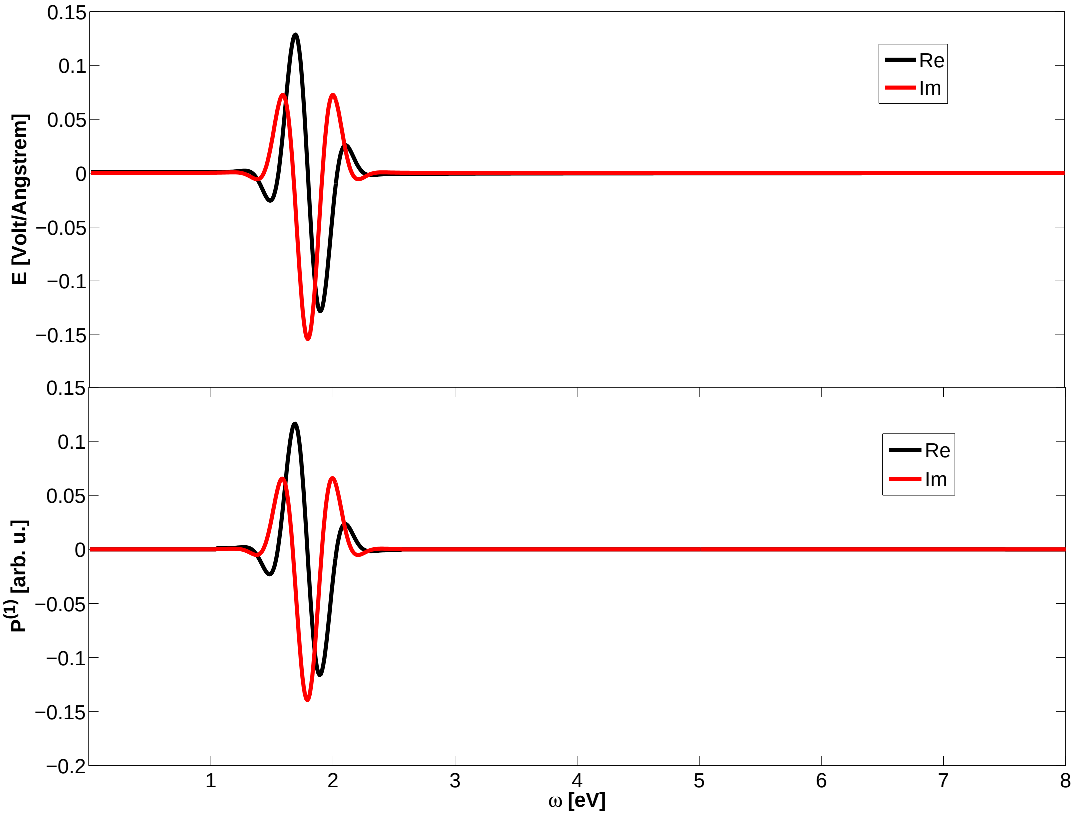

Figure 2.2: Linear polarization response to quasi monochromatic excitation at $\hbar\omega$=1.79 eV. On the top is electric field $E(\omega)$. At the bottom is second order nonlinear polarization $P^{(1)}(\omega)$. Real part is in black, imaginary part is red. Data is shown for H_2O molecule propagated using LB94 functional [8].

molecule. Shape of second order polarization is identical to square of applied electric field $E^2(\omega)$. This implies that not only $\chi^{(2)}$ is a real constant, but also that we have similar relation as in linear case: $P^{(2)}(\omega) = D^{(2)}\chi^{(2)}(\omega)E(\omega)E(\omega)$, where $D^{(2)}$ is degeneracy factor. Same argument holds for $\chi^{(3)}$. From Fig. 2.4 we deduce that $P^{(3)}(\omega) = D^{(3)}\chi^{(3)}(\omega)E(\omega)E(\omega)E(\omega)$. We see that generally non-local character of relationship between nonlinear polarization and corresponding susceptibility (2.2) is reducing to a simple product of nth power of electric field and nth order sussceptibility. This means that under sufficiently narrow quasimonochromatic excitation polarization response resembles response under mononochromaric excitation. Then in (2.2) we can make replacement $E(\omega_i) \rightarrow \delta(\omega_i - \omega_0)$ and reduce integral to a simple product of electric fields and corresponding sussceptibility. This is one of the two practically important features of quasimonochromatic probes. Another one may be easily inferred form Fig. 2.5. It is clear that second and third order responses are localized within *non-intersecting* frequency intervals. Therefore, under assumption that there is only second and third responses present, total polarization decomposes trivially into sum of second and third orders for SHG, THG and OR processes. This is the basis for Direct Evaluation Method for obtaining susceptibilities described below.

2.3 Method II: Direct Evaluation

Because under quasi-monochromatic excitation odd and even orders of nonlinear optical response are resolved, we may write:

$$P^{tot}(0) = P^{(2)}(0), \tag{2.27}$$

$$P^{tot}(2\omega) = P^{(2)}(2\omega), \tag{2.28}$$

$$P^{tot}(3\omega) = P^{(3)}(3\omega). \tag{2.29}$$

These relations are valid only if the higher order responses are negligible. This condition can be achieved in most of practical situations by selecting the appropriate amplitude of perturbing electric field. This means that, when for OR, SHG and THG

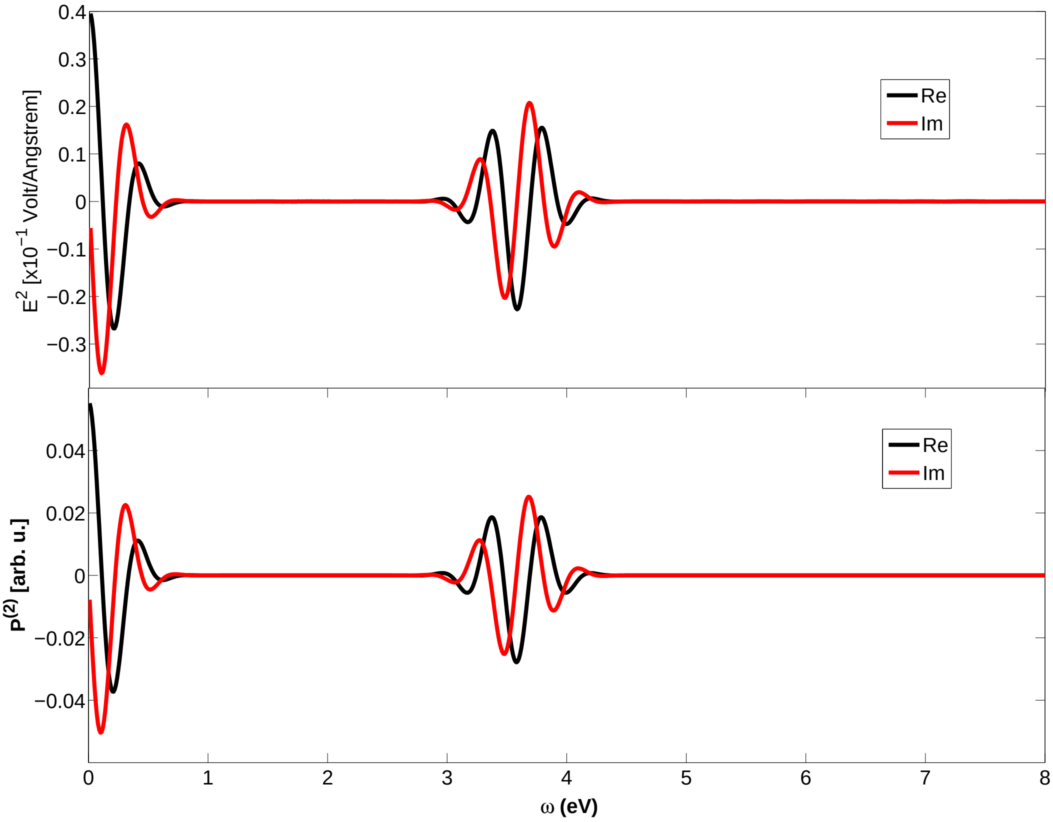

Figure 2.3: Second order polarization response to quasi-monochromatic excitation at $\hbar\omega$ =1.79 eV. On the top is square of electric field $E^2(\omega)$. At the bottom is second order nonlinear polarization $P^{(2)}(\omega)$. Real part is in black, imaginary part is red. Data is shown for H_2O molecule propagated using LB94 functional [8].

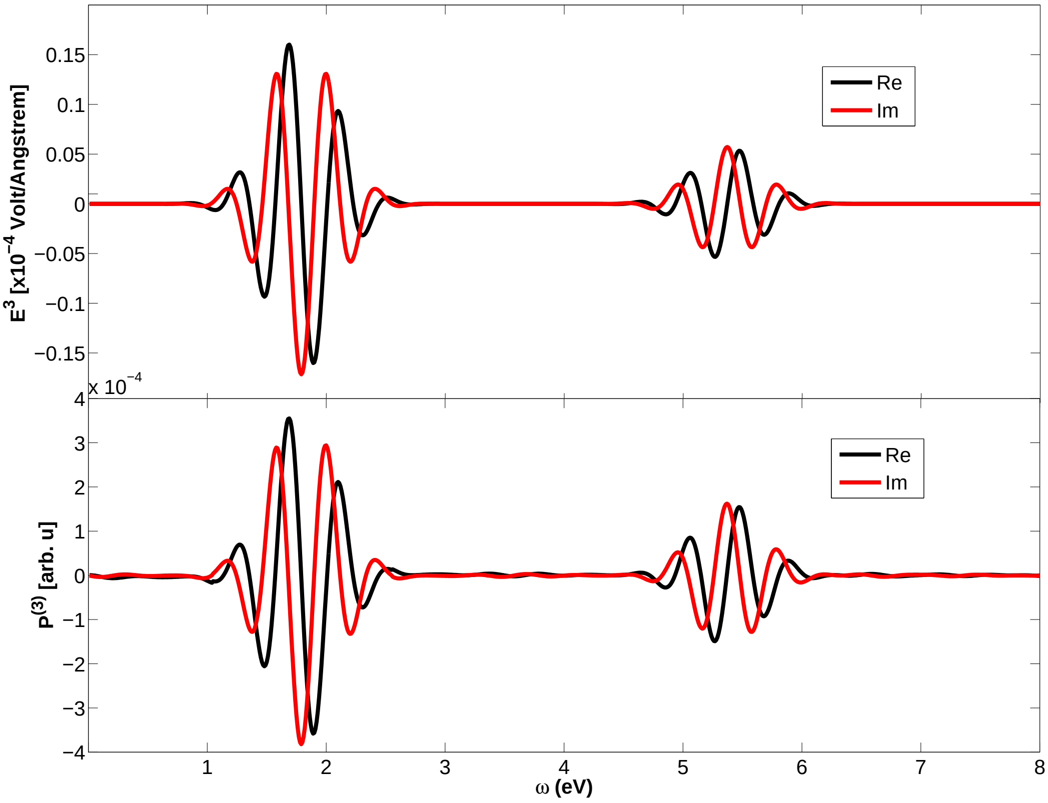

Figure 2.4: Third order polarization response to quasi-monochromatic excitation at $\hbar\omega$ =1.79 eV. On the top is cube of electric field $E^3(\omega)$. At the bottom is third order nonlinear polarization $P^{(3)}(\omega)$. Real part is in black, imaginary part is red. Data is shown for xxzz component of H_2O molecule propagated using LB94 functional.

decomposition $P^{tot} = \sum P^{(n)}$ happens automatically in frequency domain, then, we can extract diagonal elements of $\chi^{(2)}$ and $\chi^{(3)}$ for these processes from a single propagation. If field has one component $\vec{E} = (E_x, 0, 0)$, then:

$$P_i^{tot} = \sum_{jk} D\chi_{ijk}^{(2)} E_j E_k = D\chi_{ixx}^{(2)} E_x^2 \tag{2.30}$$

Diagonal components are found from:

$$\chi_{ixx}^{(2)}(\omega) = \frac{P_i^{tot}(\omega)}{DE_x^2(\omega)} \tag{2.31}$$

After diagonal components are found, one sets the electric fields to $\vec{E}(\omega) = (E_x(\omega), E_y(\omega), 0)$:

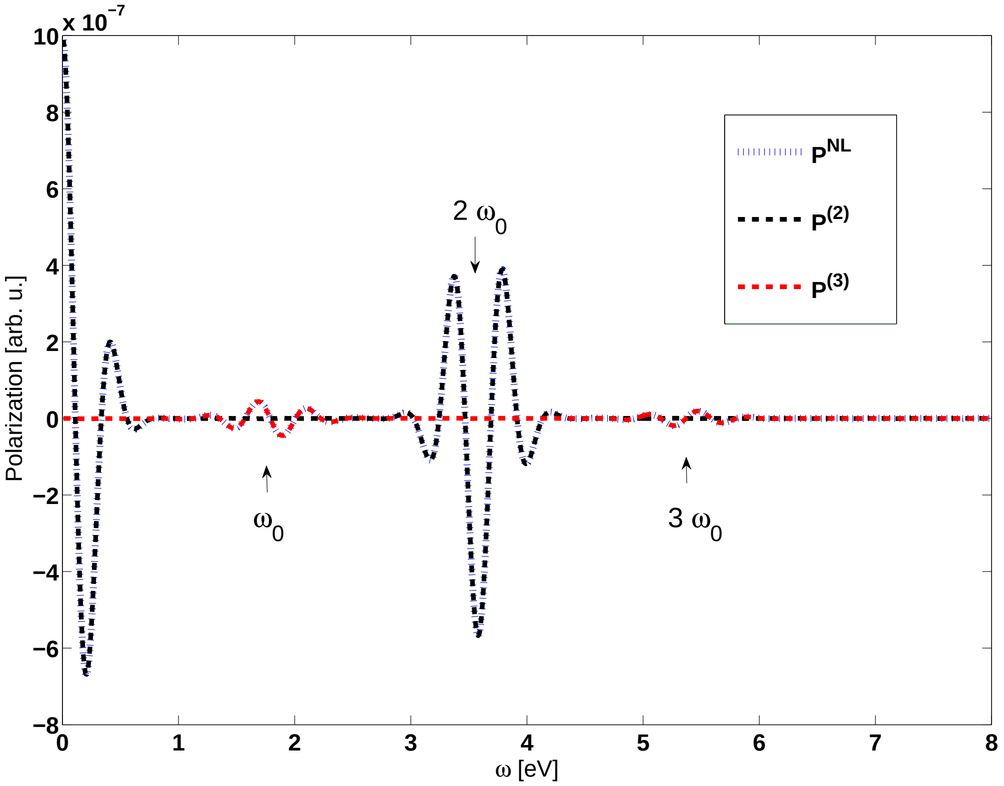

Figure 2.5: Decomposition of real part of nonlinear polarization $P^{NL} = P^{tot} - P^{(1)}$ into second $(P^{(2)}(\omega))$ and third order $(P^{(3)}(\omega))$ polarizations in frequency space. The different orders of polarization are resolved in the frequency domain. Data is shown for xxz component of H_2O molecule propagated using LB94 functional [8].

$$P_i^{tot} = \sum_{jk} D\chi^{(2)}_{ijk} E_j E_k = \mathcal{K}\chi^{(2)}_{ixx} E_x^2 + D\chi^{(2)}_{ixx} E_y^2 + 2D\chi^{(2)}_{ixy} E_x E_y \tag{2.32}$$

Setting $E_x(\omega) = E_y(\omega) = E(\omega)$ and calculating $\chi^{(2)}_{ixx}$ and $\chi^{(2)}_{iyy}$ independently one gets for $\chi^{(2)}_{ixy}$:

$$\chi^{(2)}_{ixy}(\omega) = \frac{1}{2}\left(\frac{P_i^{tot}(\omega)}{DE^2(\omega)} - \chi^{(2)}_{ixx}(\omega) - \chi^{(2)}_{iyy}(\omega)\right). \tag{2.33}$$

Thus, from five propagations one obtains five components necessary for averaging (2.17). Equation (2.33) is valid for SHG and OR processes.

Similarly for THG:

$$P_i^{tot}(3\omega) = \sum_{jkl} D\chi^{(3)}_{ijkl} E_j E_k E_l = D\chi^{(3)}_{ixxx} E_x^3(3\omega). \tag{2.34}$$

Diagonal components are

$$\chi^{(3)}_{ixxx}(3\omega) = \frac{P_i^{tot}(3\omega)}{DE_x^3(3\omega)}, \tag{2.35}$$

and off diagonals are:

$$\chi^{(3)}_{iyxx}(3\omega) = \frac{1}{6}\left(\frac{P_i^{tot}(3\omega)}{DE^3(3\omega)} - \chi^{(3)}_{ixxx}(3\omega) - \chi^{(3)}_{iyyy}(3\omega)\right). \tag{2.36}$$

Because linear and third order responses overlay at fundamental frequency ω_0, IDRI/TPA requires more then one propagation. For diagonal components we have:

$$\begin{cases} P^{tot}(\omega) = D\chi^{(3)}(\omega)E^2(\omega)E^*(\omega) + \chi^{(1)}(\omega)E(\omega) \\ P^{tot'}(\omega) = D\chi^{(3)}(\omega)E^{2'}(\omega)E^{*'}(\omega) + \chi^{(1)}(\omega)E'(\omega) \end{cases}. \tag{2.37}$$

P^{tot} is obtained from propagation under field $E(\omega)$, and $P^{tot'}$ is obtained from propagation under field $E'(\omega)$. Diagonal components are obtained from

$$\chi^{(3)}_{ixxx}(\omega) = \frac{P_i^{tot}(\omega)E'(\omega) - P_i^{tot'}(\omega)E(\omega)}{D(E^3(\omega)E'(\omega) - E^{3'}(\omega)E(\omega))}. \tag{2.38}$$

Similar considerations apply to off-diagonal components.

The Direct method is significantly more efficient than any other real-time method.

In case of diagonal components only three propagations are needed, while the Linear Reduction method requires nine. Spatially averaged $\beta_{||}$ requires five propagations in case of Direct method *vs.* twenty five in case of Linear Reduction, making approximately fivefold reduction of total calculation time.

2.4 The role of the convolution integral $\mathcal{G}(\omega)$ in calculations of response functions

One may not fail to notice that convolution integral $\mathcal{G}(\omega)$ disappears from expression for nonlinear susceptibility equations (2.33,2.36,2.38). This is only possible if $\mathcal{G}(\omega)$, is either real or imaginary constant. This is precisely the case for a Gaussian pulse. $\mathcal{G}(\omega)$ for SHG process is shown in Fig. 2.6. It is a real constant within a range of frequencies relevant for calculation of SHG response. The role of $\mathcal{G}(\omega)$ is to account for the finite width of quasi-monochromatic excitation. Therefore it can depend on the width of the pulse but not on the frequency of excitation. In case of THG $\mathcal{G}(\omega)$

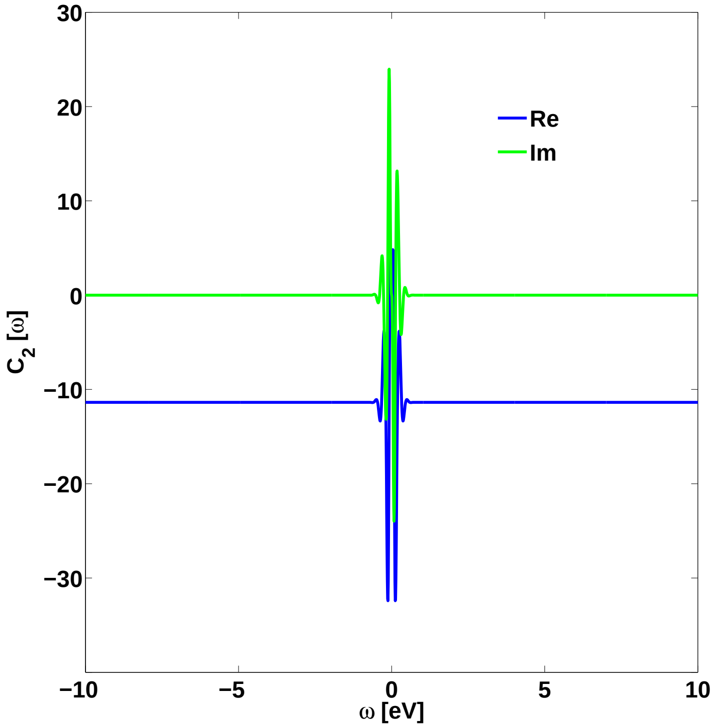

Figure 2.6: The convolution integral $\mathcal{G}(\omega)$ in case of SHG process. It is a constant everywhere except in a small interval near zero, where integration breaks down.

is purely imaginary.

2.5 Method III: Differentiation in Frequency Domain

The fact that under quasi-monochromatic excitation polarization response is local in frequency domain, allows one to calculate Taylor expansion for total polarization by direct differentiation. In this case, the partial derivatives are calculated by using finite differences. The following simple argument shows equivalence between linear decomposition and numerical differentiation in frequency domain. If we know polarization at specific frequency $p_i(\omega)$, we can write it in the following form:

$$p_i(\omega) = p_i^{(1)}(\omega) + p_{ijk}^{(2)}(\omega)\,\hat{e}^j\,\hat{e}^k + p_{ijkl}^{(3)}(\omega)\,\hat{e}^j\,\hat{e}^k\,\hat{e}^l + \ldots, \tag{2.39}$$

where $\hat{e}^j$ - Cartesian orthogonal unit vectors. We can also write it as a formal Taylor expansion:

$$p_i(\omega) = \frac{\partial p_i(\omega)}{\partial E^j}\,\delta E_j + \frac{1}{2!}\frac{\partial^2 P_i(\omega)}{\partial E^j \partial E^k}\,\delta E_j\,\delta E_k + \frac{1}{3!}\frac{\partial^3 P_i(\omega)}{\partial E^j \partial E^k \partial E^l}\,\delta E_j\,\delta E_k\,\delta E_l + \ldots. \tag{2.40}$$

Or we can write it as a polynomial in δE_k where coefficients $a_{ijk\ldots}^{(n)}$ are obtained by fitting a set of $\{p_i(\omega)\}$ computed at different fields:

$$p_i(\omega) = a_{ij}^{(1)}\,\delta E_j + a_{ijk}^{(2)}\,\delta E_j\,\delta E_k + a_{ijkl}^{(3)}\,\delta E_j\,\delta E_k\,\delta E_l + \ldots. \tag{2.41}$$

Above we had used Einstein summation notation, and no summation will be applied below. Now, suppose we are interested in a specific component of the second order susceptibility $\chi_{ijk}^{(2)}$. By comparing second order terms in equations (2.40), (2.41), and (2.39) we get:

$$\frac{1}{2\pi}\int \chi_{ijk}^{(2)}(-\omega;\omega',\omega-\omega')E_j(\omega')E_k(\omega-\omega')d\omega' = \frac{(2-\delta_{jk})}{2}\frac{\partial^2 p_i(\omega)}{\partial E^j \partial E^k}\,\delta E_j\,\delta E_k = a_{ijk}^{(2)}\,\delta E_j\,\delta E_k = p_{ijk}^{(2)}(\omega). \tag{2.42}$$

Table 2.6: Comparison between methods for HF. For individual components, the numerical discrepancy occurs at 10^{-6} a.u. level. This agreement is typical and had served as an additional quality check for the data presented in this work.

Method	$\chi^{(2)}_{zxx}$	$\chi^{(2)}_{zzz}$	$\chi^{(2)}_{\|\|}$
Frequency Domain	-2.89253973358058	-11.6003281577394	-10.4312445749404
Time Domain	-2.89253973358058	-11.6003281577394	-10.4312445749404
Finite Difference	-2.89253980559773	-11.6003278763701	-10.4312444925393

Next, we factor out the amplitude of the electric field and write it as a product with unity normalized function $f(\omega)$ that contains frequency dependence:

$$E_j(\omega') = \delta E_j\, f(\omega').$$

In general case one has to solve an integral equation similar to (2.2), but here, for quasi-monochromatic fields we impose locality on $\chi^{(2)}_{ijk}$ and write:

$$2\,\pi\, p^{(2)}_{ijk}(\omega) = \chi^{(2)}_{ijk}(-\omega)\, \delta E_j\, \delta E_k \int f(\omega') f(\omega-\omega')\, d\omega'. \tag{2.43}$$

Finally, we get the representations of $\chi^{(2)}_{ijk}$ as a fitting coefficient (middle), or a partial derivative (right):

$$\chi^{(2)}_{ijk}(-\omega) \;=\; \frac{2\,\pi\, a^{(2)}_{ijk}}{\int f(\omega') f(\omega-\omega')\, d\omega'} = \frac{(2-\delta_{jk})\,\pi}{\int f(\omega') f(\omega-\omega')\, d\omega'} \frac{\partial^2 p_i(\omega)}{\partial E^j \partial E^k}. \tag{2.44}$$

Thus, when the non-locality of $\chi^{(n)}$ in (2.2) could be neglected, the finite-difference method could be used directly in the frequency space. Practical calculations show good agreement between the methods. Comparison between these methods can be found in table (2.6).

2.6 Conclusion

The three methods described in this chapter have different accuracy, reliability and computational cost. The computational cost is dominated by the propagation of the wavefunction, and the number of propagations used by the method is a measure of its cost. Direct Evaluation is particularly suitable for large systems, because it needs as little as one propagation of wavefunction. It is also the least accurate as it may not distinguish between different orders of response, because of the limited number of propagations. The Linear Reduction method is optimal in terms of quality and computational cost. Each propagation corresponds to a term in the polynomial expansion of the total polarization (2.41). The accuracy is increased by increasing the number of propagations. The limitation of the method is its computational cost, which becomes important in case of large systems. The "fitting" methods previously used [31] are inherently less efficient than the Linear Reduction, because there are always more propagations than terms in the polynomial expansion. In other words, some propagations are "wasted", because they do not contribute to the increase in accuracy.

All described methods depend on locality of the polarization response in frequency space. In the second section of this chapter we had shown that by using quasi monochromatic excitation the optical response could be localized in practice. We had also demonstrated that for at least some small organic molecules under non-resonance conditions the quasi monochromatic response is indistinguishable from monochromatic. In this case the response becomes fully local, and the integral relation that generally exists between higher order polarization and corresponding hyperpolarizability (2.2) reduces to a simple product of electric fields and a complex constant.It also means that nonlinear polarization decomposes into a finite polynomial of order N_{max}:

$$P^{NL}(\omega) = \sum_{k=2}^{N_{max}} \chi^{(k)}(\omega) E^k(\omega). \tag{2.45}$$

This condition is not expected to hold for all systems and excitation regimes, yet it represents an important case, because it shows that the nonlinear response could be formally very similar to the linear response. The condition could be used as the basis for classification of nonlinear response. One may say that when (2.45) holds, we have a case of Regular nonlinear response.

Chapter 3

NONLINEAR RESPONSE IN ATOMS AND MOLECULES

3.1 Real-Space Implementation

In this section we give details on numerical implementation of the real-time TDDFT in real-space. In real-space calculations [44], functions and operators that depend on spatial coordinates are represented on a three dimensional lattice. Differential operators that act on spatial variables become finite-difference operators. Action of the Hamiltonian on an orbital ϕ_q is represented by:

$$\begin{aligned}\hat{H}\phi_q(x_i, y_i, z_i) = -\frac{\hbar^2}{2m}[\sum_{n_1=-M}^{M} C_{n_1}\phi_q(x_i + n_1 h, y_i, z_i) + \sum_{n_2=-M}^{M} C_{n_2}\phi_q(x_i, y_i + n_2 h, z_i) + \\ + \sum_{n_3=-M}^{M} C_{n_3}\phi_q(x_i, y_i, z_i + n_3 h)] + [V_{ion}(x_i, y_i, z_i) + V_H(x_i, y_i, z_i) + \\ + V_{xc}(x_i, y_i, z_i)]\phi_q(x_i, y_i, z_i),\end{aligned} \tag{3.1}$$

where $2M$ is order of finite difference, h is a lattice step, (x_i, y_i, z_i) is a point in discretized space. Coefficients C_{n_k} for a different orders of approximation are given in Table 3.1.

External potential also includes ionic potential V_{ion} that represents combined pseudopotential of nuclei and core electrons. Use of pseudopotentials dramatically increases efficiency of calculations. While local versions of pseudopotentials exists, the most efficient are fully separable pseudopotentials that have local and angular momentum dependent non-local parts [45]:

$$V_{ion} = \sum_{a=1}^{N_{nuc}} V_{loc,a} + \sum_{a=1}^{N_{nuc}} \sum_{l=1}^{l_{max}} \sum_{m=-l}^{l} c_{a,l,m} \mathcal{U}_{a,l,m} \mathcal{U}_{a,l,m}^T \tag{3.2}$$

Table 3.1: Coefficients for uniform grid representation of Laplacian operator. N_{FD} is order of Finite Difference.

N_{FD}									
2				1	-2	1			
4			$-\frac{1}{12}$	$\frac{4}{3}$	$-\frac{5}{2}$	$\frac{4}{3}$	$-\frac{1}{12}$		
6		$\frac{1}{90}$	-$\frac{3}{20}$	$\frac{3}{2}$	$-\frac{48}{18}$	$\frac{3}{2}$	$-\frac{3}{20}$	$\frac{1}{90}$	
8	$-\frac{1}{560}$	$\frac{8}{315}$	$-\frac{1}{5}$	$\frac{8}{5}$	$-\frac{205}{72}$	$\frac{8}{5}$	$-\frac{1}{5}$	$\frac{8}{315}$	$-\frac{1}{560}$

Non-local vectors $\mathcal{U}_{a,l,m}$ are sparse and vanish outside of spherical regions surrounding atoms. The radii of these regions are atom dependent. $c_{a,l,m}$ are normalization constants.

3.2 Numerical Considerations

There are two groups of factors that determine quality of real time real space TDDFT simulations. The first group includes the size of simulation cell, grid step, exchange-correlation functional, and convergence of forces and energy in ground state. The size of cell has to be large enough that at any step of calculations density at the periphery of the cell be close to zero. When this condition is met, size of the box does not affect calculated values of susceptibilities. Since total number of operations depends cubically on the size, it is important to choose the optimal size. Table 3.3 shows data for HF molecule. Supercell is a cube with side L. The susceptibilities show little dependence on L, because L = 10 Å is sufficient for this small molecule. For the calculations presented in this chapter 14-20 Å cell was used. The second parameter is grid step. In table 3.2 we hold L = 14 Å and vary the grid step. $\Delta x =$ 0.25 Å is an acceptable choice for a grid step for a variety of molecules and atoms [1]. The LDA functionals PZ and VWN [39, 40] are a good first choice, although as practice shows they frequently give overestimated hyperpolarizabilities [2]. Among GGA functionals, LB94 [8] frequently gives better agreement with experiment then LDA. However, it may not conserve energy, tends to yield wrong HOMO-LUMO gap,

---

[1] It depends on implementation of the pseudopotentials. But once convergence criteria in respect to grid step is established for a particulate set of pseudopotentials, grid step doesn't have to be frequently adjusted.

and may affect stability of calculations [2]. Poorly converged ground state results in unphysical oscillations of polarizability. Better then 0.01 eV convergence in single particle energies is expected.

Table 3.2: Dependence of $\chi^{(2)}$ on grid spacing for HF. Size of simulation cell was kept at 14 Å.

Δx (Å)	$\chi^{(2)}_{zxx}$	$\chi^{(2)}_{zzz}$	$\chi^{(2)}_{\|\|}$
0.225	-2.84	-12.77	-11.07
0.250	-2.97	-11.86	-10.68
0.275	-4.98	-8.85	-11.29
0.300	-27.95	-17.03	-43.76

Table 3.3: Dependence of $\chi^{(2)}$ on the size of simulation cell for HF. The grid step was kept at 0.25 Å.

L (Å)	$\chi^{(2)}_{zxx}$	$\chi^{(2)}_{zzz}$	$\chi^{(2)}_{\|\|}$
10	-2.90	-11.62	-10.45
12	-2.90	-11.62	-10.45
14	-2.89	-11.60	-10.43
16	-2.89	-11.60	-10.43

The second group defines the stability and fidelity of Real Time Evolution. Among this group are size of time step Δt, total simulation time and maximum strength of applied electric field. The stability of the propagation is critically dependent on the size of time step Δt. It is bounded by the following expression [32]

$$0 < \Delta t < \sqrt{\frac{2}{9}} m (\Delta x)^2, \tag{3.3}$$

where m is electron's mass. The error in wavefunction at each step is $\sim \mathcal{O}((\frac{\Delta t |E(t)|}{\hbar})^5)$, and in principle could be matched to machine precision by choice of Δt and the amplitude of external field E_{max}. Choosing $\Delta t \sim 10^{-3}$ fs ensures stable propagation for about 10^5 steps for majority of systems. When a small enough step is chosen to provide the computational stability through entire simulation, then the results do not appear to vary with the size of the time step (see table 3.4).

---

[2] LB94 is susceptible to numerical instabilities because it calculates asymptotic Coulomb tail from density gradient in the regions of near zero density.

Table 3.4: Dependence of $\chi^{(2)}$ on the size of time step dt for HF. N_t - is the total number of steps. The total simulation time was kept at 26.21 $\hbar$/eV.

dt ($\hbar$/eV)	N_t	$\chi^{(2)}_{zxx}$	$\chi^{(2)}_{zzz}$	$\chi^{(2)}_{\|\|}$
10^{-3}	26214	-2.89	-11.60	-10.43
1.6×10^{-3}	16384	-2.89	-11.60	-10.43
2.0×10^{-3}	13108	-2.89	-11.60	-10.43
2.62×10^{-3}	10000	N/D	N/D	N/D

The choice of the strength of electric field is also important. On one hand the field has to be strong enough to elicit a robust nonlinear response of desirable order. On another, it should not be strong enough to excite higher order responses. If one wants to use direct evaluation method, then the highest response should be not higher then third. This makes the choice of field strength molecule dependent. We had used $E \sim 0.013$ (V/Å) as a starting point, and then repeated calculations with increased field, occasionally as high as 1.0 (V/Å) (where most of the molecules undergo Coulomb explosion). Then we choose the region of the field where the response functions show least field dependence. The field range $E \sim 0.013 - 0.053$ (V/Å) is satisfactory for all cases we have tested so far.

Table 3.5: Second order susceptibilities $\chi^{(2)}_{||}(-2\omega;\omega,\omega)$. The energy, $\hbar\omega$, is in eV; the calculated permanent dipole moment, $|\vec{\mu}|$, is in (Debye); and $\chi^{(2)}$ is in atomic units. The experimental data is taken from [1]. GF ($\chi^{(2)}_{||}$) stands for the results obtained using method of Iwata and Yabana [2], [5Z4P] is from [3] and is calculated by using 5Z4P basis. The asterisk denotes data from [4].

molecule	$\|\vec{\mu}\|$	$\hbar\omega$	$\chi^{(2)}_{\|\|}$	Exp.	GF	[5Z4P]
CO	0.116	1.79	35.49	30.2±3.2	35.48	33.24
		1.96	37.07		36.89	34.70
H_2O	1.953	1.79	-35.45	-22.2 ± 0.9	-35.36	-28.90
		1.96	-38.13		-37.83	-30.9
HF	1.908	1.79	-10.39	-11.0±1.0	-11.06	-10.58 *
		1.96	-10.65		-11.42	-10.93 *
H_2S	1.075	1.79	-32.39	-10.1±2.1	-32.48	N/A
NH_3	1.585	1.79	-120.58	-48.9±1.2	-119.9	N/A
pNA	8.48	1.17	1080	1072±44	N/A	1083

Table 3.6 shows the dependence of the first hyperpolarizability on the strength

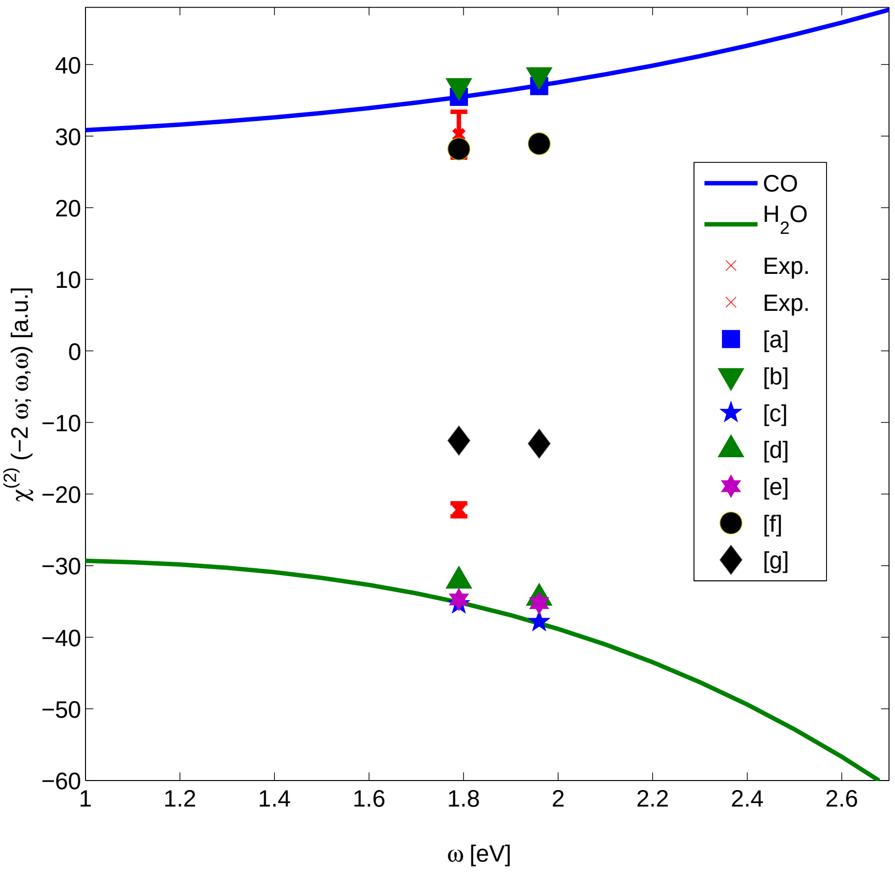

Figure 3.1: Dispersion curves for the second order nonlinear susceptibility $\chi^{(2)}(-2\omega;\omega,\omega)$ of CO (top), and H_2O (bottom) molecules. The experimental data is from [1]; [a,c] denotes results obtained by using the method of Iwata and Yabana [2]; [b,d] shows the results of Ref. [4], [e] denotes the results from [9], and [f,g] are Hartree-Fock calculations from [4].

of the electric field for the CO molecule. An eightfold increase in the electric field results in less then 1% change in $\chi^{(2)}$, indicating the stability of the calculated results with respect to the choice of field strength. Similarly, Table 3.7 shows that the second hyperpolarizability is also stable in a fourfold range of electric field. The eight-fold increase in electric field pushes the molecule out of the region of stability but only by 17 %.

Table 3.6: Dependence of $\chi^{(2)}$ on ΔE for CO. The field strength is given in (V/ Å). Eight-fold increase in the field strength results in a $\sim$ 0.31% decrease in the first hyper-polarizability.

$\lvert\Delta E_\alpha\rvert$	$\chi^{(2)}_{zxx}$	$\chi^{(2)}_{zzz}$	$\chi^{(2)}_{\parallel}$
0.013	10.74	38.46	35.97
0.026	10.72	38.43	35.92
0.053	10.71	38.43	35.90
0.106	10.69	38.38	35.86

Table 3.7: Dependence of $\chi^{(3)}$ on ΔE for N_2. The field strength is given in (V/Å). Eight-fold increase in the field strength results in a $\sim$ 17% increase in the second hyper-polarizability.

$\lvert\Delta E_\alpha\rvert$	$\chi^{(3)}_{xxxx}$	$\chi^{(3)}_{zzzz}$	$\chi^{(3)}_{xxzz}$	$\chi^{(3)}_{\parallel}$
0.013	1269	1655	380	1312
0.026	1220	1788	373	1307
0.053	1263	1680	386	1318
0.106	1397	2085	470	1539

Table 3.8: Third order susceptibilities. The energy, $\hbar\omega$, is in eV, and $\chi^{(3)}_{\parallel}(-3\omega;\omega,\omega)$ is in atomic units. The column GF shows the results obtained by the method of Iwata and Yabana [2] using the same ground state orbitals as in our calculations, and c) denotes the result of Ref. [2].

molecule	$\hbar\omega$	$\chi^{(3)}_{\parallel}$	Experiment	GF
Ar	1.175	2354	1000±100	2283
Kr	1.175	5312	2790± 270	5064
Ne	1.175	191	79± 8	189
N_2	1.790	1440	1295± 206	1663
C_6H_6	1.790	59141	23810± 460	58500

3.3 Atoms and Molecules

In Tables 3.5 and 3.8 our results are compared with experiments and other calculations. The calculated results are close to the results obtained by using the method of [2], and the results of Salek et al. [4] and Andrande et al. [9]. On the experimental side, the second order susceptibilities of the CO, H_2O and HF molecules show a rather good agreement with the measurement. On the other hand, the second order susceptibilities for H_2S, NH_3, and majority of third order susceptibilities overestimate the experimental data by the factor of three. We expect that more sophisticated exchange-correlation functionals, such as B3LYP and LB94 will improve agreement with experiment. The discrepancy between the theory and experiment is due to several factors. The most important ones are a) absence of nuclear motion, b) condensed phase effects and c) traditional shortcomings of the LDA functionals. For the CO and H_2O molecules we calculated the dispersion curves that demonstrate the correct qualitative behavior in a non-resonant spectral sectors (see Fig. 3.1). On the figure are results of calculations done by others [4, 9] as well as experimental results [1] and the results obtained using method of Iwata and Yabana [2]. While none of the theoretical results matches experimental data for H_2O molecule, all calculations for CO molecule show better agreement. The discrepancy with experiment strongly depends on the level of theory and less on the method of calculations. Hatree-Fock underestimates CO experimental data and overestimates H_2O data. In contrast, TDDFT and DFPT calculations overestimate CO data and underestimate H_2O data. When the same ground state is used, difference between real-time TDDFT calculations and DFPT calculations using Iwata and Yabana algorithm are close to each other then calculations within the DFPT by others [4]. At the same time calculations within modified Sternheimer approach of Andrade et al [9] for H_2O molecule are close to ours. One may conclude that:

- Level of the theory plays decisive role in determining realism of calculations.
- ALDA fares better then Hartree-Fock, but the differences depend on specifics of molecular structure.

- ALDA functional is the key source of discrepancy between our calculations and experiment.

One should keep in mind that the above observations are drawn from data for small and medium organic molecules calculated under Kleinman symmetry conditions [3] and may have limited generality.

3.4 Summary

In summary, we have explored the applicability and reliability of real-time real-space TDDFT method for calculations of molecular hyperpolarizabilities. The calculations are stable with respect to the variation of field strength, and there is no convergence problem associated with the basis functions. The calculations are in line with the results obtained by other methods using LDA functional and represent accurate estimates of nonlinear optical properties at the level of TDDFT.

The real-time TDDFT (RT-TDDFT) method to calculate response functions is fundamentally different from other perturbation theory based methods (such as the modified Sternheimer approach [2, 9]). The density and all observables that are derived from it are obtained from the single particle states that are explicitly time dependent and non-perturbative. The inclusion of nuclear motion is made simple in this case (for example by using Ehrenfest-type nuclear dynamics [46]) and does not require any changes in extraction algorithms. There are also critical computational differences between real-time and the perturbative methods based on the Sternheimer approach. The modified Sternheimer method relies on linear solvers and their performance determines the quality of the derived response functions. For large, complex molecules the convergence of these algorithms becomes problematic even at off-resonant frequencies. And near resonance they stop working even for the small molecules. The real-time propagation is stable near the resonance, and produces the data with the same efficiency. The real-time methods are computationally demanding, but these demands are predictable and propagation routines are easily scalable.

---

[3] See appendix B for definition

On another hand it is not possible to say how many iterations will take to achieve convergence for a linear solver.

Chapter 4

SILVER CLUSTERS

In this chapter we study the optical response of silver clusters spanning in size from 2.6 Å to 1 nm size: Ag_2, Ag_4, Ag_8, Ag_{16}, Ag_{32}. The structures of the clusters presented on Figure 4.1, and characteristic geometric parameters in Table 4.1.

Table 4.1: Geometric parameters and dipole moments of silver clusters.$|\vec{\mu}|$ is static dipole moment in Debye units. R_{eff} is characteristic size of density distribution in Å. R_{max} is maximum stretch of density distribution in Å.

Cluster	Symmetry	$\lvert\vec{\mu}\rvert$	R_{eff}	R_{max}
Ag_2	$D_{2\infty}$	0.01	2.6	5.7
Ag_4	D_{2h}	0.01	5.8	7.95
Ag_8	D_{4d}	0.03	5.2	7.3
Ag_{16}	C_1	1.12	7.63	9.74
Ag_{32}	C_1	0.61	9.11	12.74

The linear optical response of small and medium [1] silver clusters has been intensively studied from early nineties to the present day [47, 48, 49, 50, 51]. The reason for continuing attention is the non-trivial electronic structure of clusters. The 1B group of elements, of which Ag is a representative, has 1*s* valence electron next to a filled *d*-subshell and filled inner shells. In a small silver cluster, *d*-electrons have propensity to strongly influence the density distribution of the valence electrons leading to among other effects to a shift of surface plasmon frequency. The character of *d*-subshell and *s*-electron interaction is size, geometry and charge state dependent. Although the plasmon frequency is generally reduced from silver bulk value of ω_{bp}= 5.2 eV to experimentally observed in small neutral clusters of ω_{cp} ≈3.8 eV [48, 52, 47], there is also a "blue shift" phenomena, which mostly shows in negatively charged clusters. The effect is partly attributed to increased plasmon frequency for the clusters with

---

[1] Ranging from 2 to 20 atoms.

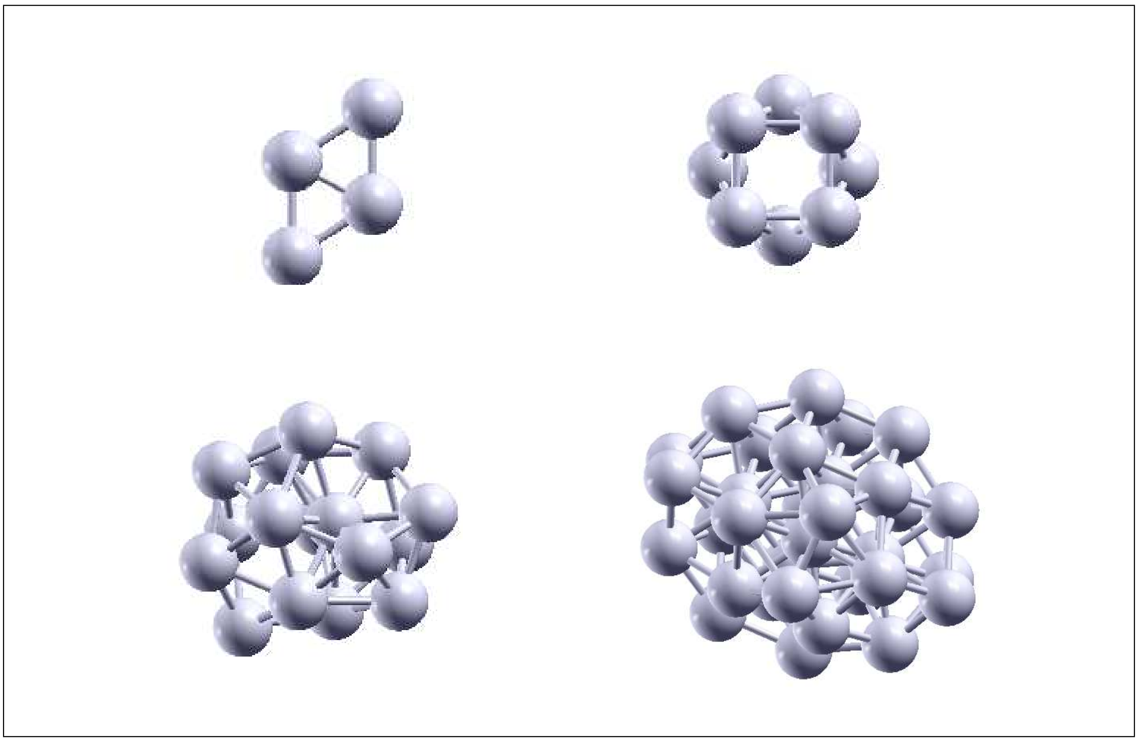

Figure 4.1: Structure of silver clusters: Ag_4 [10], Ag_8 [10], Ag_{16} [11], Ag_{32} [11].

smaller size [48].

4.1 Metallic features in absorption of large clusters

Before turning to the calculation of the nonlinear response, we briefly look at the absorption spectra. There are two reasons for that. One is that we can check quality of our simulation against known results. Another is that we find interesting an aspect that has not been thoroughly examined yet, and to which we want to bring attention: transition to metallic state that has to occur at some, perhaps very large, number of atoms in a cluster. It is interesting to find out what this number may be. It is also interesting to find out whether the method developed for finite systems would fail well before reaching the metallic state or not.

We proceed by calculating and examining features in absorption spectra that positively correlate with the number of atoms in a cluster. For calculating the absorption spectra we follow nearly the same procedure as we use for calculation of nonlinear

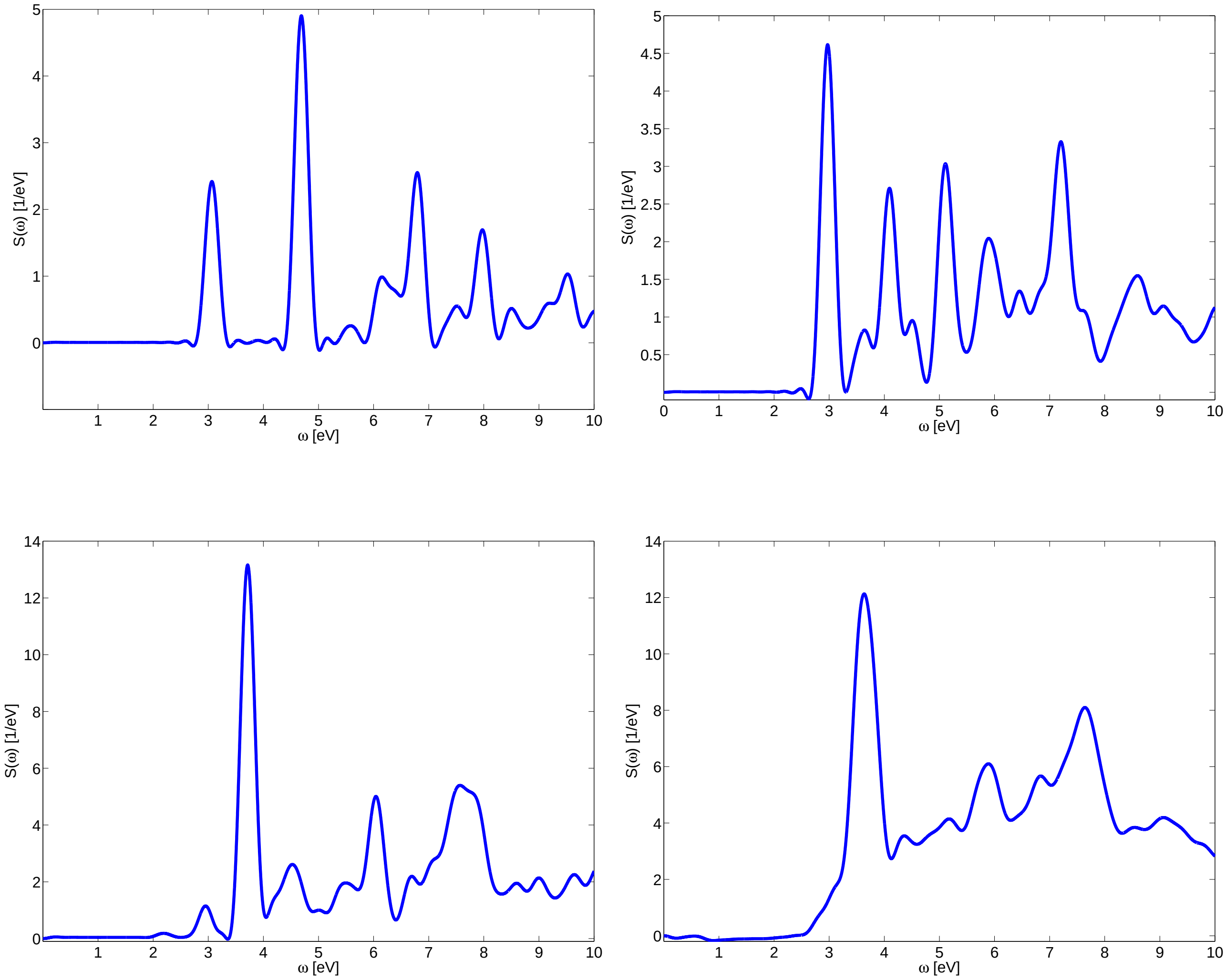

Figure 4.2: Optical absorption of silver clusters: on the top, left to right Ag_2, Ag_4; at the bottom left to right Ag_8 and Ag_{16}. Shown is oscillator strength function $S(\omega)$. Frequency is in electron-volt,strength function is in $(\mathrm{eV})^{-1}$.

response. The details could be found in [7]. The key differences from nonlinear response calculations are that : a) we use weak field of $\lambda = 3 \times 10^{-4}$ V/Å; b) we excite entire electronic spectrum by imposing one time position dependent phase shift on all ground state single particle orbitals $\phi(t_0) = e^{\imath\lambda\vec{r}}\phi_{g.s.}$ [2]. The computed spectrum for Ag_2, Ag_4 and Ag_{16} agrees well with results of Yabana et al. [47] and Baishya et al. [53]. Next we look for trends in absorption spectra that may represent evolution of cluster absorption spectra toward bulk silver spectra. The metal silver spectra is directly related to complex dielectric function. From dielectric function [54] we

---

[2] The method for calculation of optical absorption is further discussed in chapter 7.

computed the energy loss function measured in Electron Energy Loss Spectroscopy (EELS) experiments, and absorption coefficient. These are shown at the bottom of Figure 4.3. Absorption coefficient is not a typical experimental quantity for metal, but in our case it may be directly compared to oscillator strength function of clusters.

One may see that besides sharp dip at 3.81 eV, absorption of bulk silver forms a continuum. It falls as $\sim -\omega^4$ between 1 and 3.81 eV and then rises as $\sim \sqrt{\omega}$ between 3.81 and 6 eV. On another hand, small clusters have series of distinct peaks with absorption falling to near zero in the 4-6 eV range (Figure 4.2). However, starting with Ag_{16} and further progressing in Ag_{32} (Figure 4.3, top), the oscillator strength function fills out the gap 4-5 eV, while the peaks following the first start to blend into continuum. We may conclude that the cluster spectra remain very different from bulk. At the same time there are systematic changes in absorption spectra that become more pronounced when the size of the cluster increases. Still, it remains unclear how evolution of the cluster spectra will progress toward the metal spectra.

Table 4.2: Dependence of plasmonic peak on size of silver cluster. $S(\omega)$ - oscillator strength function. R-classical radius of Mie sphere.

Cluster	$\hbar\omega_p$ [eV]	$S(\omega)$ [1/eV]
Ag_2	3.063	2.417
Ag_4	2.967	4.612
Ag_8	3.712	13.16
Ag_{16}	3.68	12.09
Ag_{32}	3.486	15.26
Mie theory	3.5	$\sim R^3$

We also note that larger clusters start to behave like classical particles in at least one aspect. Table 4.2 and Figure 4.3 show that the first (plasmonic) peak approaches the position, and in case of Ag_{32} coincides with absorption peak of a uniform conducting ellipsoid described by classical Mie-Gans theory [55, 56]:

$$\sigma(\omega) = \frac{4\pi\omega R_1 R_2 R_3}{9c} \sum_{i=1}^{3} \left(\frac{\epsilon_2(\omega)}{(1 + G_i(\epsilon_1(\omega) - 1))^2 + (G_i \epsilon_2(\omega))^2} \right), \tag{4.1}$$

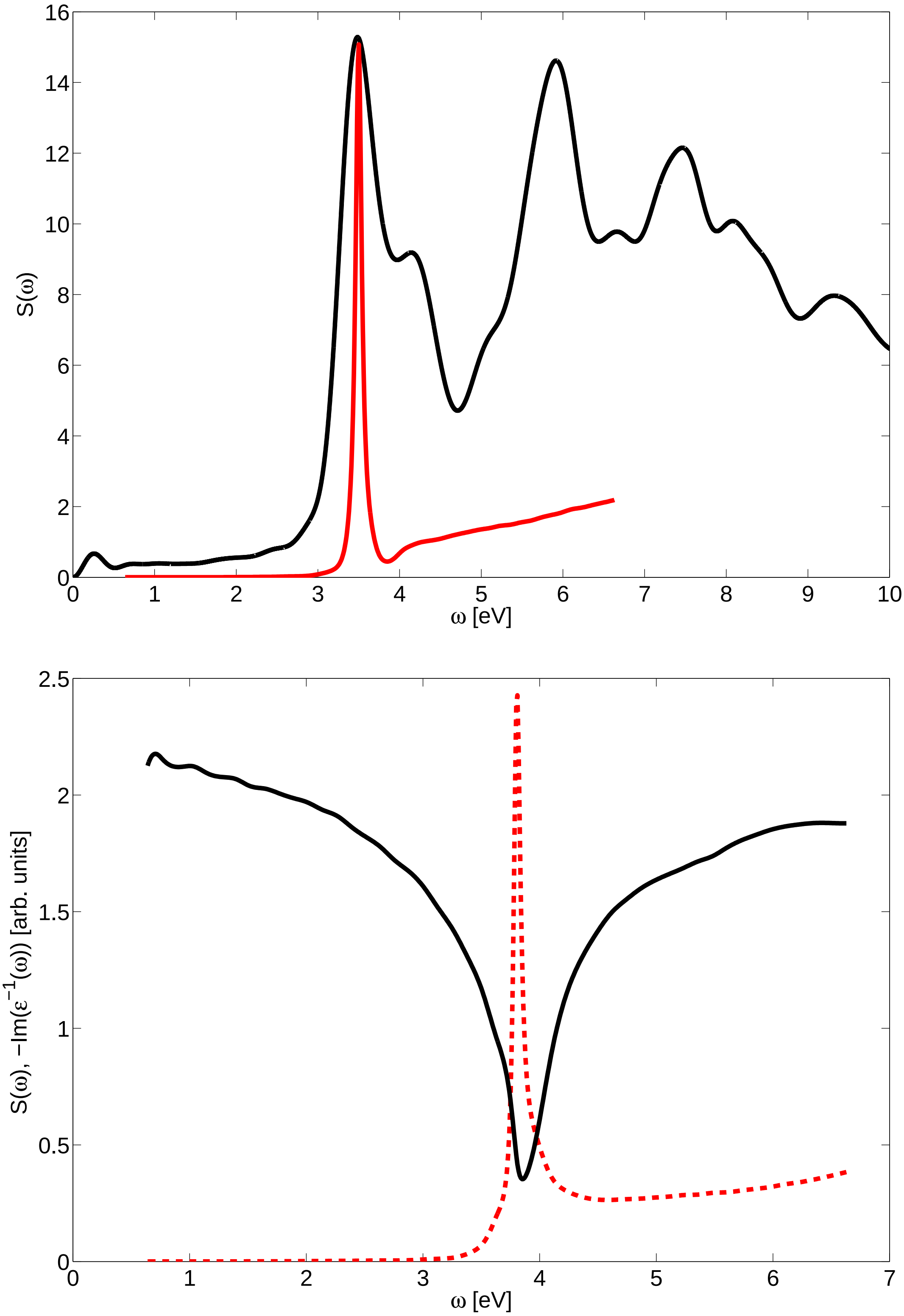

Figure 4.3: On the top: optical absorption of Ag_{32} cluster (black) and Mie theory prediction (red) for a sphere of radius R=4 Å. Shown is oscillator strength function $S(\omega)$. Frequency is in electron-volt, strength function is in $(\mathrm{eV})^{-1}$. At the bottom: absorption coefficient of bulk silver (black), and energy loss function of bulk silver $-\Im(\epsilon^{-1}(\omega))$ (red dash) .

where R_i are semi-axis of ellipsoid representing cluster, G_i is geometry dependent depolarization factors, σ is absorption cross-section, $\epsilon(\omega) = \epsilon_1(\omega) + \imath\epsilon_2(\omega)$ is dielectric function. It will be interesting to see whether the noted trends will continue for larger clusters, and whether the current method would yield realistic data for larger clusters.

4.2 Nonlinear response in $\mathrm{Ag}_{(n=2,4,8,16,32)}$

Table 4.3: Spatially averaged second hyperpolarizabilities $\chi_{||}^{(3)}$ of silver clusters at $\hbar\omega = 1.55$ eV. Data is in atomic units.

Cluster	$\chi_{\|\|}^{(3)}(-\omega)$	$\chi_{\|\|}^{(3)}(-3\omega)$
Ag_2	$8.8 \times 10^4 - 5.3 \times 10^3\imath$	$-1.3 \times 10^5 - 8.3 \times 10^5\imath$
Ag_4	$3.3 \times 10^5 - 4 \times 10^4\imath$	$-2.1 \times 10^5 - 1.6 \times 10^5\imath$
Ag_8	$3.2 \times 10^5 - 1.3 \times 10^4\imath$	$-3.0 \times 10^5 - 5.0 \times 10^5\imath$
Ag_{16}	$7.8 \times 10^5 - 7 \times 10^3\imath$	$-1.2 \times 10^5 - 5.4 \times 10^5\imath$
Ag_{32}	$1.1 \times 10^6 - 5 \times 10^4\imath$	$6 \times 10^3 - 1.5 \times 10^6\imath$

Next, we examine the nonlinear response. We focus on third order response because it is present in all clusters that we consider, and more importantly we are interested in IDRI processes as most relevant for optoelectronic applications. The excitation frequency of external field was set to $\hbar\omega = 1.55$ eV. Two electric field strengths were chosen: $\lambda = \{0.025, 0.05\}$ (V/Å) for Ag_{16} and Ag_{32}, and three fields we used for Ag_2, Ag_4, Ag_8: $\lambda = \{0.013, 0.025, 0.05\}$ (V/Å). The second hyperpolarizabilities were extracted using method II described in Chapter 2. The averaged second hyperpolarizabilities are presented in Table 4.3, and the characteristic third order nonlinear response is shown in Figure 4.4.

Since response of Ag_2 cluster is analyzed in Chapter 5, we start with Ag_4. The cluster shows regular response at ω with positive real part, substantial negative imaginary part, and partially distorted response at 3ω with imaginary and real parts being both negative and nearly equal in size. The magnitude of third order response is $\sim 10^5$ a.u..

Response of Ag_8 at ω is similar to Ag_4. At 3ω imaginary part dominates, and response is generally disordered. Both real and imaginary parts are negative. The magnitude of third order response is of the same order as Ag_4.

Response of Ag_{16} has divergence at near zero frequency. Because we are focusing on the third order, the second order response was not computed and is not shown. Response at ω is regular, with some imaginary part. At 3ω imaginary part dominates, but response remains regular. Both real and imaginary parts are negative. The magnitude of third order response is of the same order as Ag_4.

Similarly to Ag_{16}, the second order response of Ag_{32} was not computed and is not shown on the figure. Response at ω is irregular, has contribution from the fifth order. Imaginary part is 100 times smaller then real part. At 3ω imaginary part dominates, response remains regular. While the imaginary parts remains negative, the real part is positive and 1000 times smaller then imaginary. The magnitude of third order response is of the same order as Ag_2. The magnitude of third order response is $\sim 10^6$ a.u..

Absolute values of third order susceptibilities grow gradually with the size of the cluster from $\sim 3 \times 10^5$ a. u. in case of Ag_4 to 1.6×10^6 a.u. in case of Ag_{32}. Overall, clusters show similarities in nonlinear response, although they can be further differentiated into two groups. The small clusters Ag_4 and Ag_8 are closer to each other then larger clusters: Ag_{16} and Ag_{32}. The same classification is true for linear response.

4.3 Excited charged density dynamics and nonlinear response in strong fields

Next, we look at dynamics of electronic density response. Figure 4.5 shows snapshots of the density change for Ag_{32}: $\Delta\rho(\mathrm{t}) = \rho(t) - \rho_{g.s.}$, where $\rho_{g.s.}$ is the ground state density. The three snapshots at times 2.96, 9.83 and 11 fs correspond to $\{0.38, -2.88, 2.22\} \times 10^{-2}$ (V/Å) values of external field. The fourth snapshot is at the very end of simulation when the field is 10^{-7} (V/Å). The black color indicates positive excess of density, the white shows negative excess density, while the green color corresponds to no change in density in respect to the ground state. We would like to offer the following classification of the electronic excitations present in the Figure 4.5. We call the black-white pairs clearly seen in the middle of the cluster excited charge density structures (ECDS for short) [3]. The hallmark of ECDS is that they appear as a stable pair of an excited electron and depleted density created by the spatial displacement of the corresponding excited electron density. The depleted density has opposite sign to the negatively charged surrounding electron density. The white and gray clouds enveloping two and more atoms are another kind of excited density. These formations of excess and depleted density extend over several atoms and may be interior charged density oscillations. They do not have definite angular momentum. We call them c-modes. These are clearly seen at t = 11.0 fs. The four ECDS in the middle of the cluster owe their stability to the shielding effect of surrounding atoms. At the intensity of external field I $\sim 3.7 \times 10^{14}$ (W/m^2) electrons at outer atoms delocalize and tend to blend into the c-modes. When the fields are strongest, at 9.83 and 11 fs the ECDS change their shape, which points to a possibility that they go to higher energy levels, perhaps with higher angular momentum. This is seen as change from one white - one black dot to two white - two black dots. Without direct quantification it is not possible to determine which excitations play dominant role in nonlinear response. The ECDS certainly have greater density fluctuation then the smeared density excitations. Yet the ECDS are highly localized, while the smeared excitations are distributed over extended regions. Both kinds may equally contribute to the polarization response.

Here we list possible mechanisms of contribution of electronic excitations to the nonlinear optical response. The ECDS may contribute in at least two different ways. In strong oscillating field they tend to change orientation, replicating harmonic oscillations. The surrounding electrons distort the harmonic potential and as a result inducing "soft", "regular" nonlinearities [4]. Other, delocalized electrons may "collide" with the ECDS. In strong field the ECDS may go to the higher angular momentum levels that lead to dramatic changes in their electronic density distributions. This would lead to essential, strong nonlinearities. The collective c-modes have highly nonlinear dynamics and their contribution to polarization is likely to be always highly nonlinear.

---

[3] It is an open question whether ECDS are related to the Valence Bond Excitons [57, 58].

[4] Regular nonlinear polarization response is defined as part of the total polarization minus linear response *exactly* representable by a polynomial in electric field.

4.4 Summary

In this chapter, we have calculated absorption spectra of several silver clusters and noted that for clusters starting with n = 16, there exists positive correlation between size of the cluster and metallic features in absorption spectra. We calculated and analyzed third order susceptibilities at $\hbar\omega = 1.55$ eV. The susceptibilities are essentially complex, with absolute values positively correlating with the size of the cluster and ranging between 10^5 and 10^6 a.u.. We have examined time dependent density response and classified the electronic charge density excitations. We have proposed several mechanisms for contribution of electronic excitations to nonlinear optical response.

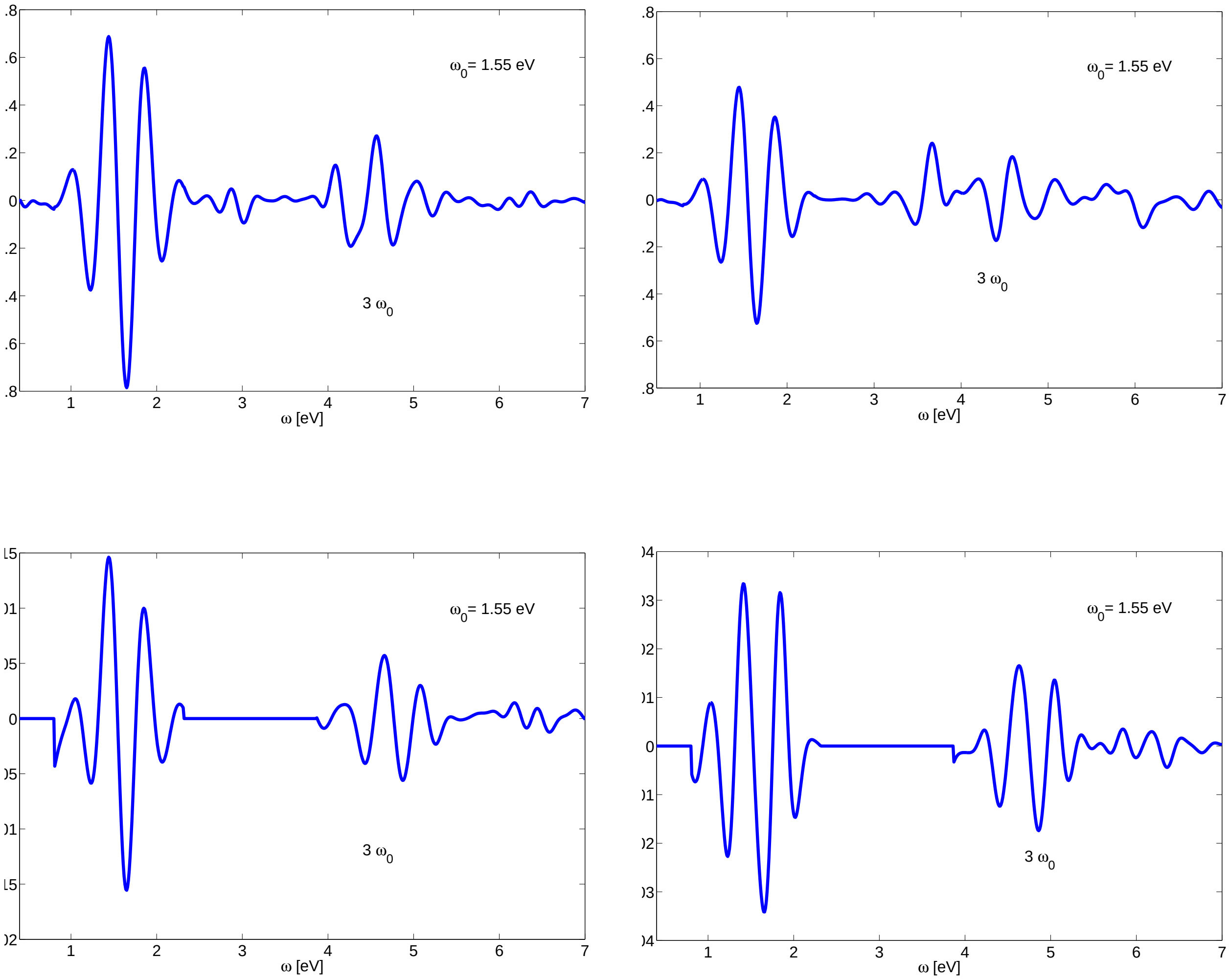

Figure 4.4: Third order nonlinear response of silver clusters. On the top, left to right: Ag_4, Ag_8. At the bottom, left to right: Ag_{16} and Ag_{32}. The response has not been calculated for [0.0, 0.7] eV and [2.2, 4.0] eV intervals for Ag_{16} and Ag_{32} graphs. Vertical axis displays real part of $P^{NL}(\omega)$. Polarization is in arbitrary units. Horizontal axis displays frequency in electron-volt.

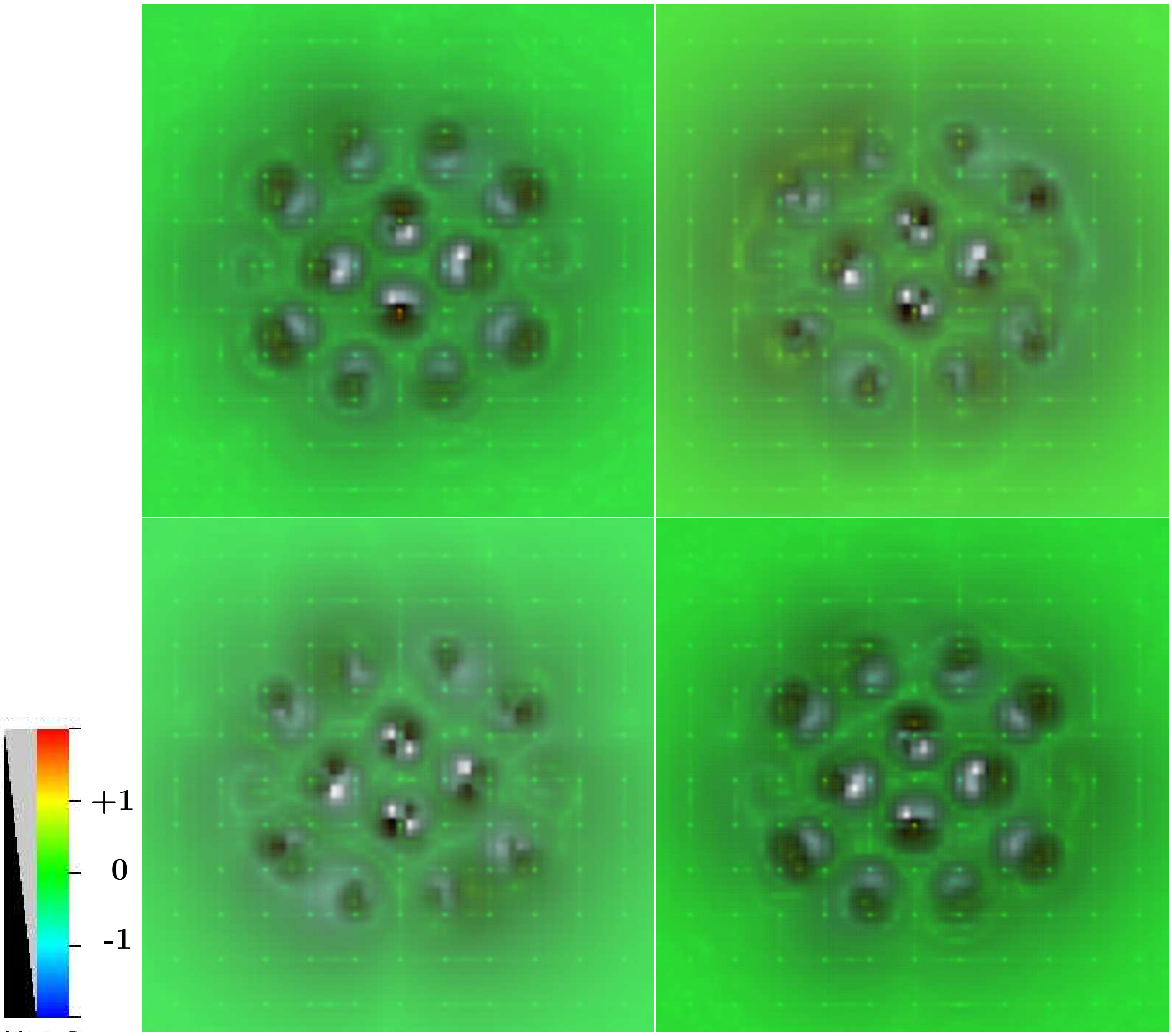

Figure 4.5: Charge-density excitations of Ag_{32} cluster in external field with photon energy $\hbar\omega_0$ =1.55 eV. Shown is (001) slice of density change $\Delta\rho(\mathrm{t}) = \rho(\mathrm{t})$ -$\rho_{g.s.}$, where $\rho_{g.s.}$ is the ground state density. External field of (0.05 V/Å) magnitude is in [100] direction. Size of each box is ∼1.6 nm. Depleted (negative) density change is shown in white, excess of density (positive) change is in black. On the top, left to right: t = 2.96 fs and 9.83 fs; on the bottom, left to right: t = 11.0 fs and 24.0 fs.

Chapter 5

FULLERENE CAGE

In this section we look at possible applications of the methodology developed and presented in previous chapters. As an example we investigate how nonlinear optical properties of C_{60} fullerene change upon placing into its interior a silver dimer. Design of such an exotic structure is motivated by a need for developing highly nonlinear materials for all optical switches. The desirable characteristic of *de novo* material is enhanced third order response at the same frequency as the exciting field.

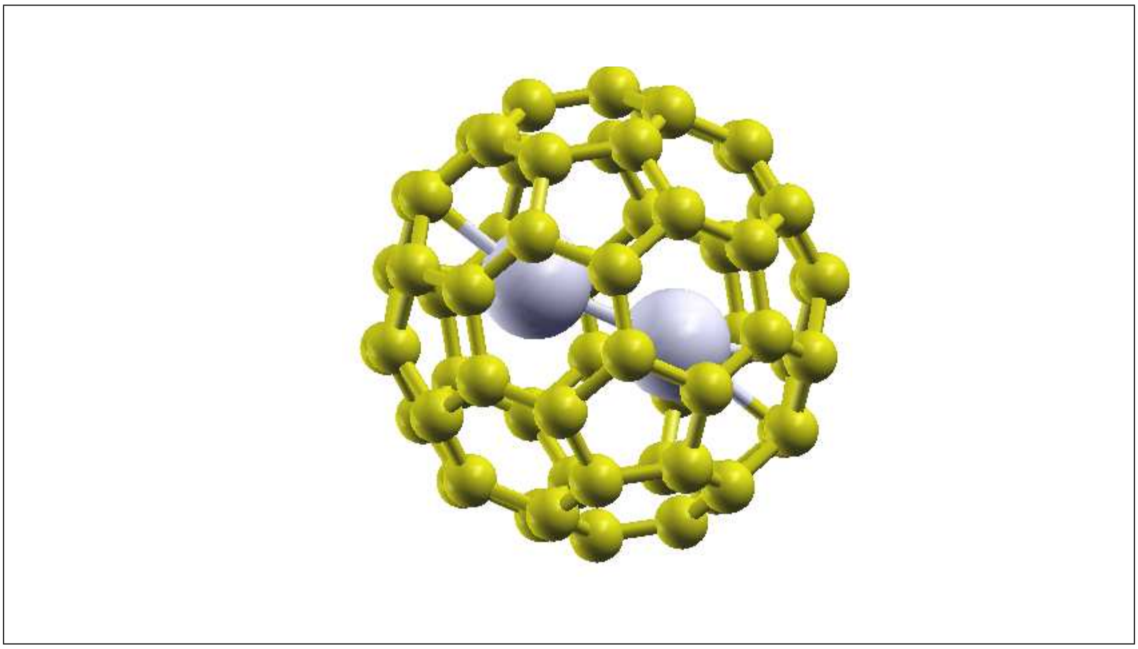

Figure 5.1: Structure of $C_{60}Ag_2$ fullerene.

C_{60} fullerene already has substantial third order response at ω, however, it will be interesting to see how it is affected by structural modifications. In particular, we would like to see if we can enhance IDRI/TPA by combining it with a material that has high nonlinear response - a silver cluster. Structurally fullerene serves as a cage for silver (Figure 5.1), keeping it from aggregation and allowing stochiometry control of carbon and silver. It also partially shields silver dimer from external field.

Table 5.1: Absolute values of second hyperpolarizabilities of caged silver. Data is in atomic units. R:THG/IDRI - ratio of nonlinear response at 3ω to ω. Degeneracy factor D=3 is included to facilitate comparison of responses.

Molecule	$\lvert D \times \chi^{(3)}(-\omega)\rvert$	$\lvert\chi^{(3)}(-3\omega)\rvert$	R:THG/IDRI
C_{60}	6.2×10^4	9.8×10^4	1.6
$C_{60}Ag_2$	1.9×10^5	5.2×10^5	2.7
Ag_2	7×10^4	8×10^4	1

Absorbance spectra (Figure 5.2) show that losses of the caged silver at relevant telecommunication frequency of $\hbar\omega = 1.17$ eV are not very high and in practice may be reduced by mixing it with "empty cages".

Time dependent polarization response was obtained using methods of RT-TDDFT as described in previous chapters. The molecules were placed in a cubic supercells with side L=16Å, and grid step of 0.25 Å. Ground states were constructed by using 262, 240 and 22 valence electrons for $C_{60}Ag_2$,C_{60} and Ag_2 respectively. Troullier-Martins pseudopotentials [59] were used to represent effective Coulomb potential of inner core electrons and nuclei. Perdew-Zunger [39] Exchange-Correlation functional was used. Conjugate Gradients was used as total energy minimization algorithm. External quasi-monochromatic field with FWMH = 10fs, $\hbar\omega = 1.17$ eV, three values of amplitude : $\lambda = 0.026, 0.053, 0.079$ (V/Å) and six directions of the field were used for real time propagation. Molecules was propagated for 20000 steps with dt = 0.0012 fs step size. Calculations were done using NERSC[1] Edison computer. For $C_{60}Ag_2$,

Table 5.2: Major diagonal component of second hyperpolarizability $\chi^{(3)}_{zzzz}$ of caged silver. Data is in atomic units. Degeneracy factor D=3 is included to facilitate comparison of responses.

Molecule	$D \times \chi^{(3)}_{zzzz}(-\omega)$	$\chi^{(3)}_{zzzz}(-3\omega)$
C_{60}	$1.5 \times 10^5 - 7 \times 10^2 \imath$	$2.3 \times 10^5 - 1.0 \times 10^4 \imath$
$C_{60}Ag_2$	$5.8 \times 10^5 - 1.3 \times 10^5 \imath$	$1.6 \times 10^6 - 1.0 \times 10^6 \imath$
Ag_2	$2.4 \times 10^5 - 8.1 \times 10^3 \imath$	$-5.8 \times 10^5 - 3.0 \times 10^5 \imath$

---

[1] National Energy Research Supercomputing Center

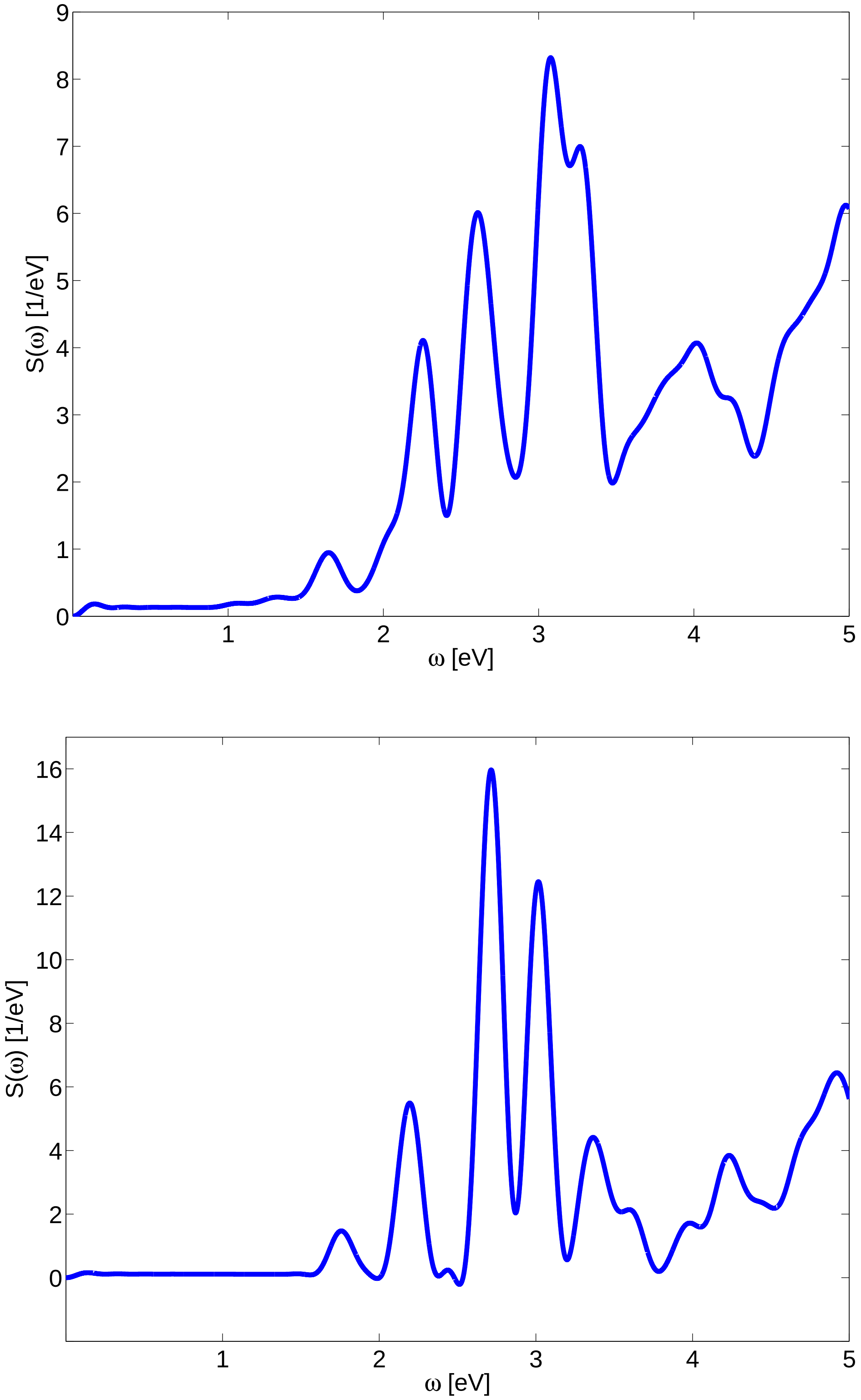

Figure 5.2: On the top is shown absorption spectra of C_{60} fullerene. At the bottom is absorption spectra of $C_{60}Ag_2$ fullerene.

2358 processors were needed for 130 min 7 sec. Nonlinear response was extracted using Method I from chapter 2.

Table 5.3: Spatially averaged second hyperpolarizabilities $\chi^{(3)}_{||}$ of caged silver. Data is in atomic units. Degeneracy factor D=3 is included to facilitate comparison of responses.

Molecule	$D \times \chi^{(3)}_{\|\|}(-\omega)$	$\chi^{(3)}_{\|\|}(-3\omega)$
C_{60}	$6.2 \times 10^4 - 7 \times 10^2 \imath$	$9.8 \times 10^4 - 4 \times 10^3 \imath$
$C_{60}Ag_2$	$1.8 \times 10^5 - 6 \times 10^4 \imath$	$1.9 \times 10^5 - 4.8 \times 10^5 \imath$
Ag_2	$7.1 \times 10^4 - 5.9 \times 10^3 \imath$	$5.8 \times 10^4 - 4.1 \times 10^4 \imath$

5.1 Nonlinear response of caged silver

We start analysis with Ag_2. Considering the fact that it is a two atom molecule, nonlinear response is very strong, with absolute value of third order susceptibilities $\sim 10^4$ a.u. (Table 5.1). Figure 5.3 shows that nonlinear response at ω_0 is mostly regular, and is practically real. Nonlinear response at $3\omega_0$ is irregular, it has a contribution from fifth order and a large imaginary part. Also, fifth order response clearly shows up at $5\omega_0$. At least five different amplitudes of external field are needed to resolve the contributions from fifth order. Because we used three, it makes susceptibility values ambiguous at $3\omega_0$. Averaged susceptibilities are listed in Table 5.3. Real parts are positive and imaginary parts are negative at both ω_0 and $3\omega_0$.

Analysis of C_{60} shows that fullerene third order response is the same magnitude as Ag_2. From Figure 5.4 one may see that third order response is regular. It has low dispersion both at ω and 3ω. The response is nearly isotropic as one may infer by comparing values in Tables 5.3 and 5.1.

Finally, investigate $C_{60}Ag_2$. Caged silver third order response is larger then C_{60} by a factor of 3 at ω and by factor of five at 3ω. Third order response is somewhat irregular, especially at 3ω. It is dispersive both at ω and 3ω. The response is anisotropic. It also has significant fifth order response at 5ω.

"Doping" fullerene with silver enhances third order response. The increase is larger than the simple sum of responses from dimer and fullerene. Data in Table 5.1

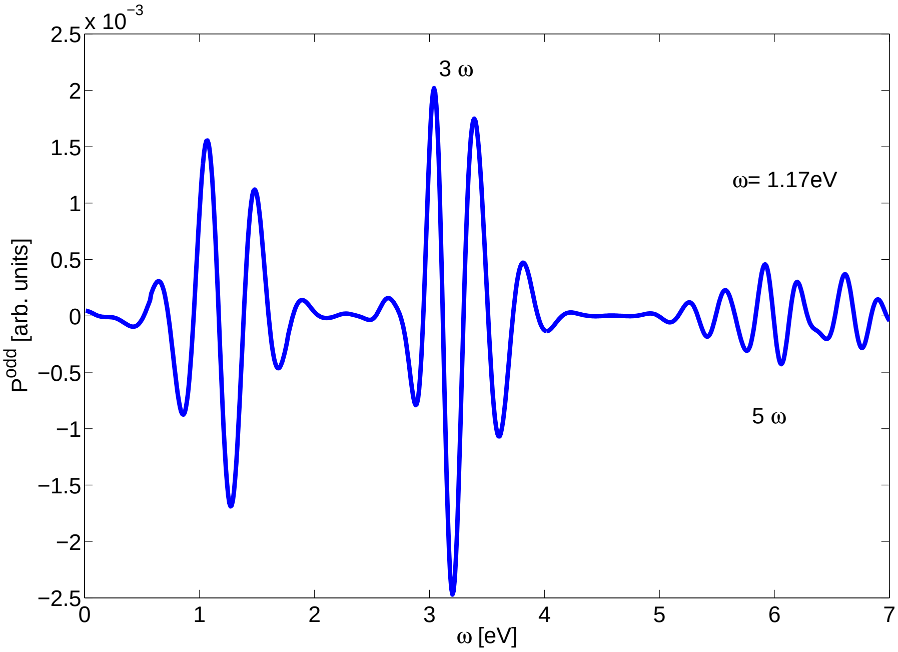

Figure 5.3: Odd order nonlinear optical response of Ag_2 cluster.

shows increase the ratio of third order processes at 3ω to ω; however, this increase is ambiguous due to unresolved contribution from fifth order.

5.2 Stabilization of excited charged density dynamics and enhanced nonlinear response

We now turn to analysis of dynamics of charged density excitation. Figures 5.6 and 5.7 show snapshots of density change for C_{60} and $C_{60}Ag_2$ respectively. The density change is calculated between time t and the ground state density: $\Delta\rho(t) = \rho(t) - \rho_{g.s.}$, where $\rho_{g.s.}$ is the ground state density. The three snapshots at times 2.96, 11.00 and 17.25 fs correspond to $(0.38, -2.88, 2.22) \times 10^{-2}$ (V/Å) values of external field. The fourth snapshot is at the very end of simulation when the field is vanishing. The black color indicates positive excess of density, white shows negative excess density, while green corresponds to no change in density in respect to the ground state. Field is perpendicular to the slice. We start with C_{60}. At t_1=2.96 fs four bright white spots and eight black spots are what we call excited charge density structures (ECDS). Extended gray clouds near interior surface are "distributed" or "smeared" excitations.

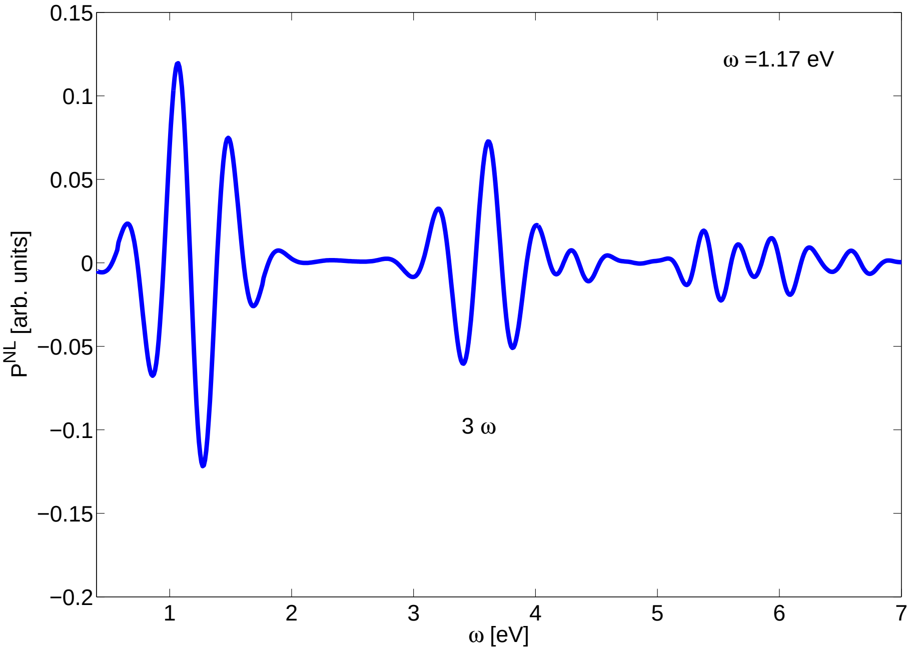

Figure 5.4: Third order optical response of C_{60} fullerene.

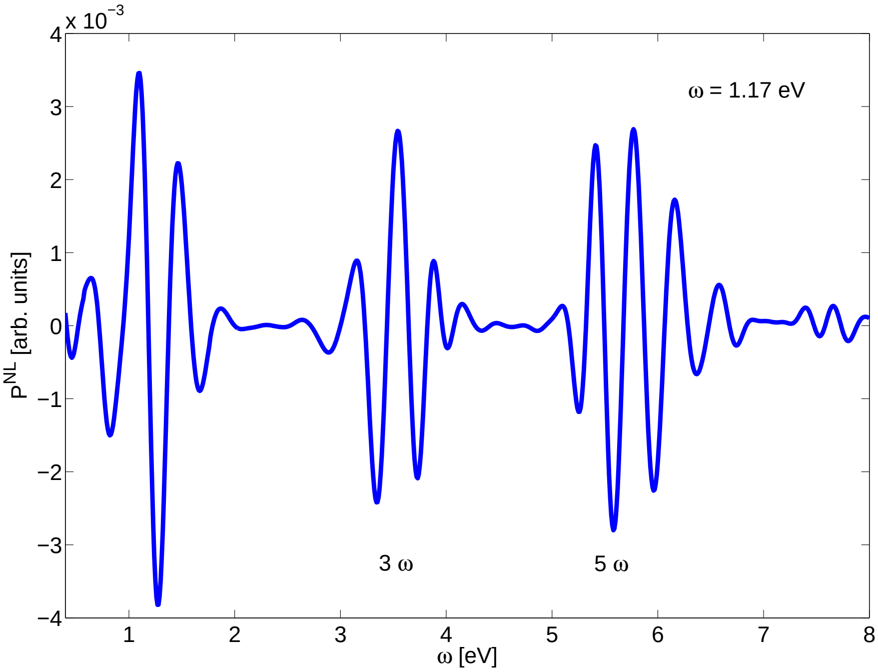

Figure 5.5: Third order optical response of $C_{60}Ag_2$ fullerene. Shown is z-projection of third order polarization with external field along [001] direction.

At t_2, the field flips, and so do the ECDS. White spots turn to black and vice verse. At t_3 the field flips again and the picture become similar to t_1. The last t_4 snapshot corresponds to the end of simulation and vanishing field. Spatially distributed charge density excitations have disappeared, while the ECDS are in process of recombination. $C_{60}Ag_2$ dynamics is noticeably different. Some of the excited electrons are delocalized. The interior is practically filled with "smeared" charged density fluctuations. The number of the ECDS is smaller, but they appear in different shape that may be higher angular momentum states. They have similar dynamics - flipping along the field. At the end of simulation smeared excitations persist, although their space "mode" becomes asymmetric. Since contribution of these excitations to polarization is essentially nonlinear, they represent significantly larger part of the excited density in case of caged silver, and that translates into a remarkable enhancement of nonlinear response.

5.3 Summary

In this chapter, we studied a prospective mechanism of enhancement of third order response of fullerene by adding silver dimer into its interior. We calculated and analyzed third order susceptibilities at $\hbar\omega = 1.17$ eV. Third order response at ω has increased in absolute value from 6.2×10^4 to 1.9×10^5 a.u.. We have examined the time dependent density response, and have shown that enhancement of nonlinear response in caged silver is attributed to domination of the electronic excitations by the interior charge density modes.

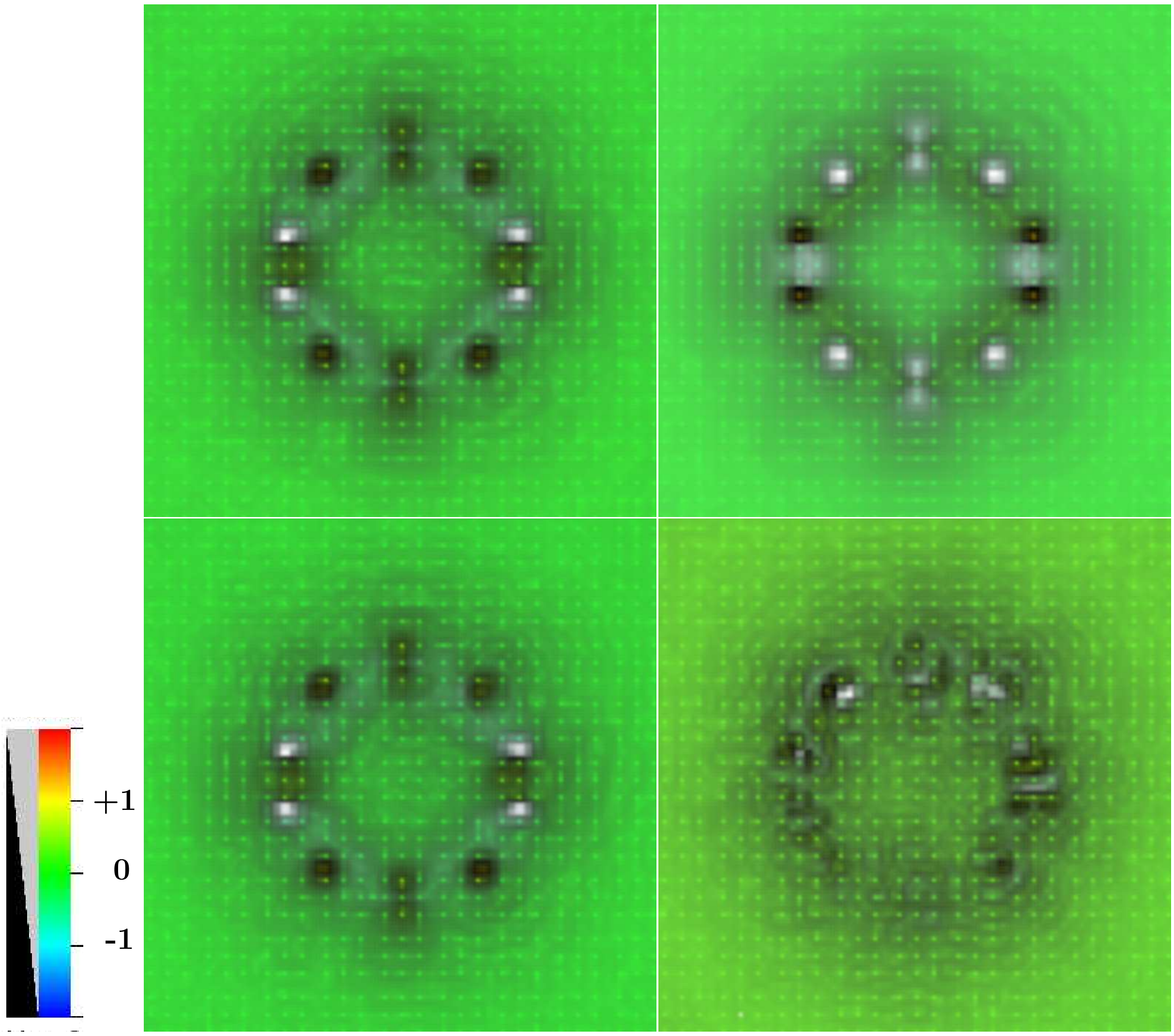

Figure 5.6: Charge-density excitations of C_{60} fullerene in external field with photon energy $\hbar\omega_0 = 1.17$ eV. Shown is (1 0 0) slice of density change $\Delta\rho(\mathrm{t}) = \rho(t) - \rho_{g.s.}$, where $\rho_{g.s.}$ is ground state density. External field of 0.05 (V/Å) magnitude is in [1 0 0] direction. Side of each box is $\sim$ 1.3 nm. Depleted (negative) density change is shown in white, excess of density (positive) change is in black. On the top, left to right: t= 2.96 fs and 11.00 fs. On the bottom, left to right: t= 17.25 fs and 24.0 fs.

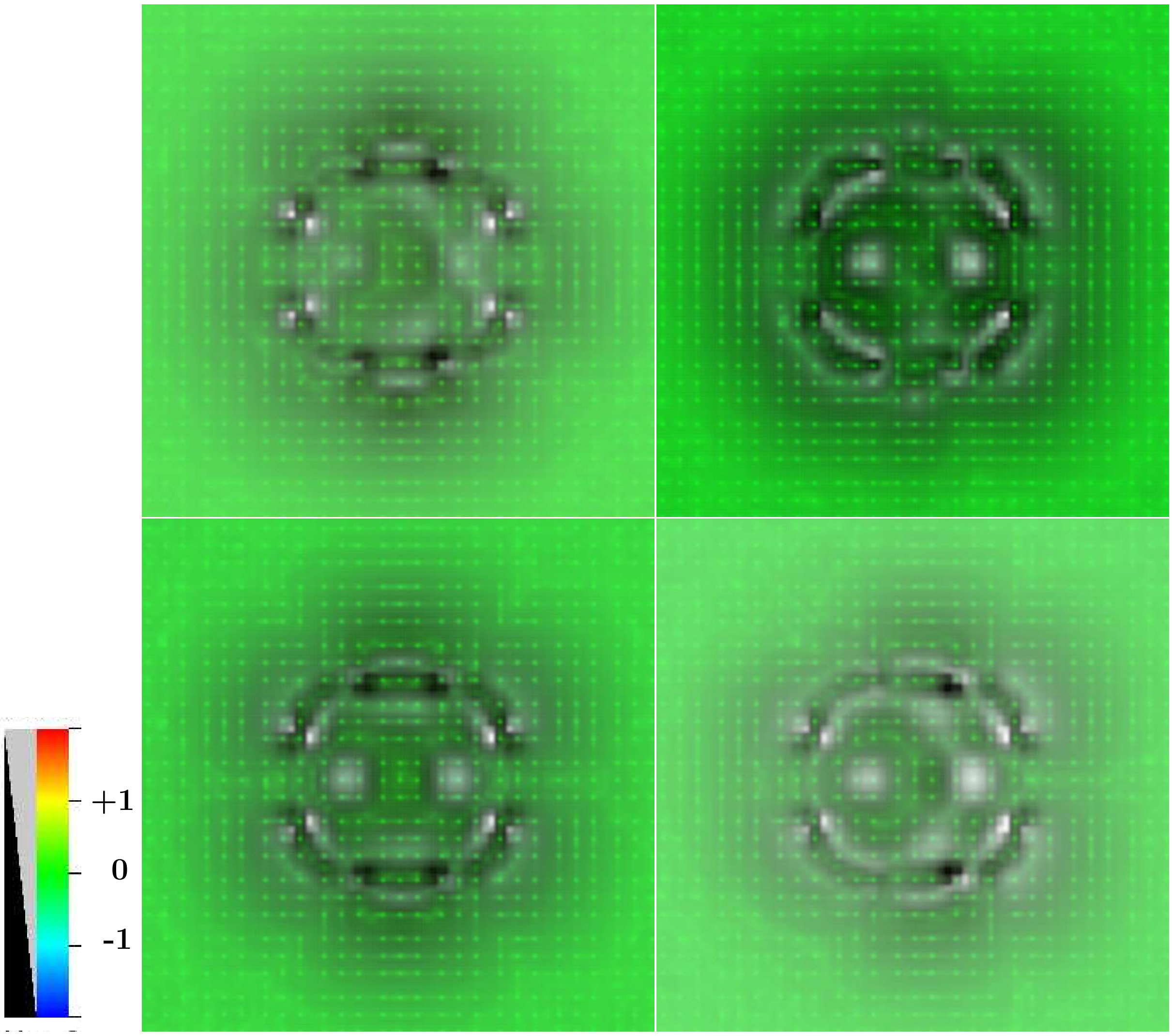

Figure 5.7: Charge-density excitations of $C_{60}Ag_2$ cage in external field with photon energy $\hbar\omega_0$ =1.17 eV. Shown is (1 0 0) slice of density change $\Delta\rho(t) = \rho(t) - \rho_{g.s.}$, where $\rho_{g.s.}$ is ground state density. External field of 0.05 (V/Å) magnitude is in [1 0 0] direction. Side of each box is ~1.3 nm. Depleted (negative) density change is shown in white, excess of density (positive) change is in black. On the top (left to right) t = 2.96 fs and 11.00 fs; on the bottom (left to right) t = 17.25 fs and 24.0 fs.

Chapter 6

NONLINEAR RESPONSE IN SOLIDS

Most of the materials used in electronics and optoelectronics are periodic solids. Nonlinear susceptibilities of solids are difficult to calculate from first principles. In the past five decades a number of theories for calculation of susceptibilities was devised [60, 61, 62, 63, 64, 65, 66, 67]. Starting with earlier independent particle approximation (IPA) theories that exhibited non-physical divergences [60, 63] and progressing to recent many-body perturbation theories [68, 69], accuracy and complexity of calculations grew. Yet for a variety of non-linear processes there is still no single *ab initio* method that can simultaneously provide a reasonable match with experiment and numerical efficiency. The theories meet several kinds of challenges. These include the necessity to account for excitonic and local field effects which are best addressed by Bethe Salpeter Equation (BSE) [69, 70]. However, there is no BSE calculated spectra beyond linear response at this time, and the issue is more commonly addressed by scissors-operator in band structure methods [64] as well as in Density-Functional Theory (DFT) based methods with scissor corrections [68]. Incidentally, DFT (and time-dependent DFT)-based methods, particularly earlier ones, have their own difficulties related to calculation of polarization. One is insufficiency of density as the only independent variable [71, 72]. Another is that external perturbation taken in dipole approximation as a scalar field $-\vec{r}\cdot\vec{E}(t)$ violates periodicity of crystal field and therefore can not be used in such form [73]. In addition, the definition of polarization as a matrix element of position operator $\hat{P} = -\frac{e}{8\pi^3}\sum_{n,k}\langle u_{n,k}|\hat{x}|u_{n,k}\rangle$, where $u_{n,k}$ is periodic part of Bloch function of band n with wave vector $\vec{k}$, used in early calculations of $\hat{\chi}^{(2)}$ [60] was found to be invalid for infinite crystals and had to be amended either by Wannier functions representation [65, 74] or by replacing it with $\hat{P} = \frac{e\,i}{4\pi^3}\sum_n \int \langle u_{n,k}|\frac{\partial}{\partial k}|u_{n,k}\rangle\, d^3k$ [75]. Currently, all of the published theories are perturbative and as such they share one feature that complicates their numerical implementation: the expressions for susceptibilities are cumbersome and their complexity grows rapidly with increasing order of non-linearity.

The aim of this chapter is to introduce a non-perturbative method based on real space, real time, time dependent DFT (RT-TDDFT). The method is an extension of a method that was used for calculation of hyperpolarizabilities of molecules [43, 31]. The extension is largely based on the theory for strong electromagnetic fields in crystalline solids developed by K. Yabana *et al* [73, 76, 32]. The key element of the theory is the Schrödinger-Maxwell dynamics cast as a system of coupled time dependent Kohn-Sham and wave equations that are solved simultaneously in real time. The theory uses density $\rho(\vec{r}, t)$ and polarization current $\vec{j}(\vec{r}, t)$ as basic variables. It also uses the vector potential $\vec{A}_{ext}(t) = -\int_0^t \vec{E}(t')dt'$ as external interacting field to avoid violation of translational symmetry [73]. In real time methods the single particle wave functions are continuously evolved under action of evolution operator, and dynamical effects such as screening are included. Some effects of electron-hole interactions are therefore present, albeit at the level corresponding to the exchange-correlation functional used in calculations. The formalism is extraordinary simple and the calculations are easily implemented on parallel computers. Moreover, the cost of computing the k^{th} order response or $(k+1)$ is approximately the same, and often several orders of $\hat{\chi}^{(k)}$ could be extracted in a single set of calculations.

6.1 Coupled Schrödinger - Maxwell dynamics

The formalism is restricted to dipole approximation and optical frequencies. The electromagnetic (EM) interaction is allowed to be arbitrary large. The vector potential is taken as the sum of external and induced polarization parts, and Coulomb gauge is employed:

$$\vec{A}(t) = \vec{A}^{pol}(t) + \vec{A}_{ext}(t) \tag{6.1}$$

$$\vec{E} = -\frac{\partial \vec{A}}{\partial t} \tag{6.2}$$

$$\nabla \cdot \vec{A} = 0 \tag{6.3}$$

Practical considerations also suggest that for sufficiently small region of the crystal lattice (the size of a few primitive unit cells), the vector potential can be taken spatially uniform $\vec{A} = \vec{a}\, A(t)$, where $\vec{a}$ is a constant unit vector. The well known expression for the wave vector of crystal electron [77] $\vec{k}$ in electric field $\vec{E}$:

$$\hbar \, \frac{d\vec{k}}{dt} = -e\vec{E} \tag{6.4}$$

provides motivation for the following form of the Bloch states [1]:

$$\psi_{k,b}(\vec{r},t) = u_{\vec{k},b}(\vec{r},t)\; e^{i\,\vec{r}\,(\frac{\vec{A}}{\hbar}+\vec{k})} \tag{6.5}$$

$$u_{\vec{k},b}(\vec{r}+\vec{R},t) = u_{\vec{k},b}(\vec{r},t), \tag{6.6}$$

where $\vec{R}$ is the lattice vector. Inserting (6.5) into single particle time dependent Schrödinger equation

$$\imath\hbar \frac{\partial \psi_{k,b}(\vec{r},t)}{\partial t} = \left(\frac{p^2}{2\,m} + \vec{E} \cdot \vec{r} + \hat{V}(\vec{r},t) \right) \psi_{k,b}(\vec{r},t) \tag{6.7}$$

and using (6.2), after some algebra yields the reduced equations:

$$i\hbar \, \frac{\partial u_{\vec{k},b}(\vec{r},t)}{\partial t} = \frac{1}{2\,m} \left(-i\,\hbar\,\nabla + e\,\vec{A} + \hbar\,\vec{k} \right)^2 u_{\vec{k},b}(\vec{r},t) + \hat{V}(\vec{r},t)\, u_{\vec{k},b}(\vec{r},t). \tag{6.8}$$

The potential is the sum of electrostatic, exchange-correlation and ionic part

$$V(\vec{r},t) = \hat{V}_H(\rho(\vec{r},t)) + \hat{V}_{xc}(\rho(\vec{r},t)) + \hat{V}_{ion}(\vec{r},t), \tag{6.9}$$

and it needs to conform to the periodicity of lattice:

$$\hat{V}(\vec{r}+\vec{R},t) = \hat{V}(\vec{r},t). \tag{6.10}$$

---

[1] Using $\vec{A} = \vec{a}\, A(t)$ to integrate (6.4) gives $\vec{k}(t) = \frac{e}{\hbar}\vec{A}(t) + \vec{k}_o$, which is inserted into (6.5).

Electrostatic $\hat{V}_H(\rho(\vec{r},t))$ and exchange-correlation $\hat{V}_{xc}(\rho(\vec{r},t))$ parts in Adiabatic Local Density Approximation (ALDA) are scalar functions of density

$$\rho(\vec{r},t) = \sum_{\vec{k}}^{BZ} \sum_{b}^{occ} u^*_{\vec{k},b}(\vec{r},t)\, u_{\vec{k},b}(\vec{r},t) \tag{6.11}$$

and therefore maintain the same symmetry as electron density. The cumulative effect of nuclear charges and inner electrons is represented by pseudopotential contribution, which comes in our case in two parts: local and non-local. The local part is made periodic by explicit construction in reciprocal space and by subsequent back transformation into real space. The non-local part $\hat{V}_{nlc}u_b$ depends on single particle density matrix $\sum_{k,b} \psi^*_{k,b}(\vec{r},t)\psi_{k,b}(\vec{r'},t)$ and is taken as

$$\hat{V}_{nlc}(u_b(\vec{r},t)) = \int e^{-\imath\,\vec{r}\,(\frac{\vec{A}}{\hbar}+\vec{k}_0)}\, V_{nlc}(\vec{r},\vec{r'})\, u_{\vec{k},b}(\vec{r'},t)\, e^{\imath\,\vec{r'}\,(\frac{\vec{A}}{\hbar}+\vec{k}_0)}\, d\vec{r'}^3. \tag{6.12}$$

Equations (6.8) with (6.12) describe the dynamics of crystal electrons in the field $\vec{A}(t)$. For the dynamics to be realistic, this field has to be a superposition of the external and polarization fields. An essential ingredient in this formalism is the current.

The current is obtained from the expectation value of velocity operator $\hat{v}$:

$$\int \vec{j}(\vec{r},t)dr^3 = \frac{1}{2}\sum_{k,b}\int \left(\psi^*_{k,b}\,\hat{v}\,\psi_{k,b} - \psi_{k,b}\,\hat{v}\,\psi^*_{k,b}\right) dr^3. \tag{6.13}$$

The velocity operator breaks into three parts [2]

$$\hat{v} = \frac{\imath}{\hbar}\left[\hat{H},\vec{r}\right] = \frac{\imath}{\hbar}\left[\frac{p^2}{2\,m} + \frac{\vec{A}\cdot\vec{p}}{m} + \hat{V}_{nlc},\vec{r}\right], \tag{6.14}$$

where $\hat{H}$ is the corresponding single particle Hamiltonian.

---

[2] Since A^2 - term is scalar, it does not contribute to current. In Hamiltonian appearing in (6.13) we made replacement $\vec{p} \to \vec{p} - e\vec{A}$. Momentum operator is defined as: $\vec{p} = -\imath\hbar\nabla$, where gradient operator acts on Cartesian coordinates of single particle wavefunction. Summation is over the occupied states b and reciprocal vectors k in the first Brillouin zone.

Mirroring the structure of the velocity operator, the current density is divided into three parts:

$$\vec{j}(\vec{r},t) = \vec{j}_{\psi}(\vec{r},t) + \vec{j}_{EM}(\vec{r},t) + \vec{j}_{nlc}(\vec{r},t). \tag{6.15}$$

For the non-local current density we have:

$$\vec{j}_{nlc} = \frac{\imath}{2\,\hbar}\sum_{k,b}\left(\psi^{*}_{k,b}(\hat{V}_{nlc}\vec{r} - \vec{r}\hat{V}_{nlc})\psi_{k,b} - c.c.\right) = -\frac{1}{\hbar}\sum_{k,b}\Im\left(\psi^{*}_{k,b}(\hat{V}_{nlc}\vec{r} - \vec{r}\hat{V}_{nlc})\psi_{k,b}\right). \tag{6.16}$$

After unfolding the nonlocal potential nonlocal the current density becomes:

$$\vec{j}_{nlc}(\vec{r},t) = -\frac{1}{\hbar}\sum_{\vec{k},b} Im[\; u^{*}_{\vec{k},b}(\vec{r}',t)\; e^{-i\,\vec{r}\,(\frac{\vec{A}}{\hbar}+\vec{k})} \int V_{nlc}(\vec{r},\vec{r}')\; u_{\vec{k},b}(\vec{r}',t)\; e^{i\,\vec{r}'\,(\frac{\vec{A}}{\hbar}+\vec{k})}\;\vec{r}'\; d\vec{r}'^{3} - \\ -u^{*}_{\vec{k},b}(\vec{r},t)\; e^{-i\,\vec{r}\,(\frac{\vec{A}}{\hbar}+\vec{k})}\;\vec{r} \int V_{nlc}(\vec{r},\vec{r}')\; u_{\vec{k},b}(\vec{r}',t)\; e^{i\,\vec{r}'\,(\frac{\vec{A}}{,\hbar}+\vec{k})}\; d\vec{r}'^{3}]. \tag{6.17}$$

Two other contributions are:

$$\vec{j}_{\psi}(\vec{r},t) = \frac{\hbar}{m}\sum_{\vec{k},b} Im(u^{*}_{\vec{k},b}\,\nabla\, u_{\vec{k},b}) \tag{6.18}$$

$$\vec{j}_{EM}(\vec{r},t) = \frac{1}{m}\sum_{\vec{k},b} u^{*}_{\vec{k},b}\, u_{\vec{k},b}\;\vec{A}(t) \tag{6.19}$$

Matter responds to the external field by producing polarization field. Classically, the rise of polarization field could be described by the inhomogeneous wave equation. The source in this case is the "quantum-mechanical" current arising from the flow of the electrons:

$$\nabla^{2}\vec{A}^{pol} - \frac{1}{c^{2}}\frac{\partial^{2}\vec{A}^{pol}}{\partial t^{2}} = -\mu_{0}\,\vec{j}^{pol} \tag{6.20}$$

The current density $\vec{j}^{pol}$ serves as a coupler between Schrödinger and Maxwell dynamical variables, and is proportional to the total current density calculated above: $\vec{j}^{pol} = e\vec{j}$. When the vector potential is approximately constant throughout a region (such as the unit cell), $\nabla^2 \vec{A}$ vanishes and from inhomogeneous wave equation we have:

$$\frac{\partial^2 \vec{A}^{pol}}{\partial t^2} = e \frac{\vec{j}_\psi + \vec{j}_{EM} + \vec{j}_{nlc}}{\epsilon_0} \tag{6.21}$$

The macroscopic induced vector potential A^{pol} and macroscopic polarization current are obtained by averaging over the unit cell:

$$\langle \vec{j}_{pol}(t) \rangle = e \int_{Cell} \vec{j}(\vec{r}, t)\, d^3\vec{r} \tag{6.22}$$

$$\Omega\, A_i^{pol}(t) = \int_{Cell} \vec{A}^{pol}(t) \cdot \hat{i}\, d^3\vec{r}, \tag{6.23}$$

where Ω is the unit cell volume, and $\hat{i}$ is a unit vector. Now we can re-write (6.8) and (6.21) as a system of coupled equations:

$$\begin{cases} i\hbar\, \frac{\partial u_{\vec{k},b}(r,t)}{\partial t} = \frac{1}{2\,m} \left(-i\,\hbar\,\nabla + e\,\vec{A} + \hbar\,\vec{k} \right)^2 u_{\vec{k},b}(r,t) + \hat{V}(\vec{r},t)\, u_{\vec{k},b}(r,t) + \\ \qquad + \int\, e^{-i\,\vec{r}\,(\frac{\vec{A}}{\hbar} + \vec{k}_0)}\, V_{nlc}(\vec{r}, \vec{r}')\, u_{\vec{k},b}(\vec{r}', t)\, e^{i\,\vec{r}'\,(\frac{\vec{A}}{\hbar} + \vec{k}_0)}\, d\vec{r}'^3 \\ \frac{\partial^2 A_i^{pol}(t)}{\partial t^2} = \frac{\langle \vec{j}_{pol}(t) \rangle_i}{\Omega\, \epsilon_0} \end{cases} \tag{6.24}$$

The system of equations (6.24) represents a closed set of equations governing the dynamics of crystal electrons in electric field. The meaning of V_{nlc} could be expanded to include the non-local contributions from prospective exchange-correlation potentials [78].

The first equation in (6.24) is solved by continuous application of evolution operator $\hat{U}$ to the periodic part of Bloch wave functions:

$$|u_{\vec{k},b}(r,t)\rangle = \hat{U}(t, t_0) |u_{\vec{k},b}(r, t_0)\rangle. \tag{6.25}$$

In this work, the evolution operator for a finite time interval is taken as a product of infinitesimal evolution operators [79] $\hat{U}(t, t_0) = \prod_n \hat{U}(t_{n+1}, t_n)$ with Taylor expansion representation for the propagator,

$$\hat{U}(t_{n+1}, t_n) = \sum_{k=0}^{N} \frac{(-\frac{i}{\hbar}\Delta t \hat{\mathcal{H}}[\rho](\vec{r}, t))^k}{k!}, \tag{6.26}$$

where N is the highest order of expansion. Although this approximation is non-unitary, its properties and limitations are very well studied [79, 7]. This representation is attractive for two reasons. First, it does not involve a matrix inversion and therefore is highly scalable and computationally efficient. Second, the errors are controlled by the expansion order N. The non-unitarity is two orders higher then N. For example, choosing $N = 4$ results in non-unitarity (and correspondingly in norm non-conservation) of the sixth order:

$$\hat{U}^{-1}\hat{U} = \frac{\hat{\mathcal{H}}^6}{72\hbar^6} - \frac{\hat{\mathcal{H}}^8}{576\hbar^8}. \tag{6.27}$$

The error in wave-function at each step is $\sim O((\frac{\Delta t \hat{\mathcal{H}}}{\hbar})^5)$, and could, in principle be matched to machine precision by adjusting the time step Δt.

Macroscopic polarization

$$\vec{P}(t) = \frac{\int_{t_0}^{t} \langle \vec{j}_{pol}(t') \rangle \, dt'}{\Omega}, \tag{6.28}$$

and total electric field $\vec{E}(t) = \vec{E}_{ind}(t) + \vec{E}_{ext}(t)$ are calculated at every time step (Fig.6.1). This also allows calculation of the dielectric constant $\epsilon(\omega)$.

6.2 Response Functions

The Response functions are calculated by one of the methods described above. To highlight the specifics of calculations in case of periodic solids we outline the major steps in application of one of the methods.

The relation $\vec{D}(t) = \epsilon_0 \vec{E}(t) + \vec{P}(t)$ in case of non-linear response may be written as

$$\vec{D}(t) = \epsilon_0 \left(\vec{E}(t) + \int \hat{\chi}^{(1)}(\tau)\, \vec{E}(t-\tau) d\tau + \int\int \hat{\chi}^{(2)}(\tau,\tau')\, \vec{E}(t-\tau)\, \vec{E}(t-\tau') d\tau\, d\tau' + \ldots \right), \tag{6.29}$$

where the rank $n+1$ tensors $\hat{\chi}^{(n)}$ are the nonlinear susceptibilities. Equation (6.29) could be expressed as series in terms of nonlinear polarization tensors $P^{(n)}_{ij\ldots k}$:

$$D_i(t) = \epsilon_0\, E_i(t) + \sum_j P^{(1)}_{ij}(t) + \sum_{jk} P^{(2)}_{ijk}(t) + \sum_{jkl} P^{(3)}_{ijkl}(t) + \ldots, \tag{6.30}$$

Each n^{th} term in the series is effectively a function of n^{th} power of electric field $E(t)$. The second order correction is quadratic in the *total* field $\vec{E}(t)$:

$$P^{(2)}_{ijk}(t) = \epsilon_0 \int_0^\infty d\tau_1\, d\tau_2\; \chi^{(2)}_{i,j\,k}(\tau_1,\tau_2)\, E_j(t-\tau_1)\, E_k(t-\tau_2)\,. \tag{6.31}$$

In frequency domain, the linear response is local:

$$\chi_{ij}(-\omega;\,\omega) = \frac{P_i(\omega)}{\epsilon_0\, E_j(\omega)}. \tag{6.32}$$

The n^{th} order response in frequency domain takes the following form:

$$P^{(n)}_{ik\ldots m}(\omega) = \frac{\epsilon_0}{(2\pi)^{(n-1)}} \int \chi^{(n)}_{ik\ldots m}(-\omega;\,\omega_1,\ldots,\omega-\sum_{j=1}^{n-1}\omega_j)\, E_k(\omega_1)\, \ldots\, E_m(\omega-\sum_{j=1}^{n-1}\omega_j)\, d\omega_1 \ldots d\omega_{n-1}. \tag{6.33}$$

In case of quasi-monochromatic excitation the response is well localized (Fig. 6.5), and in non-resonant case $\chi^{(n)}$ could be taken out of the integral similarly to the case of finite structures described in chapter 2 One may write the total field as

$$E_j(\omega) = \frac{\varepsilon_j\, g(\omega)}{\epsilon(\omega)}, \tag{6.34}$$

where $g(\omega)$ is normalized Fourier transform of external field $\vec{E}^{ext}(t)$, and ε_j its amplitude;

$$E^{ext}_j(t) = -\frac{\partial A^{ext}_j}{\partial t} = \varepsilon_j\, \sin(\omega_0\, t)\, e^{-\frac{(t-t_0)^2}{\sigma^2}}. \tag{6.35}$$

Inserting (6.35) into (6.33) leads to

$$P^{(n)}_{ik\ldots m}(\omega) = \frac{\epsilon_0\, \chi^{(n)}_{ik\ldots m}(-\omega)\, \varepsilon_k\, \ldots\, \varepsilon_m\, C_n(\omega)}{(2\pi)^{(n-1)}} = a^{(n)}_{ik\ldots m}(\omega)\varepsilon_k\, \ldots\, \varepsilon_m, \tag{6.36}$$

where C_n is

$$C_n(\omega) = \int \frac{g_k(\omega_1)\, \ldots\, g_m(\omega - \sum_{j=1}^{n-1} \omega_j)}{\epsilon(\omega_1)\, \ldots\, \epsilon(\omega - \sum_{j=1}^{n-1} \omega_j)}\, d\omega_1 \ldots d\omega_{n-1}. \tag{6.37}$$

Next, one proceeds by propagating the electronic wave-functions multiple times with varying amplitudes ε_j. The total polarization data is put into vector $\vec{\mathcal{P}} = \{P_i(\omega; \vec{E}(\eta))\}$. Matrix of external field values $\hat{\Theta}$ and vector of coefficients $\vec{\mathcal{X}} = (a^{(1)}_{11}, a^{(1)}_{12}, a^{(1)}_{13}, \ldots, a^{(2)}_{111}, a^{(2)}_{112}, a^{(2)}_{113}, \ldots, a^{(3)}_{1111}, a^{(3)}_{1112}, a^{(3)}_{1113}, \ldots)$ are formed. Solving $\hat{\Theta}\, \vec{\mathcal{X}} = \vec{\mathcal{P}}(\omega)$ for $\vec{\mathcal{X}}$ gives the response function $\hat{\chi}^{(n)}$:

$$\chi^{(n)}_{ik\ldots m}(-\omega) = \frac{(2\pi)^{(n-1)}\, a^{(n)}_{ik\ldots m}(\omega)}{\epsilon_0\, C_n(\omega)}. \tag{6.38}$$

6.3 Numerical Details and Results

In this section results for THG for a semiconductor and an insulator are presented and compared to available experimental results. The crystals belong to $m3m$ crystal class, and $\hat{\chi}^{(3)}$ generally have four independent components. However, for THG process these are further reduced to two components $\chi^{(3)}_{1111}(-3\,\omega)$ and $\chi^{(3)}_{1122}(-3\,\omega)$.

The calculations are performed using the grid representation for the real space [80]. A cubic, eight atom cell was used with the following parameters. For Si, side of the cube is L= 5.43Å, and grid with 20^3 points has been used. This corresponds to grid spacing with $\Delta x = 0.2715$Å. For carbon diamond, cube with L= 3.57Å side, and 16^3 grid points ($\Delta x = 0.2231$Å) has been used. In reciprocal space, uniformly spaced k-grids with three different densities were used (see Table 6.1 and discussion below). Core electrons were represented by Troullier-Martins pseudopotentials [59]. The ground state and band structure were calculated using Conjugate Gradient method [81] and 500 iterations. This provided convergence of total energy greater then 10^{-3} eV. Perdew-Zunger 1981 [39] V_{xc} functional has been used. Identical Exchange-Correlation functionals were used both for ground state and for time propagation.

The external vector potential was obtained by numerical integration of the electric field:

$$A_{ext}(t) = -E_{max} \int_0^t dt' \sin(\omega_0 \, t') \, e^{-\frac{(t'-T_0)^2}{\sigma^2}}, \tag{6.39}$$

Amplitude of the field E_{max} was varied from -0.78 (V/Å) to +0.78 (V/Å), typically in steps of 0.26 (V/Å). This strong field [3] ensured prominent appearance of third order response (Fig.6.4). The field may have one component in [100] direction, which is sufficient for calculation of major diagonal components of $\chi^{(3)}$. To find out $\chi^{(3)}_{1122}$ the field has to have two components. These were taken in [100] and [010] directions. Parameter σ controls the width of Gaussian envelope in (6.39). The envelope should be chosen to be wide enough to allow at least one full oscillation of the exciting field, and at the same time to temporally localize the field within the simulation interval. Ideally, the field's amplitude should gradually increase and reach the maximum in the first half of the simulation interval. Then, it should be reduced to zero several femtoseconds before the simulation end. This prevents density shocks, and allows the density to relax to its final state before the simulation end.

The first equation describing crystal electrons interacting with external field (6.24) is solved by application of the evolution operator. The evolution operator is taken as in (6.26), with N = 4 . Kinetic operator in the Hamiltonian is approximated by the nine point finite difference. The second equation in (6.24) is integrated by a three-point finite-difference scheme. The total number of time steps was 22000. The size of iteration step was Δ t =0.0012 fs resulting in 26.4 fs simulation time. This choice of parameters guaranteed stable propagation [4]. Varying the size of the step within stability interval $0 < \Delta t < \sqrt{\frac{2}{9} m (\Delta x)^2} \sim 0.004\,\text{fs}$ [32] does not significantly

---

[3] The field corresponds to laser intensity of 3.3 × 10^{17} (W/m^2). Single 10 fs pulse will have corresponding fluence of 0.3 (J/cm^2). For comparison, Ti:sapphire laser with 0.6 mJ energy per 40 fs pulse focused at 1 mm^2 have fluence of 0.06 (J/cm^2). However, laser beam could be focused to spots of just 45 micron diameter producing fluence of 1-1.5 (J/cm^2) [82].

[4] Stable propagation means that the induced polarization largely follows the field, and typically vanishes at the end.

impact results [43]. One feature of the method is that it permits probing the dielectric

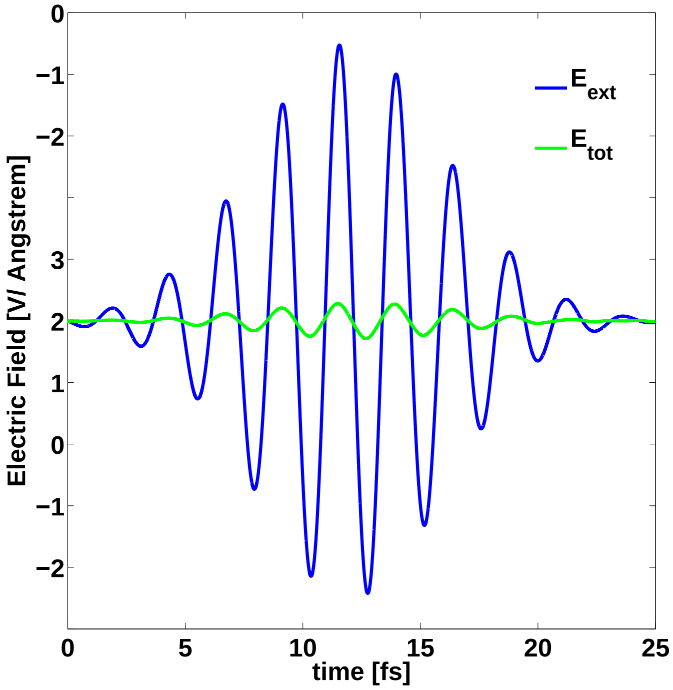

Figure 6.1: Comparison of total $E_{tot}(t)$ and external $E_{ext}(t)$ electric fields for Si. Total field is shown in light green, and external in blue. At the peak, ratio $E_{ext}/E_{tot} \sim 16$.

property of the material in a small interval near excitation frequency. Figure 6.1 shows time dependent external laser and total electric fields in Si. The total field is almost in phase with laser field indicating low absorbance. The total field is reduced by 16 fold in comparison to the external field. This is somewhat larger then the experimental dielectric constant $\epsilon(\omega) = 14.1$, but is consistent with the results obtained by Yabana et al. [32]. Thus, dielectric function at the excitation frequency ω_o is computed prior to, and could be later used for computing $\chi^{(n)}$. Figure 6.2 shows comparison of the computed $\epsilon(\omega)$ and the experiment within small frequency range centered at excitation frequency. The method overestimates the experimental data by 9.7 % in case of silicon, and by 14.8% in case of carbon diamond. The transfer of energy from laser pulse to matter can also be examined by the method. Figure 6.3 shows excitation

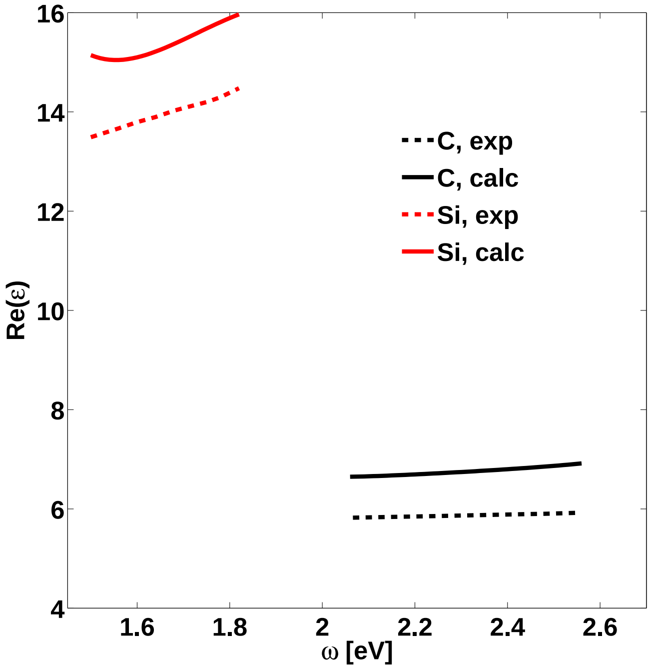

Figure 6.2: Real part of dielectric function $\epsilon(\omega)$. Data for silicon is shown in red and for carbon diamond in black. The experimental values taken from [12] are shown by dashed line, computed values by solid line. Quasi-monochromatic probe can be used to calculate dielectric function within a small neighborhood of excitation frequency. Data shown is for excitation frequency for Si at 1.7 eV and for diamond at 2.27 eV. The experimental dielectric constants are from [12].

energy per atom under simulated laser field. Excitation reaches its maximum at the height of the laser pulse, and persists after the external laser field is reduced to zero, similar to results of Shinohara et al. [76].

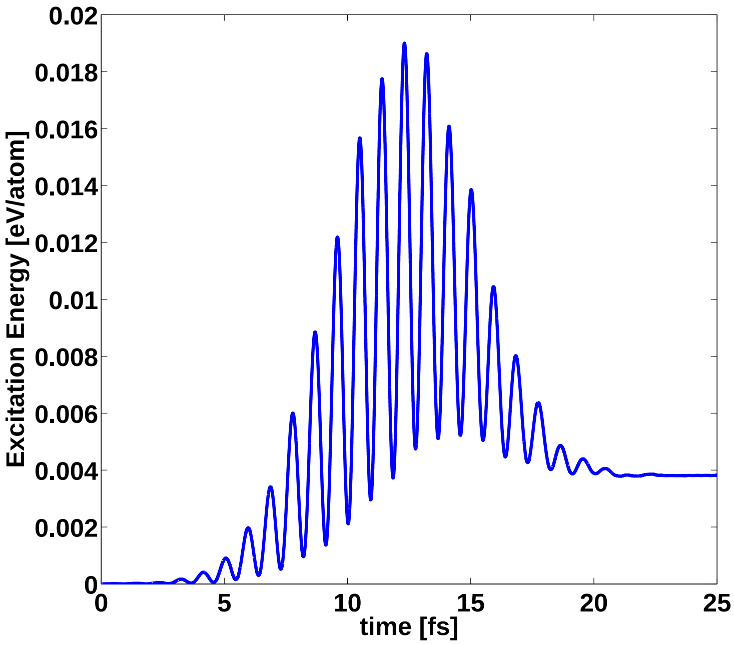

Figure 6.3: Electronic excitation energy per atom as a function of time. Data shown is for carbon diamond. The excitation remains after the laser pulse is turned off.

The key feature of the method is the realistic representation of the polarization response of solid under laser excitation in the entire optical range of frequencies. First, time-dependent macroscopic polarization $\vec{P}(t)$ is obtained from (6.28), and subsequently Fourier-transformed. Figure 6.4 shows typical frequency dependent polarization response in Si. The laser frequency is $\hbar\omega = 1.7$ eV. The response is well localized within the series of intervals corresponding to odd multiples of laser frequency $\hbar\omega$. The response is dominated by the first order; inset also shows appearance of the third order at approximately 100x scale. The shape of the linear response peak closely matches the shape of external electric field. The shape of the real part of third order response is similar to the imaginary part of third power of external electric field. In order to decompose the macroscopic polarization into the sum of higher orders

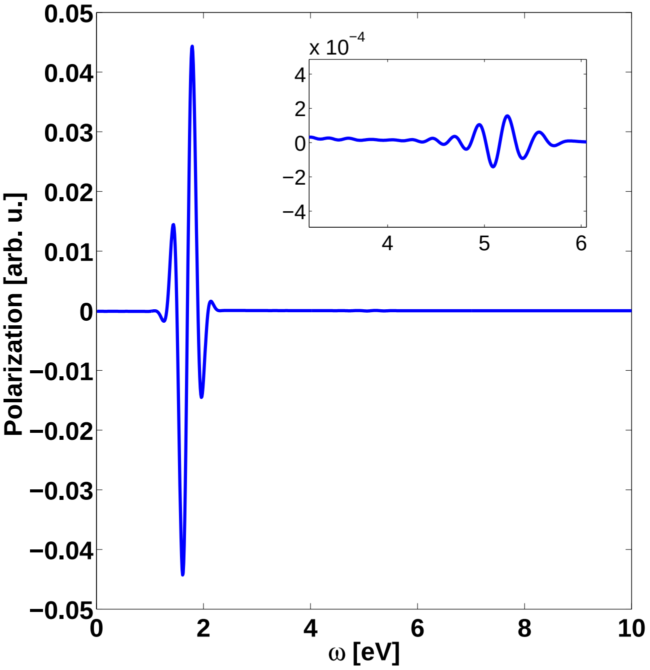

Figure 6.4: Nonlinear response in Si under simulated quasi-monochromatic laser excitation. The excitation energy is $\hbar\omega_0 = 1.7$ eV. Shown is real part of polarization $P(\omega)$. Inset shows 100x magnified frequency interval where THG response develops. The second order response is notably absent.

$\vec{P} \rightarrow \sum_n P^{(n)}$, three propagations with different amplitudes of the laser field are performed simultaneously, and 3x3 matrix is used to extract $\chi^{(3)}$ by solving (2.13). If one were to use the numerical differentiation or the least squares fitting method, four to six propagations would be needed. From Fig.6.5, it is clear that the nonlinear part of polarization is dominated by the third order, and the second order is practically absent, as it should be in a crystal with inversion symmetry. The third order response appears at both fundamental frequency ω and at third harmonic 3ω. The integrals C_n needed for calculation of $\hat{\chi}^{(n)}$ from (6.38) are computed numerically. They account for screening effects as well as for the finite width of quasi-monochromatic pulse.

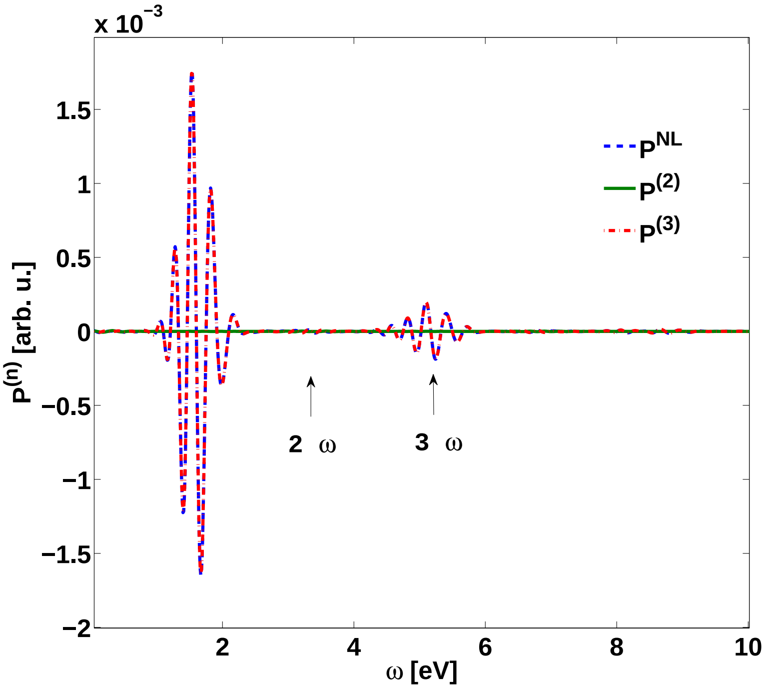

Figure 6.5: Decomposition of nonlinear polarization $P^{NL} = P_{total} - P^{(1)}$ into second and third order. The second order vanishes due to inversion symmetry. The third order $P^{(3)}$ at $3\omega_0$ is responsible for THG. Data shown is for Si. The second order is shown in green, third order is red dash and P^{NL} is blue.

In Table 6.1 the calculated susceptibilities are compared with experimental data as well as with Tight Binding band structure calculations from [7]. $\chi^{(3)}$ were calculated using k-grids with three densities using 4^3, 8^3 and 16^3 points. In principle, major diagonal components could be calculated with symmetry reduced grids. This gives a considerable savings. For example, the 16^3 grid may be represented by only 578 k-points. However, the symmetry reduction is not always possible because intense laser field adds to internal crystal field and alters its symmetry. As a result, some of the k-points that are transformed into each other by the original symmetry operations become independent and are needed to be included in calculations [5]. In case of major diagonal components like $xxxx$, the laser field may have only a single component along x axis allowing use of the symmetry reduction. This is not possible when two orthogonal components of external field are needed, such as in case of $xxyy$ and other off-diagonal tensor components. The data presented in this paper were obtained using uniform grids.

Overall, comparison between the computed results with experiment may be considered satisfactory for these type of calculations. Data for Si shows that both $\chi^{(3)}_{1111}$ and $\chi^{(3)}_{1122}$ are about 2.3 times smaller than experimental values for 16^3 grid. In case of diamond agreement with experiment is somewhat better. For 16^3 grid computed $\chi^{(3)}_{1111}$ component is 1.6 times smaller than experiment. Nevertheless, the ratio $\chi^{(3)}_{1122}/\chi^{(3)}_{1111}$ agrees with experiment within 2.5% for both silicon and carbon diamond. The ratio is an intrinsic property of the material, and is therefore an important measure of the reliability of calculations.

Increasing the k-point densities generally improves quality of simulation and reliability of results, and it is expected that at higher k-point densities the differences with experimental values will be reduced. However, the major shortcoming of the method is due to limitations of TDDFT theory itself, most importantly of inadequacy of the exchange-correlation functionals. It is very well known that Local Density Approximation drastically underestimates band gap in semiconductors, therefore leading to

---

[5] This should be clear from the form of Bloch wavefunctions (6.5): the k-vector is a function of time dependent vector potential, which has different symmetry than the original crystal symmetry.

Table 6.1: Third order susceptibilities $\chi^{(3)}_{1111}(-3\omega;\omega,\omega,\omega)$. The energy, $\hbar\omega$, is in eV; and $\chi^{(3)}$ is in 10^{-14} esu. The experimental data for $\chi^{(3)}$ of diamond is taken from [5]; and for Si from [6]. TB are the results of Tight Binding band structure calculations from [7]. ALDA are the results of present work. N$_K$ is the number of k-points.

			$\chi^{(3)}_{1111}(10^{-14}$ esu)			$\chi^{(3)}_{1122}$ (10^{-14} esu)			$\chi^{(3)}_{1122}/\chi^{(3)}_{1111}$		
	$\hbar\omega$	N_K	ALDA	TB	Exp.	ALDA	TB	Exp.	ALDA	TB	Exp.
Si	1.7	16^3	260	200	600 ± 260	124	142	290 ± 30	0.48	0.71	0.48
		8^3	208			92			0.44		
		4^3	460			211			0.46		
C	2.27	16^3	2.8	0.175	4.6 ± 0.6	1.1	0.075	1.84 ± 0.2	0.39	0.43	0.40
		8^3	2.6			1.8			0.69		
		4^3	4.4			1.4			0.32		

the major discrepancy with experiment in susceptibilities calculations. One may expect that more sophisticated exchange-correlation functionals or/and quasi-particle corrections such as scissor operations will significantly improve agreement with experiment. Additional sources of discrepancy between the theory and experiment are due to the following factors: a) approximation used in extracting $\chi^{(n)}$ according to (6.36), b) absence of nuclear motion, c) the coarseness of the real space grid, d) spatial independence of vector potential $\vec{A}$, and e) absence of photonic feed-back. Nevertheless the calculated values of $\chi^{(3)}$ are at least of the same order of magnitude as experimental values, which is not always the case even with semi-empirical methods, such as Tight-Binding.

6.4 Summary

A novel, non-perturbative *ab initio* method for computing nonlinear optical susceptibilities was described. The methodology is based on the theory for strong electromagnetic fields in solids [32]. The centerpiece of the theory is Maxwell-Schrödinger dynamics representing electron-photon interaction at quasiclassical level. The frequency dependent macroscopic polarization response is computed from polarization current for entire optical range of frequencies and is decomposed in a sum of linear and higher order polarizations $P^{(n)}_{ik...m}(\omega)$. The use of quasi-monochromatic excitation allows an easy separation of nonlinear polarization contributions with different parity. This greatly simplifies analysis of the nonlinear response and calculation of susceptibilities $\chi^{(n)}$. The newly developed extraction method for $\chi^{(n)}$ allows to cut computation costs in comparison to fitting or numerical differentiation. The numerical examples presented in this work support the methodology. Two crystals - silicon and carbon diamond were studied by the method. In both cases the calculated values of $\chi^{(3)}$ were compared to the experimental data and found to be of correct order of magnitude. The discrepancy with experiment is approximately 1.6 - 2.3 fold for $\chi^{(3)}$ values. Yet the method reproduces $\chi^{(3)}_{1122}/\chi^{(3)}_{1111}$ ratio within 2.5 % for both materials. The mismatch with experimental data is attributed to the general failure of TD-DFT in representation of band structure of solids near fundamental band gap. It is expected that quasiparticle corrections as well as exact solution of (6.33) will improve the accuracy of $\chi^{(n)}$.

Chapter 7

DOMAIN DECOMPOSITION APPROACH TO TDDFT

The majority of TDDFT implementations use atom-centered basis sets for representation of the Kohn-Sham (KS) orbitals, as this is a common practice in quantum chemistry. Real space grids and plane wave bases are also popular choices for representing the orbitals in TDDFT calculations. In calculations based on plane waves or real space grids the number of basis functions is typically much larger than in atom-centered basis sets, and can easily exceed 10,000, even in small molecules such as benzene. The large number of basis states becomes a bottleneck of calculation of time propagation of wave function. In time propagation one has to calculate the action of $\exp(-iH\Delta t)$ operator on orbitals $|\Psi\rangle$, where H is Hamiltonian of the system and Δt is time step. Various techniques have been developed to approximate this operator including straightforward polynomial expansions of the exponential and Crank-Nicolson [42] approach. Once Hamiltonian is represented as a matrix using appropriate basis states, time propagation involves ether inversion of $(1 + iH\Delta t)$ (Crank-Nicholson) or repeated application of Hamiltonian to calculate $H^n|\Psi\rangle$ (polynomial approximation). The efficacy of calculations then crucially depends on the basis representation, and we are interested in basis states which lead to Hamiltonian matrices for which inversion and/or multiplication can be implemented with the highest efficiency.

In this chapter we introduce and test the multidomain decomposition method to calculate optical absorption properties using the time-dependent density functional theory. In the multidomain decomposition approach one divides the system into smaller overlapping or non-overlapping subdomains. The Kohn-Sham equations can be solved independently in each subdomain. Using subdomain eigenfunctions as basis states one obtains especially structured sparse block-matrix representation of

Hamiltonian. Using sparse block-matrix structure of Hamiltonian both inversion and matrix-multiplication can be carried very efficiently. This allows us to do TDDFT calculations on large systems, which has not been possible using the conventional approaches.

To test the merit of the proposed approach we have compared the result of TDDFT calculations using three different basis sets. The first set uses the box basis functions that are used in the multidomain decomposition approach. These box basis functions are optimized by solving the Kohn-Sham equation in subdomains. We have developed two ways to construct these basis functions. One is to use finite difference subdomain eigenvectors and another is to use linear combinations of Lagrange functions to represent the box eigenvectors. Both ways have their advantages. The finite difference works well for small molecules and is the first choice in exploratory and developmental phases as it reduces to classical finite difference scheme when number of boxes is set to one. The Lagrange functions, on another hand provide a very accurate description of the wave function in the subdomains and are ideal for large complex systems. The introduction of these box basis functions is motivated by computational advantages and physical intuition.

Use of Lagrange functions [83] is not limited to representation of subdomain vectors and could be used as ordinary basis functions for the entire system. This is our second set. In this case the computational approach is identical to well known atomic orbital case. The Lagrange functions are defined on a real space grid. Each Lagrange function is nonzero at one grid point and zero at all other grid points, oscillating between the grid points. Due to the continuous and analytical form these basis functions represent the wave function not only on the grid points but everywhere in space. The Lagrange functions form an orthonormal complete set of states; convergence of the calculated energy is exponential with respect to the grid size. On the Lagrange functions basis, similarly to the finite difference approaches [44, 84, 85], the potential energy matrix is diagonal leading to very sparse Hamiltonians that is ideal for iterative inversion and diagonalization.

The third set uses localized atomic orbitals as basis functions. The main advantage of atomic orbitals is that size of the basis is manageable. The disadvantage is that the atomic orbitals are less flexible in describing continuum states that may play important role in time-dependent perturbation processes. Their inclusion in the present calculations is motivated by their popularity and test purposes.

The Lagrange basis is an ideal basis because it is flexible and the accuracy can be controlled by a single parameter, the number of grid points. For larger systems, however, the number of grid points is several millions or even more which poses computational problems. A large number of orbitals have to be calculated and stored for each grid points. Some of these orbitals are localized around atoms or in finite regions and zero everywhere else so their representation on the whole computational domain is not necessary. In the multidomain approach, basis functions localized in subdomains are generated and used to represent the wave function of the whole system. This substantially reduces the computational cost and ideal for parallel computation. Each subdomain can be solved independently in parallel and the final solution is linear combination of the basis states defined in the subdomains.

7.1 Unitary time evolution

By representing the electron wave function ψ_i in terms of basis functions ϕ_k as

$$\psi_i(\mathbf{r},\mathbf{t}) = \sum_k c_{ik}(t)\phi_k(\mathbf{r}) \tag{7.1}$$

the TKSE takes the form

$$i\frac{\partial c}{\partial t} = S^{-1}Hc \tag{7.2}$$

where S is the overlap matrix between the basis functions, $S_{ij} = \langle\phi_i|\phi_j\rangle$. If Hamiltonian operator commutes with itself at different points in time then the formal solution of Eq. (7.2) is

$$c(t) = U(t,0)c(0) = exp\left(-i\int_0^t S^{-1}H(t')dt'\right)c(0), \tag{7.3}$$

In practice, a discrete form of solution is used. It is obtained by breaking the total evolution operator into evolution operators of small time intervals

$$U(t,0) \simeq \prod_{n=0}^{N-1} U((n+1)\Delta t, n\Delta t), \tag{7.4}$$

where $\Delta t = \frac{T_{tot}}{N}$ and

$$U(t+\Delta t, t) = exp\left(-iS^{-1}H(t)\Delta t\right). \tag{7.5}$$

T_{tot} is the total time that we allow the system to evolve. The discretization with a time step on the order of femtosecond makes calculation insensitive to commutativity of Hamiltonian in time. One difference among propagation schemes arise from the way the exponential in Eq. (7.5) is approximated. In our approach, we approximate the exponential in Eq. (7.5) with the Crank-Nicholson operator. The coefficients between the steps $n+1$ and n are related by the equation

$$c^{n+1} = \frac{1 - iS^{-1}H(t_n)\frac{\Delta t}{2}}{1 + iS^{-1}H(t_n)\frac{\Delta t}{2}}\ c^n. \tag{7.6}$$

This method is unitary, strictly preserving the orthonormality of the states for an arbitrary time evolution. For time independent Hamiltonians it is also explicitly time reversal invariant, and exactly conserves energy. In practice, with a suitable choice of Δt, the energy is satisfactorily conserved even when the Hamiltonian changes with time. One can increase the stability of the solution if we include more terms of the expansion in the numerator and denominator of the Crank-Nicholson operator [86].

By including more terms in the expansion it is possible either to increase the time step preserving the accuracy, or to increase the accuracy of the dynamics and the energy conservation for a given time step. The main advantage of using a bigger time step is the saving of time because we have to calculate the Hamiltonian fewer times. However, one should be careful in extending time step in case of non-commuting in time Hamiltonian. In any case the energy resolution is not affected by the size of time step since it depends on the total time that we allow the system to evolve.

Each box is described by a basis function set ϕ^i_j where i is the box index and j is the index of the basis function in box i. The box basis functions are allowed to overlap with those in the nearest neighboring boxes. The construction of these basis functions will be discussed in the next subsection. The Hamiltonian and overlap matrices in the ith box are defined as

$$(H_{Bi})_{kj} = \langle \phi^i_k | H | \phi^i_j \rangle \qquad (O_{Bi})_{kj} = \langle \phi^i_k | \phi^i_j \rangle \tag{7.7}$$

while those in the connecting neighboring boxes are

$$(H_{Ai})_{kj} = \langle \phi^i_k | H | \phi^{i-1}_j \rangle \qquad (O_{Ai})_{kj} = \langle \phi^i_k | \phi^{i-1}_j \rangle . \tag{7.8}$$

The Hamiltonian of the system will now be a sparse block-tridiagonal structured matrix

$$H = \begin{pmatrix} H_{B1} & H^T_{A2} & 0 & 0 & \dots \\ H_{A2} & H_{B2} & H^T_{A3} & 0 & \dots \\ & & & & H^T_{AN} \\ 0 & \dots & & H_{AN} & H_{BN} \end{pmatrix} \tag{7.9}$$

$$O = \begin{pmatrix} O_{B1} & O^T_{A2} & 0 & 0 & \dots \\ O_{A2} & O_{B2} & O^T_{A3} & 0 & \dots \\ & & & & O^T_{AN} \\ 0 & \dots & & O_{AN} & O_{BN} \end{pmatrix} \tag{7.10}$$

where H_{Bi} (O_{Ai}) and H_{Ai} (O_{Ai}) are $n_i \times n_i$ matrices. Once the block tridiagonal matrices have been generated we perform an LDL decomposition (see Appendix A for details) to have

$$EO - H = LDL^T = \begin{pmatrix} D_1 & L_1^T & 0 & 0 & \dots \\ L_1 & D_2 & L_2^T & 0 & \dots \\ & & & & L_{N-1}^T \\ 0 & \dots & & L_{N-1} & D_N \end{pmatrix} \qquad (7.11)$$

where L_i are a lower diagonal and D are diagonal matrices. Note that the LDL decomposition of a block tridiagonal matrix preserves the block tridiagonal form. The LDL factorization can be generated by a recursive procedure as described in [87] The advantage of the LDL decomposition is that the inverse of the whole matrix can be easily calculated by forward and backward substitutions.

7.3 Basis functions

7.3.1 Box basis functions

The computational cell is divided into N_x intervals

$$[a_i, b_i] \quad (i = 1, \dots, N_x), \qquad (7.12)$$

where $a_{i+1} < b_i$ but $a_i < a_{i+1}$, that is, there is an overlap between the neighboring boxes, but there is no overlap with the second neighbors (Fig. 7.1).

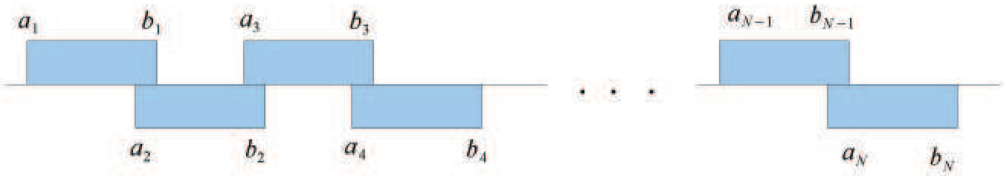

Figure 7.1: Intervals in the x direction.

The jth basis function in the ith box is expanded in terms of a tensorial product of Lagrange basis functions as

$$\phi_j^i(\mathbf{r}) = \textstyle\sum_{l=1}^{M_x} \sum_{m=1}^{M_y} \sum_{n=1}^{M_z} C_{j,lmn}^i L_l^i(x) L_m(y) L_n(z). \qquad (7.13)$$

In the x direction, the Lagrange functions are defined on grid points $a_i < x_k^i < b_i$ as

$$L_n^i(x) = \pi_n(x)\sqrt{w(x)} \qquad \pi_n(x) = \prod_{\substack{k=1\\k\neq n}}^{M_x} \frac{x - x_k^i}{x_n^i - x_k^i} \tag{7.14}$$

where $w(x)$ is the weight function and the index i indicates that the Lagrange function is defined in the ith box. We use the same Lagrange basis $L_m(y)$ and $L_n(z)$ in the y and z directions in each box. Other basis functions e.g. atomic orbitals, Gaussians, or finite differences can be used as well.

There are $M = M_x \times M_y \times M_z$ Lagrange basis functions in each box. The box basis functions ϕ_j^k are generated by solving the eigenvalue problem

$$H_{Ak}C_j^k = E_j O_{Ak} C_j^k \tag{7.15}$$

for C_j^k of eq. (7.13) and keeping the lowest n_k eigenstates (below a preset cutoff energy).

7.3.2 Atomic orbitals

The atomic orbitals are defined as

$$\phi_{k\alpha}^{AO}(\mathbf{r} - \mathbf{R_k}) = \sum_j c_{pj}\varphi_{lm}^{\nu_j}(\mathbf{r} - \mathbf{R_k}) \tag{7.16}$$

where $\mathbf{R}_k$ is the position of atom k and α is an index for (p, l, m). Gaussian functions are used in the expansion of the atomic orbitals

$$\varphi_{lm}^{\nu}(\mathbf{r}) = \left(\frac{4\pi 4^l}{(2l+1)!!}\right)^{1/2} (\sqrt{\nu}r)^l \left(\frac{2\nu}{\pi}\right)^{3/4} \mathrm{e}^{-\nu r^2} Y_{lm}(\hat{r}).$$

The linear combination coefficients c_{pi} are determined by solving the Kohn-Sham equation for a single atom confined in a sphere of radius R_{cutoff} [88, 89, 90, 91], and the AOs vanish beyond that radius. AOs similar to these are very popular in electronic structure and transport calculations. The AO basis depends on the maximum angular momentum l_{max}, the cutoff radius R_{cutoff} and the maximum number p_{max} of radial parts for each value of the the angular momentum l. By increasing l_{max} and p_{max} the accuracy of the calculations improves but the computational time also increases, losing the advantages of the localized basis states. The accuracy of the calculations also depends on the cutoff radius and shape of the AOs. For the molecules used in the present work $R_{cutoff} = 5$ Å and $l_{max} = 2$ give well-converged results [92, 90].

7.4 Calculation of optical absorption spectra

Calculating the optical absorption spectra of molecules, clusters and solids is a practically important applications of TDDFT. Several methods exist, see [7] for a recent summary. We adopt the method by Bertsch *et al.* [93, 94] and apply an impulse electric field $\mathbf{E}(t) = \epsilon\hbar\hat{\mathbf{k}}\delta(t)/e$ to the system at $t = 0$, where $\hat{\mathbf{k}}$ is unit vector and ϵ is a small quantity. The system, which is at its ground state at $t = 0^-$, would undergo transformation

$$\tilde{\psi}_n(\mathbf{x}, t = 0^+) \;=\; e^{i\epsilon\hat{\mathbf{k}}\cdot\mathbf{x}}\tilde{\psi}_n(\mathbf{x}, t = 0^-), \tag{7.17}$$

for all its occupied electronic states, $n = 1..N$, at $t = 0^+$. Note that the true, unpseudized wavefunctions should be used in (7.17) if theoretical rigor is to be maintained.

One may then evolve $\{\tilde{\psi}_n(\mathbf{x}, t), n = 1..N\}$ using a time stepper, with the total charge density $\rho(\mathbf{x}, t)$ updated at every step. Time evolution of polarizability matrix $\hat{\alpha}(t)$ is calculated as

$$\hat{\alpha}(t) \;=\; e\,\hat{\mathbf{k}}\int d^3\mathbf{x}\,\vec{\mathbf{r}}\,\delta\rho(\mathbf{x}, t) \tag{7.18}$$

In a supercell calculation one needs to be careful to leave a large enough spatial region between the molecule centered in the middle and the boundary of computational cell, so no significant charge density can "spill over" PBC boundary, causing a spurious discontinuity in $\alpha(t)$.

The optical absorption cross-section $\sigma(\omega)$ can be computed by extracting imaginary part of Fourier transformed spatially averaged polarizability tensor $\alpha_{avg}(t)$

$$\sigma(\omega) \equiv \frac{2m_e\omega}{e\hbar\pi}\int_0^\infty dt\sin(\omega t)e^{-\gamma t^2}\alpha_{avg}(t), \tag{7.19}$$

where γ is a small damping factor and m_e is the electron mass. In actual implementations a cubic damping function is used. As noted in [7] polynomial rather than exponential dumping factor guarantees the preservation of Thomas-Reiche-Kuhn sum rule. Here we generalize dumping function expression f(t) for arbitrary order. The higher orders N¿3 result in sharpening of spectral peaks analogous to the effect associated with decrease in γ, but this feature should be used with caution as it may introduce artifice.

$$f(t) \; = \; 1 + \sum_{k=2}^{N} \frac{2(-1)^{k+1}}{N-1}(k + (-1)^k)(\frac{t}{T})^k \tag{7.20}$$

The key advantage of the direct time evolution of polarizability matrix under delta-function perturbation is that the entire optical spectrum is obtained from a single run.

7.5 Applications

We have tested the multidomain decomposition approach on four molecules to check the accuracy and applicability of the method. These test calculations are presented in this section. To broaden types of studied molecules in addition to small organic molecules we included a metal cluster and a graphene ribbon. Structures went through geometry optimization using CP2K DFT code [95]; then optical absorption calculations were performed using software developed by our group.

The density and wave functions were saved on disc and then used as a starting point for Finite-Difference (FD) and Multi-Domain Decomposition (fdMDDM). The ground states for Atomic Orbital method (AO) and AO based MDDM (mdMDDM) were treated similarly. We use FD code calculation as a benchmark because its performance is proven to be in excellent agreement with results of others and with experimental data for a range of molecules. As was noted above, using one box in

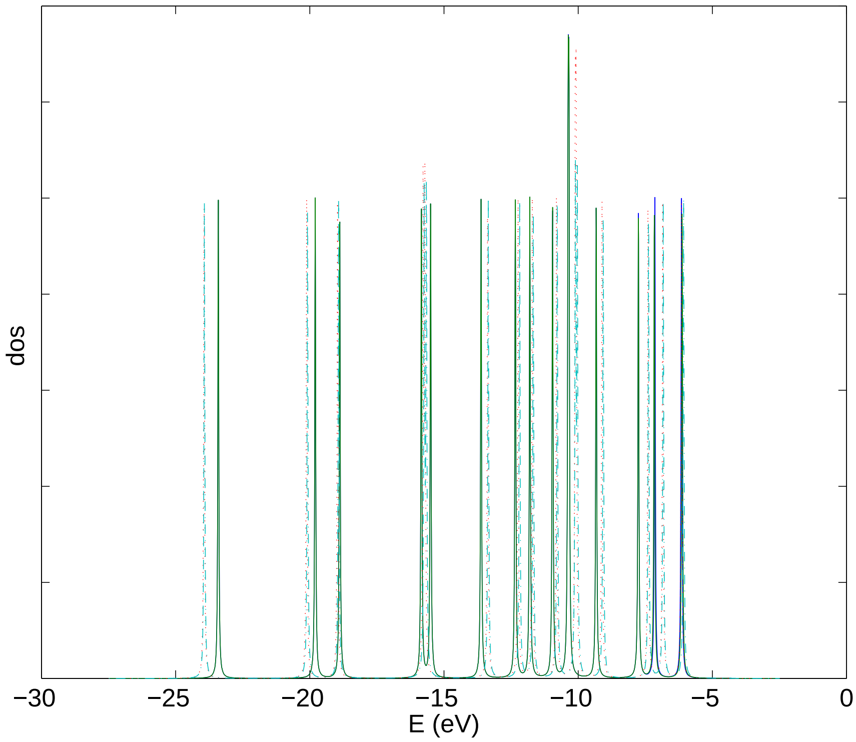

Figure 7.2: Pyridine ground state single particle energies. Dash - Finite Difference, solid - fdMDDM, dot-dash - aoMDDM and dot -Atomic Orbitals.

fdMDDM should in principle lead to the same results as FD.

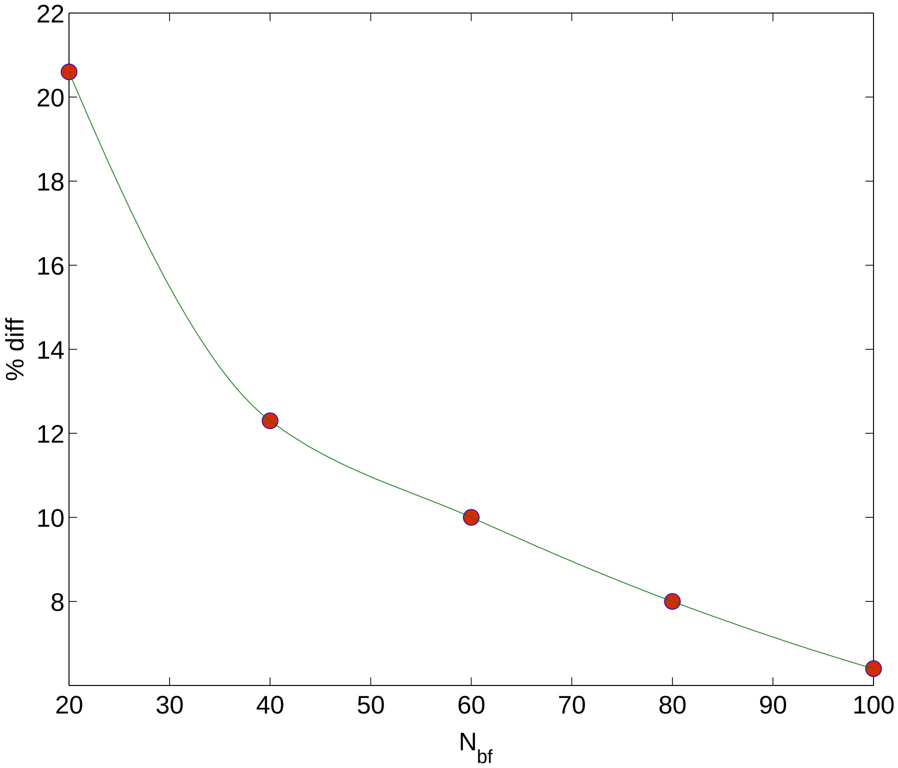

Figure 7.3: Convergence in respect to number of basis functions. N_{bf} - number of fdMDDM basis functions. Y-axis shows percent difference in position of major UV peak between FD and fdMDDM.

Since TDDFT depends parametrically on the initial ground state, for fair comparison between four different methods we needed essentially identical starting conditions. The question was what criteria to use. We decided to use the single particle (s.p.) energy spectra of the ground state as a measure of the difference between MDDM and conventional (FD or AO) initial states (Fig. 7.2). Our intention was to require the tightest possible energy spectra match. It turned out that this was meaningful only for the same kinds of basis representation. In other words, it worked for FD and fdMDDM and for AO and aoMDDM, but the differences up to 0.5Ev didn't play a large role if the basis types differed. Figure 2 illustrates this situation. The s.p. energies form two practically indistinguishable overlaping sets. One set is AO and aoMDDM and another is FD and fdMDDM. There is a difference between the sets, especially notable at lowest energies, but the spectra agreement between AO and FD was in fact better then between FD and fdMDDM (Fig. 7.5). Thus, we have finally adopted the s.p. energy match of ground states as an indication of propensity to converge, but with quantitative measure dependent on what kinds of basis sets are being compared. For different kinds s.p. energies between the methods could deviate up to 0.5eV in some cases, but same kinds of basis have to match up to 0.1eV or better. This ensures that calculated absorption spectra will converge with convergence dependent on the number of box basis functions as shown in case of pyridine (Fig. 7.3).

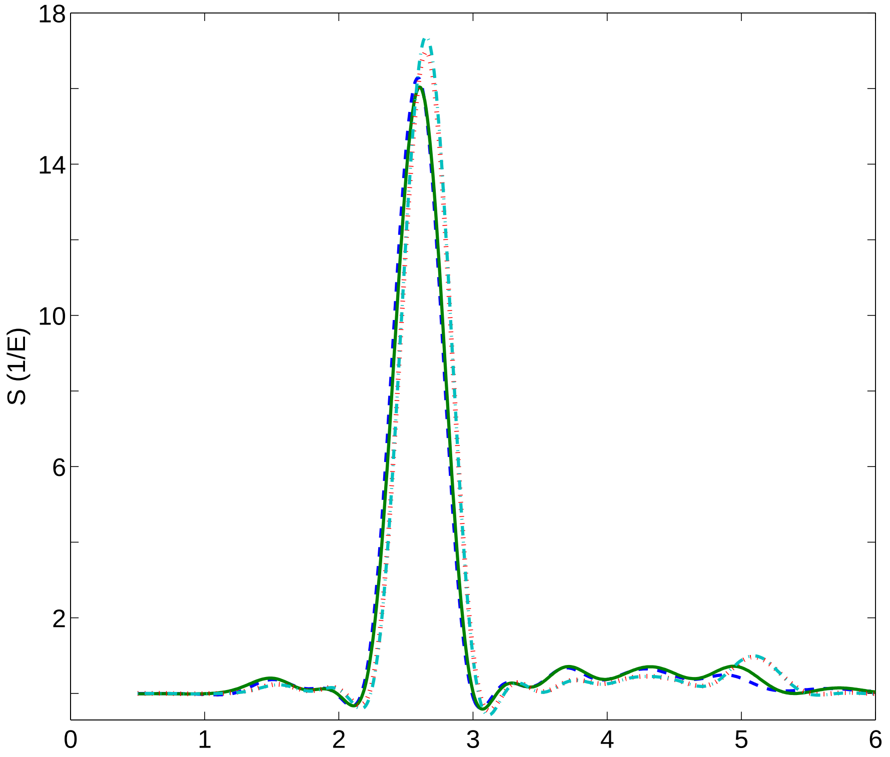

Figure 7.4: Sodium Cluster oscillator strength. Dash - Finite Difference, solid - fdMDDM, dot-dash - aoMDDM and dot -Atomic Orbitals. Eight parameter Gaussian basis set, 125,000 lattice points, 15x15x15 Åcell.

Absorption spectra by all four methods agreed well for eight atom sodium cluster (Fig. 7.3). Large atomic radius required increase in number of basis functions in comparison to other systems and we have used eight parameter Gaussian basis instead of typical six. FD and fdMDDM calculation produced plasmonic peak at 2.6eV and AO at 2.61eV (Fig. 7.4). Experimental data shows plasmonic peak at 2.53eV [96].

The second test case is a pyridine molecule. For the major far-UV peak around 7.2eV MDDM and AO agree to within 0.16eV, while fdMDDM yields 7.6eV (Fig. 7.5). fdMDDM calculations show strong dependence on number of box basis functions (Fig. 7.3).

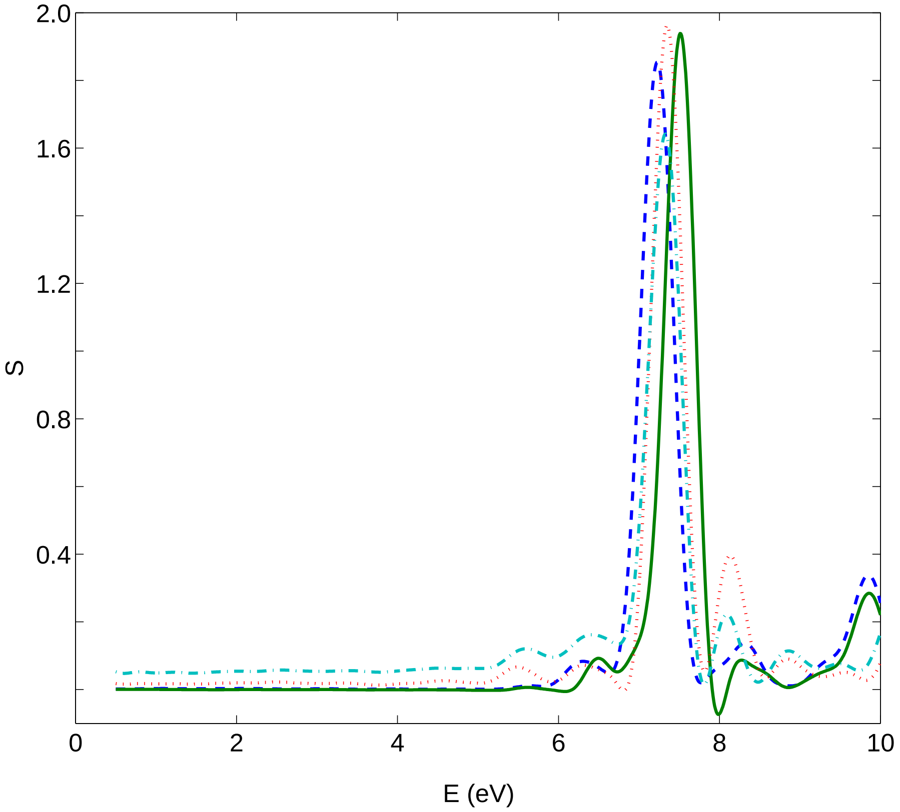

Figure 7.5: Pyridine oscillator strength. Dash - Finite Difference, solid - aoMDDM, dot - fdMDDM and dot-dash -Atomic Orbitals.

Current implementation of the Multi-Domain Decomposition Method is particularly suitable for large elongated supramolecular assemblies. We have chosen two long polymers and a synthetic triad as an illustration. First long molecule is a sixty six atom graphene sheet (Fig. 7.6). The molecule was enclosed in 33x12x12 Å cell and contained 192 electrons. The Multi-Domain Decomposition employed 220 basis functions ranging 1.1-1.6 b.f. per electron depending on the region of molecule. Both FD and MDDM had shown good agreement in spectral region up to the fist ionization energy $\sim$ 5.3 eV (Fig. 7.7).

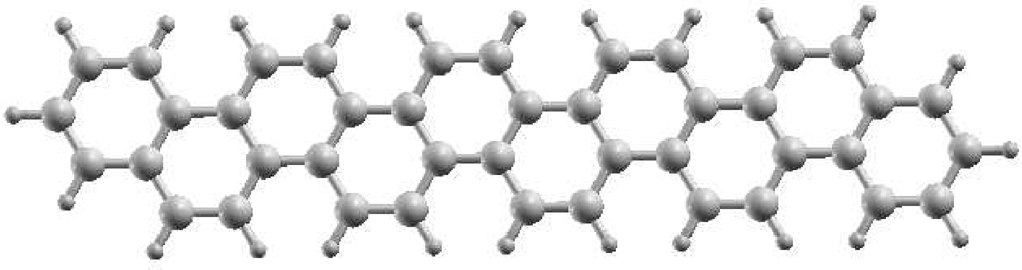

Figure 7.6: Graphene ribbon structure.

In the UV-Vis part of spectra first peaks agree to 0.1eV and second and third are within 0.15eV. We have to note that in our calculations the spectra become divergent at energies above 6.0eV as the first quartet of electrons become delocalized and perhaps encountered boundaries of the computational cell. Interestingly, when the perturbing field was directed along the axis of the ribbon, the polarization dynamics in both FD and MDDM calculations matched up to 10eV, and it is only the perpendicular direction that had shown significant difference between these two methods.

The second long molecule is a 26 atom alkene chain (Fig. 7.8). Here again all methods agreed within the practically important IR-Vis-UV region 1-5eV.

The last example is a light harvesting triad (Fig. 7.9). The design of the molecule was inspired by [97]. Our version of triad differs form the previously published by a)replacement of beta-carotene with graphene strip, b) inclusion of iron in porphyrin ring and c) shorter, simpler linker between C_{60} and porphyrin. These changes were motivated by further enhancement of charge transfer and optical absorption in visible part of spectra with the aim of potential use of the device as a power generator for prospective nanomachinery [98]. Although there is yet no experimental data for this type of design we expected that dominant absorption peak in UV-Vis region will

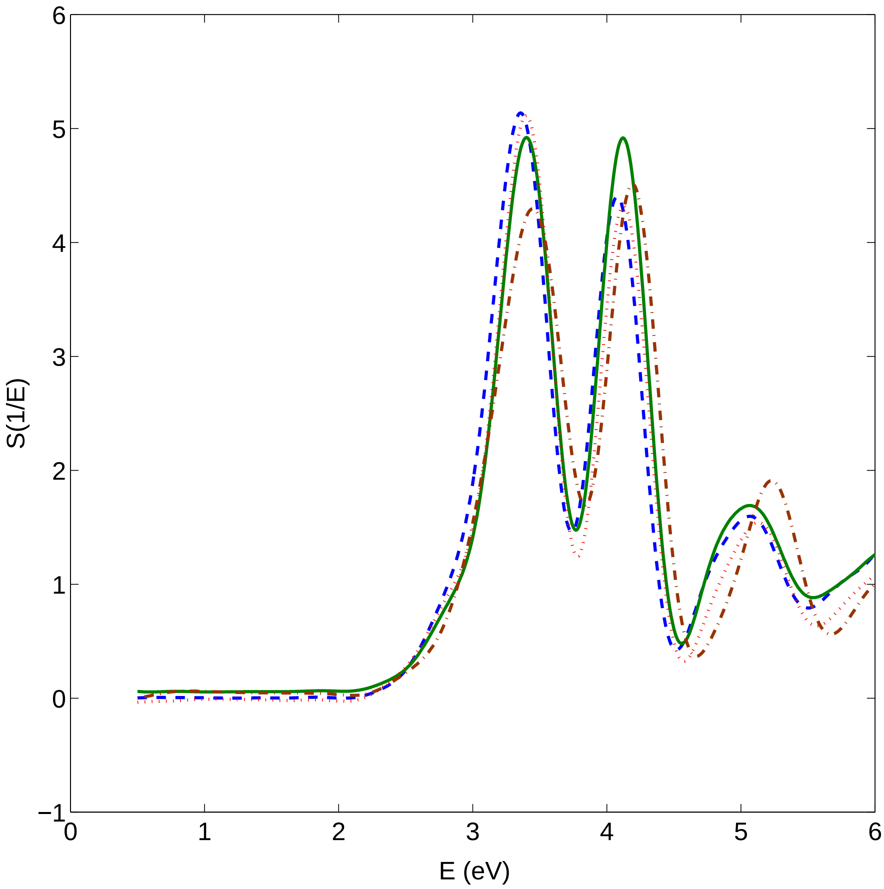

Figure 7.7: Graphene ribbon oscillator strength. Dash - Finite Difference, solid - fdMDDM, dot-dash - aoMDDM and dot -Atomic Orbitals.

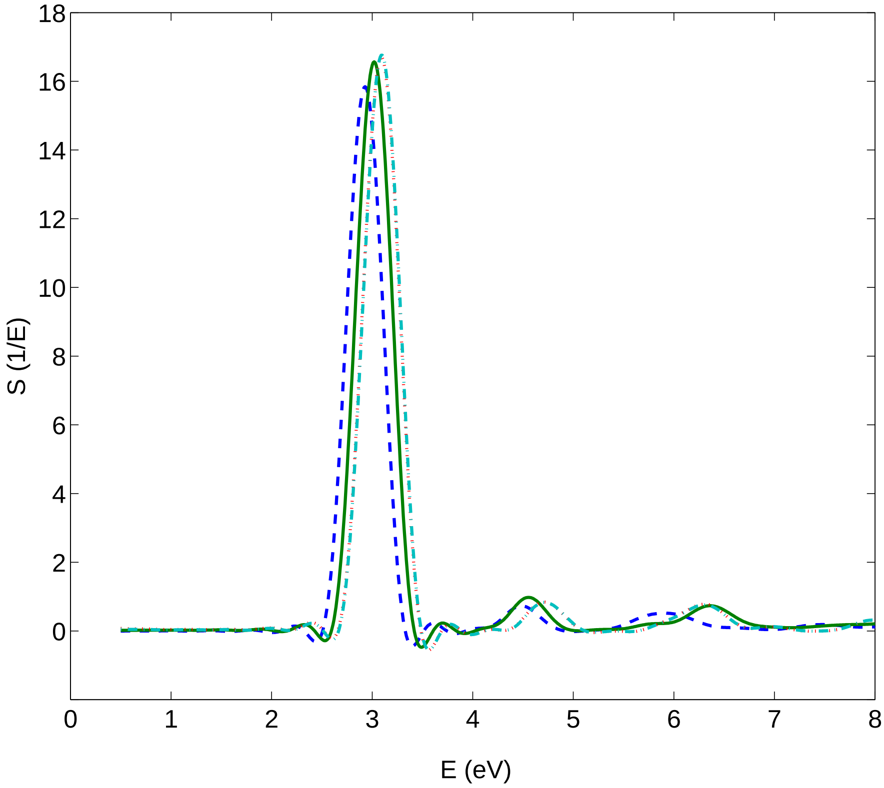

Figure 7.8: Alkene chain oscillator strength. AO and aoMDDM make a near perfect overlay making them indistinguishable on this graph. Dash - Finite Difference, solid - fdMDDM, dot-dash - aoMDDM and dot -Atomic Orbitals.

come from the porphyrin photocenter,and that was confirmed. Indeed, 3.0 eV peak coincides with experimentally observed porphyrin peak in [97].

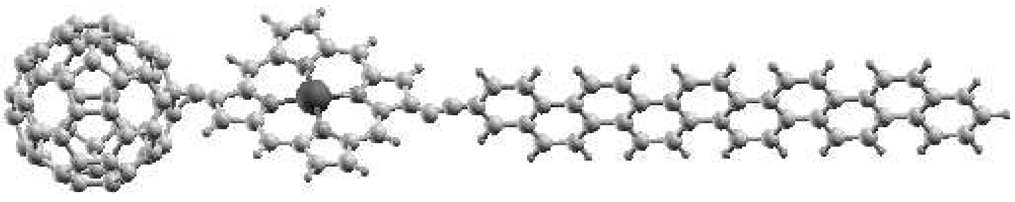

Figure 7.9: Triad Structure.

The triad consisted of 163 atoms, was placed in 54x18x18 Åcell and contained 561 electrons. The size of the cell was similar to the recent RT-TDDFT study of the carotene-porphyrin-fullerene (C-P-C60) triad [99], but our choice of the linker has straightened the molecule and allowed to reduce the cell in one of the dimensions. The absorption spectra of graphene-porphyrin-C_{60} (G-P-C60) triad shows remarkable enhancement of absorption in visible and near-UV spectrum. The wide 2-3 eV gap noted in [99] has been filled. In fact G-P-C60 shows enhanced absorption within 0.8-3.5 eV range with transient peaks at 1.9 and 2.7 eV making it excellent natural light trap. We also expect that use of graphene rather then beta-carotene tail will enhance electron transmission during recombination step leading to overall improvement in the device efficiency.

7.6 Summary

In conclusion we may note that a number of TDDFT based software packages for calculation of optical properties were developed, with an explosive growth in recent years. These packages could be broadly split in three categories. The first is the class of frequency domain calculators, such as ABINIT (www.abinit.org), dp and EXC (www.etsf.eu). The root of the method they are based on, is in the solution of Bethe-Salpeter equation. This method is considered standard for semiconductors and some other solids calculations. The second class features Cassida approach [100]. It is also implemented in ABINIT, as well as in GAMESS (www.msg.chem.iastate.edu), Gaussian (www.gaussian.com) and other packages. This method is the most popular

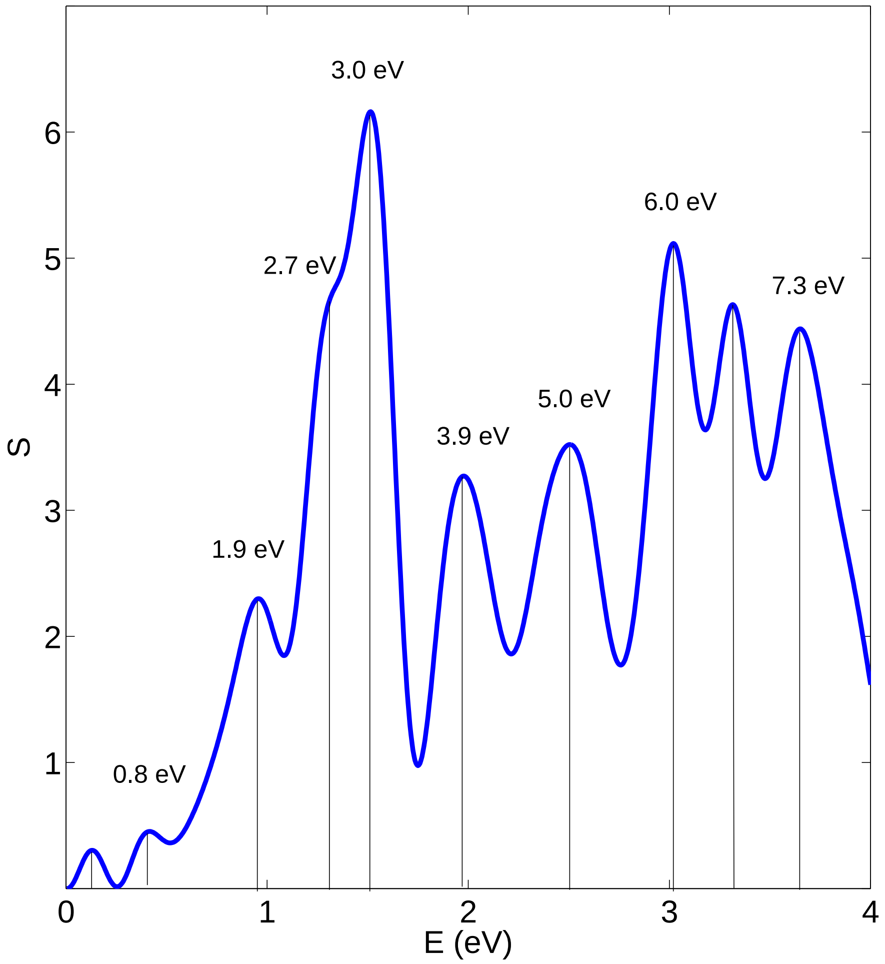

Figure 7.10: Light harvesting TRIAD, oscillator strength. Data is for aoMDDM as calculation times for FD and AO become prohibitively long.

Table 7.1: Multidomain Decomposition calculations require significantly lower number of basis functions for the same accuracy. N_{atom} - number of atoms, N_{box} - number of domains, $N_{b.f.}$ - number of basis functions or grid points in case of FD. Cell dimensions are in Å.

molecule	N_{atom}	cell	method	N_{box}	$N_{b.f.}$
Pyridine	11	14x14x14	FD		103823
			fdMDDM	1	100
			AO		242
			aoMDDM	1	100
Alkene	26	27x15x15	FD		225000
			dMDDM	3	180
			AO		364
			aoMDDM	3	180
Graphene	66	33x12x12	FD		176000
			fdMDDM	5	220
			AO		528
			aoMDDM	5	220

with physical chemists and chemical physicists. The third class is dynamic real-time TDDFT as discussed in this paper. The OCTOPUS (www.tddft.org) is the most well known example of this class.

Overall our implementation of MDDM had shown reasonable accuracy and efficiency in calculation of optical absorption spectra. Out of two MDDM implementations, aoMDDM shows better convergence then fdMDDM for the tested cases. The majority of test cases chosen were relatively small; we expect MDDM to outperform conventional AO and FD for larger molecules, and to show its superiority when code parrallelization effort is complete. We may conclude that Multi-Domain Decomposition Method passes initial evaluation and shows a promise as an efficient method for calculating physical properties of large linear molecules. We plan to continue developing MDDM to extend its capabilities over globular supramolecular assemblies and nanostructures.

Chapter 8

CONCLUSION

In this thesis, I have advanced methodology for calculating nonlinear optical response functions. The methodology is not perturbative and is based on dynamic simulation of interaction of the electro-magnetic field and matter from first principles. The interaction is modeled by solving time-dependent Schrödinger equation in case of finite systems and by a coupled system of Maxwell and time-dependent Schrödinger equations in case of solids. The Hamiltonian is taken at the level of TDDFT, and is typically uses ALDA exchange-correlation functional to represent the electron-electron interactions and pseudopotentials to represent the interaction of valence electrons with the effective potential of nuclei and filled electron shells.

The frequency dependent polarization response is calculated from single particle orbitals in case of finite systems and from the polarization current in case of solids. The m order response functions are extracted from corresponding m order polarizations that depend on m power of electric field E^m. The higher order polarizations could be obtained from total polarization by one of many decomposition algorithms, three of which are described in detail in this thesis.

The extraction step depends on locality of the polarization response in frequency space. I have shown that by using quasi monochromatic excitation the optical response could be localized in practice.

I have explored nonlinear response in small organic molecules and found that under non-resonance conditions the quasi monochromatic response is indistinguishable from monochromatic. In this case the nonlinear response becomes fully local and the total polarization decomposes into a finite polynomial in the electric fields. When this condition holds, nonlinear response resembles linear response in the sense that the m order polarization is equal to m power of electric field multiplied by a complex constant.

The real-time calculations of nonlinear response have about the same accuracy as the most accurate perturbative methods [1]. At the same time real-time approach yields more information then perturbative methods, because it samples material response within approximately 1 eV energy range yielding qualitative features of the response near excitation frequency. This information is helpful both in increasing reliability and in characterizing the photon-matter interaction. When compared with experiment, the real-time method typically deviates from empirical data within 15-75 %. The major source of error is in inadequacy of currently available exchange-correlation functionals.

Among the multitude of directions for future development I would like to point out the following.

- Including local field effects by giving vector potential spatial dependence.
- Upgrading the equation for vector potential in (6.24) to the wave equation.
- Including nuclear dynamics.
- Exploring the current dependent exchange-correlation functionals.
- Using adaptive grids for real-space calculations.

To conclude, the real-time method for calculating nonlinear response is a viable alternative to the modern perturbative methods, and is likely to become the method of choice when its capabilities in realistic simulations of dynamics of the electron-photon interaction become more widely known.

---

[1] Such as modified Sternheimer method.

Appendix A

APPENDIX TO CHAPTER 1

A.1 N-electron system

A variety of important physical properties[1] of molecular systems could be straightforwardly calculated if the solution of N - electron Schrödinger Equation (A.1) is known.

$$\hat{H}|\Psi_n\rangle = E_n|\Psi_n\rangle \tag{A.1}$$

Disregarding relativistic corrections and magnetic effects the relevant Hamiltonian could be written as following:

$$\hat{H} = \hat{T}_e + \hat{T}_n + \hat{W}_{ee} + \hat{W}_{nn} + \hat{W}_{en}. \tag{A.2}$$

First two terms in (A.2) are one-body kinetic energy operators for N_e-electrons and N_n-nuclei. The remaining are two-body potential energy operators representing Coulombic interactions between electrons and nuclei. The electronic and nuclear dynamics happen on different time scales. In many cases this allow to search for solution of electron dynamics while nuclear degrees of freedom are kept constant. This approach is known as Born-Oppenheimer (BO) approximation. The (BO) Hamiltonian is substantially simpler, because the nuclear kinetic operator $\hat{T}_{nn}$ vanishes, the nuclear potential energy becomes constant $\hat{W}_{nn} \rightarrow$ *const.*, and electron-nuclear potential energy operator becomes one-body operator. The (BO) Hamiltonian is

$$\hat{H} = \sum_{i=1}^{N_e} \frac{p_i^2}{2\,m_e} + \sum_{i<j}^{N_e} \frac{e^2}{|\vec{r}_i - \vec{r}_j|} - \sum_{i=1}^{N_n}\sum_{j=1}^{N_e} \frac{e^2}{2}\frac{Z_i}{|\vec{R}_i - \vec{r}_j|} \tag{A.3}$$

---

[1] Chemical structure, mechanical properties such as elasticity tensor, electronic spectra including optical and X-ray, dielectric constant, etc.

Where $\hat{p}_j$ is a momentum operator acting on coordinates of j -electron: $\hat{p}_j = -\imath\hbar\nabla_j$. The eigenstates and eigenenergies of (A.1) become parametrically dependent on a set of nuclear coordinates: $|\Psi_n\rangle = |\Psi_n(\{\vec{R}_i\})\rangle$, $E_n = E_n(\{\vec{R}_i\})$, although this dependence is typically kept implicit. One may write spatial and spin degrees of freedom of i^{th} electron as as set $(\vec{r}_i, s_i) \rightarrow (x_i)$. N-electron wavefunction in coordinate representation is

$$\langle x_1\, x_2\, \ldots x_N|\Psi\rangle = \Psi(x_1, x_2, \ldots, x_N) = \Psi(\{x_i\}). \tag{A.4}$$

It can be written as a sum over orbital configurations $L = (l_1, l_2, \ldots, l_n)$:

$$\Psi_n(\{x_i\}) = \sum_L C_L \Phi_L(\{x_i\}), \tag{A.5}$$

where

$$\Phi_L(\{x_i\}) = \frac{1}{\sqrt{N!}} \det \|\phi_{l_i}(x_k)\| \tag{A.6}$$

is a determinant composed of two component spinor orbitals

$$\phi_l(x) = \begin{pmatrix} \phi_\uparrow(\vec{r}) \\ \phi_\downarrow(\vec{r}) \end{pmatrix}$$

.

Representation of N-electron wavefunction (A.5) is known as full Configuration Interaction (CI). CI solutions for (A.1) are generally intractable. Therefore (A.5) is truncated at first few determinants to produce an approximation.

A.2 Hartree-Fock

Hamiltonian (A.3) conserves total spin. Therefore it is expected that $|\Psi\rangle$ is an eigenfunction of square of total spin operator $\hat{S}^2$:

$$\hat{S}^2|\Psi\rangle = s(s+1)|\Psi\rangle \tag{A.7}$$

However, using one determinant in (A.5) generally do not satisfy (A.7), except when total spin is zero. It may be shown that N-electron wavefunction with definite

Table A.1: Few electron wavefunction with definite spin. Ψ is wavefunction constructed according to (A.8). N - is number of electrons, S-total spin, K-is number of paired electrons. Normalization factor $\frac{1}{\sqrt{N!}}$ is omitted.

N	S	K	$\Psi = \Psi^{(1)}\,\Psi^{(2)}$
1	$\frac{1}{2}$	0	$\phi_1(r)$
2	0	1	$\phi_1(r_1)\phi_1(r_2)$
2	1	0	$\phi_1(r_1)\phi_2(r_2) - \phi_2(r_1)\phi_1(r_2)$
3	$\frac{1}{2}$	1	$\phi_1(r_1)(\phi_1(r_2)\phi_2(r_3) - \phi_2(r_2)\phi_1(r_3))$
3	$\frac{3}{2}$	0	$\phi_1(r_1)(\phi_2(r_2)\phi_3(r_3) - \phi_3(r_2)\phi_3(r_3))-$
			$-\phi_1(r_2)(\phi_2(r_1)\phi_3(r_3) - \phi_3(r_1)\phi_2(r_3)) + \phi_1(r_3)(\phi_2(r_1)\phi_3(r_2) - \phi_3(r_1)\phi_2(r_2))$

total spin s can be constructed from $N-k$ orbitals $\phi_i(\vec{r})$ arranged as product of two determinants (Fock, 1930)[101]:

$$\Psi = \Psi^{(1)}\,\Psi^{(2)}, \tag{A.8}$$

where

$$\Psi^{(1)} = \begin{vmatrix} \phi_1(\vec{r}_1)\ldots\phi_1(\vec{r}_k) \\ \ldots\ldots\ldots \\ \phi_k(\vec{r}_1)\ldots\phi_k(\vec{r}_k) \end{vmatrix} \tag{A.9}$$

$$\Psi^{(2)} = \begin{vmatrix} \phi_1(\vec{r}_{k+1})\ldots\phi_1(\vec{r}_N) \\ \ldots\ldots\ldots \\ \phi_k(\vec{r}_1)\ldots\phi_k(\vec{r}_k) \end{vmatrix} \tag{A.10}$$

$$k = \frac{N}{2} - s. \tag{A.11}$$

One may note that orbitals entering (A.8) are spinless. Table A.1 shows an example of Ψ constructed according to (A.8).

Evaluating total energy $E[\Psi]$

$$E[\Psi] = \frac{\langle\Psi|\hat{H}|\Psi|\rangle}{\langle\Psi|\Psi\rangle}, \quad \langle\Psi|\Psi\rangle = N, \tag{A.12}$$

with Ψ from(A.8) and rewriting relevant terms using expression for single electron Hamiltonian H_0

$$H_0(\vec{r}) = \frac{p^2}{2m_e} + 2e^2 \int \frac{\rho(\vec{r}', \vec{r}')}{|\vec{r} - \vec{r}'|} d^3r' \tag{A.13}$$

gives:

$$\begin{aligned} E[\Psi] = \sum_{p=1}^{k} \int \phi^*(\vec{r}) H_0(\vec{r}) \phi^*(\vec{r}) d^3r + \sum_{p=1}^{N-k} \int \phi^*(\vec{r}) H_0(\vec{r}) \phi^*(\vec{r}) d^3r + \\ + \frac{e^2}{2} \int \frac{\rho^{(1)}(\vec{r}, \vec{r}) \rho^{(1)}(\vec{r}', \vec{r}') - |\rho^{(1)}(\vec{r}, \vec{r}')|^2}{|\vec{r} - \vec{r}'|} d^3r\, d^3r' + \\ + \frac{e^2}{2} \int \frac{\rho^{(2)}(\vec{r}, \vec{r}) \rho^{(2)}(\vec{r}', \vec{r}') - |\rho^{(2)}(\vec{r}, \vec{r}')|^2}{|\vec{r} - \vec{r}'|} d^3r\, d^3r' + \\ + \frac{e^2}{2} \int \frac{\rho^{(1)}(\vec{r}, \vec{r}) \rho^{(2)}(\vec{r}', \vec{r}')}{|\vec{r} - \vec{r}'|} d^3r\, d^3r' \end{aligned} \tag{A.14}$$

Where $\rho^{(1)}$ and $\rho^{(2)}$ are single particle density matrices:

$$\rho^{(1)}(\vec{r}, \vec{r}') = \sum_{i=1}^{k} \phi_i(\vec{r})^* \phi_i(\vec{r}'), \tag{A.15}$$

$$\rho^{(2)}(\vec{r}, \vec{r}') = \sum_{i=1}^{N-k} \phi_i(\vec{r})^* \phi_i(\vec{r}'). \tag{A.16}$$

The energy obtained from (A.14) accounts for 99% of total electronic energy for molecules and atoms. Its non-trivial structure is a manifistation of electron correlation due to spin exchange. From (A.14) follows a system of equation from which $\phi_q(\vec{r})$ are determined. In case of closed shell (total spin zero) these equations reduce to Hartree-Fock equation (A.17):

$$\left(\frac{p^2}{2m_e} + 2e^2 \int \frac{\rho(\vec{r}', \vec{r}')}{|\vec{r} - \vec{r}'|} d^3r' \right) \phi_q(\vec{r}) - e^2 \int \frac{\rho(\vec{r}, \vec{r}') \phi_q(\vec{r}')}{|\vec{r} - \vec{r}'|} d^3r' = E_q \phi_q(\vec{r}) \tag{A.17}$$

The Mean Field Coulomb potential in (A.17) is known as Hartree potential[102]:

$$V_H(\vec{r}) = 2e^2 \int \frac{\rho(\vec{r'}, \vec{r'})}{|\vec{r} - \vec{r'}|} d^3 r'. \tag{A.18}$$

Hartree potential ls a local potential and depends on total electron density. It could be represented by a one-body operator.

The non-local integral operator is known as Quantum Exchange [101] (a.k.a. Fock exchange):

$$\hat{K}\phi_q(\vec{r}) = -e^2 \int \frac{\rho(\vec{r}, \vec{r'})\phi_q(\vec{r'})}{|\vec{r} - \vec{r'}|} d^3 r'. \tag{A.19}$$

The Exchange operator is a two-body operator and is computationally demanding. Omitting it leads to Hartree equation, which in atomic units appears as:

$$\left(-\frac{\nabla^2}{2} + V_H(\vec{r}) \right) \phi(\vec{r}) = E\phi(\vec{r}). \tag{A.20}$$

A local approximation to the Exchange operator is known $\hat{K} \to \hat{V}_{x\alpha}$[103, 104]:

$$V_{x\alpha}(\vec{r}) = -2\alpha C_x \rho(\vec{r})^{\frac{1}{3}}, \tag{A.21}$$

where C_x and α are constants and $\rho(\vec{r})$ is total electronic density. Combining Hartree and $V_{x\alpha}$ into effective potential $V_{eff}(\vec{r}) = V_H(\vec{r}) + V_{x\alpha}(\vec{r})$ allows one to approximate (A.17) by the following equations:

$$\left(-\frac{\nabla^2}{2} + V_{eff}(\vec{r}) \right) \phi(\vec{r}) = E\phi(\vec{r}). \tag{A.22}$$

A.3 Local Spin Density Approximation

Energy functional (A.14) was obtained as a product of two determinants approximation to (A.5), and does not account for all electron-electron interactions. In particular, it does not account for the correlations beyond spin exchange. Density Functional Theory (DFT) furnishes a number of approximations to these correlations, including a Local Spin Density Approximation (LSDA). LSDA approximates correlations with a local potential known as correlation potential: $V_c(\vec{r})$. Within LSDA, $V_{x\alpha}$ is cast into a slightly different form: $V_x = -\frac{4}{3}C_x\rho(\vec{r})^{\frac{1}{3}}$. The effective potential becomes:

$$V_{eff}(\vec{r},s) = V_H(\vec{r}) + V_x(\vec{r}) + V_c(\vec{r},s) = V_x(\vec{r}) + V_{xc}(\vec{r},s). \tag{A.23}$$

Note that (A.23) is in general spin dependent. Solving (A.22) with (A.23) allows to find a set of single particle orbitals $\{\phi_k(x)\}$ known as Kohn-Sham orbitals. These are put in a single determinant form (A.6) to provide an approximation to the ground state of the N-electron system. Kohn-Sham orbitals are found by Self Consistent Field (SCF) iterative procedure. Applicability of DFT is limited to the ground state; excited states are explored by extension of DFT known as Time Dependent Density Functional Theory (TDDFT). Within DFT equation (A.22) is called Kohn-Sham equation[105]. It is deceptively similar to Schrödinger Equation, yet this is a non linear equation, and it can only be solved by an iterative self consistent procedure where it regains linearity at each iteration step.

A.4 Conjugate Gradients for linear equations

The minimum $\vec{x}_*$ of a positively defined quadratic form

$$F(\vec{x}) = c - \vec{b} \cdot \vec{x} + \frac{1}{2}\vec{x}^T A\,\vec{x} \tag{A.24}$$

is attained at a point where its gradient

$$\nabla F = -\vec{b} + A\,\vec{x} \tag{A.25}$$

is zero:

$$A\,\vec{x} = \vec{b} \tag{A.26}$$

Thus, the problem of finding a minimum of a positively-defined quadratic form is equivalent to a solution of (generally non-homogeneous) linear system. One efficient algorithm for the solution of this problem is a Conjugate Gradient (CG) iteration. Similarly to steepest descent method, it approaches the solution in a series of steps [106]:

$$\vec{x}_n = \vec{x}_{n-1} + \alpha_n \vec{p}_{n-1} \tag{A.27}$$

The directions of the search $\vec{p}_n$ are "A-conjugate":

$$\vec{p}_n^T A\,\vec{p}_j = 0 \ \ (j < n) \tag{A.28}$$

and the residuals

$$\vec{r}_n = \vec{b} - A\,\vec{x}_n \tag{A.29}$$

are orthogonal:

$$\vec{r}_n \cdot \vec{r}_j = 0 \ \ (j < n). \tag{A.30}$$

The residual of the linear problem $\vec{r}_i$ serves as a "gradient" $\vec{g}_i$ to the quadratic problem. The error at each step is

$$\vec{e} = \vec{x}_* - \vec{x}_n \tag{A.31}$$

Since A - is positive definite, we can define norm on R^n

$$||\vec{x}||_A = \sqrt{\vec{x}^T A\, \vec{x}}. \tag{A.32}$$

With exact arithmetic, CG minimizes $||\vec{e}||_A$ (and $||\vec{e}||_A^2$) in $m < n$ steps [106]. CG iteration algorithm reads: $\vec{x}_0 = 0$, $\vec{r}_0 = \vec{b}$, $\vec{p}_0 = \vec{r}_0$

for n =1,2,3, ...

$$\alpha_n = \frac{\vec{r}_{n-1}^T \vec{r}_{n-1}}{\vec{p}_{n-1}^T A\, \vec{p}_{n-1}} \quad (step\ \ length) \tag{A.33}$$

$$\vec{x}_n = \vec{x}_{n-1} + \alpha_n \vec{p}_{n-1} \quad (approximate\ \ solution) \tag{A.34}$$

$$\vec{r}_n = \vec{r}_{n-1} - \alpha_n A\, \vec{p}_{n-1} \quad (residual) \tag{A.35}$$

$$\beta_n = \frac{\vec{r}_n^T \vec{r}_n}{\vec{r}_{n-1}^T \vec{r}_{n-1}} \quad (improvement) \tag{A.36}$$

$$\vec{p}_n = \vec{r}_n + \beta_n \vec{p}_{n-1} \quad (search\ \ direction) \tag{A.37}$$

This algorithm could be used to solve linearized Poisson equation.

A.5 Conjugate Gradients for total energy minimization

The Conjugate Gradients algorithm in its original form (appendix A.4) has to be modified if the minimization is constrained. In case of total energy minimization, the relevant constraint is orthonormality of the wave eigenfunctions. In this case the symmetric, positively-defined quadratic form of interest is

$$F(\{|\psi_i\rangle\}) = 2\sum_i^{occ.} \langle\psi_i|H - \lambda_i|\psi_i\rangle. \tag{A.38}$$

Role of $\vec{x}_k$ is taken by $\{|\psi_{i,k}\rangle\}$. The eigenfunctions and eigenvalues may have two indices. Index i indicates the orbital (eigenstate) and the second index - k indicates the iteration. Absence of iteration index for these quantities in the particular expression means that they do not vary in the particular expression. On another hand, the quantities that are "internal" to the algorithm, such as $\vec{r}_i$ etc., need to have only one index - iteration. In order to satisfy the orthogonality constraints $\langle\psi_i|\psi_j\rangle = \delta_{ij}$, we remove the projection of the gradient on the previously optimized orbitals. The expression for the "gradient" of the quadratic form (or equivalently the residual) becomes:

$$\vec{r}_{n+1} = 2(H - \lambda_{p,n})|\psi_{p,n}\rangle - \sum_{q=1}^{p-1} \langle \psi_q | 2(H - \lambda_{p,n}) | \psi_{p,n} \rangle |\psi_q\rangle \tag{A.39}$$

where

$$\lambda_{p,k} = \frac{\langle \psi_{p,k} | H | \psi_{p,k} \rangle}{\langle \psi_{p,k} | \psi_{p,k} \rangle}. \tag{A.40}$$

The sum in (A.39) keeps gradient $(H - \lambda_{p,n})|\psi_{p,n}\rangle$ orthogonal to all $(p-1)$ previously optimized eigenfunctions during the search. The step length α_n may be chosen from condition yielding extremum of the energy functional along the one-dimensional search line and is given below (A.41). The modified algorithm reads:

For each orbital p: initialize $\vec{p}_0 = 0, \;\; \lambda_{p,0} = \frac{\langle \psi_{p,0} | H | \psi_{p,0} \rangle}{\langle \psi_{p,0} | \psi_{p,0} \rangle}, \;\; \vec{r}_0^T \vec{r}_0 = 10^{50}$.

For n=1,2,3,...

- compute gradient $\vec{r}_n$ using (A.39)
- improvement $\beta_n = \frac{\vec{r}_n^T \vec{r}_n}{\vec{r}_{n-1}^T \vec{r}_{n-1}}$
- search direction $\vec{p}_n = -\vec{r}_n + \beta_n \vec{p}_{n-1}$
- compute $H\vec{p}_n$
- solve (A.41) and take the larger root as α_n
- $|\psi_{p,n}\rangle = |\psi_{p,n-1}\rangle + \alpha_n \vec{p}_n$
- advance $H|\psi_{p,n}\rangle = H|\psi_{p,n-1}\rangle + \alpha_n \, H\vec{p}_n$, and compute $\lambda_{p,n}$.

The ultimate objective function is the energy functional, and the step α_n may be taken as a solution of

$$\frac{\partial}{\partial \alpha_n} \frac{\langle \psi_{p,n-1} + \alpha_n \vec{p}_n | H | \psi_{p,n} + \alpha_n \vec{p}_n \rangle}{\langle \psi_{p,n-1} + \alpha_n \vec{p}_n | \psi_{p,n-1} + \alpha_n \vec{p}_n \rangle} = 0. \tag{A.41}$$

After rearrangement this yields a quadratic equation

$$\alpha_n(\langle\vec{p}_n|H|\vec{p}_n\rangle\langle\psi_{p,n-1}|\vec{p}_n\rangle - \langle\psi_{p,n-1}|H|\vec{p}_n\rangle\langle\vec{p}_n|\vec{p}_n\rangle) + \alpha_n(\langle\vec{p}_n|H|\vec{p}_n\rangle\langle\psi_{p,n-1}|\psi_{p,n-1}\rangle - \langle\psi_{p,n-1}|H \\ |\psi_{p,n-1}\rangle\langle\vec{p}_n|\vec{p}_n\rangle) + \langle\psi_{p,n-1}|H|\psi_{p,n-1}\rangle\langle\psi_{p,n-1}|\psi_{p,n-1}\rangle - \langle\psi_{p,n-1}|H|\psi_{p,n-1}\rangle\langle\psi_{p,n-1}|\vec{p}_n\rangle = 0, \tag{A.42}$$

the larger root is α_n.

Appendix B

APPENDIX TO CHAPTER 2

B.1 Causal Response

Response functions form a wide class of both classical and quantum quantities. Synonyms of response functions are linear and non-linear susceptibilities of different kinds, as well as polarizability and hyperpolarizabilities. The defining characteristic of a response function $\chi(t)$ is causality of a map that it establishes between perturbing quantity $E(t)$ and a responding quantity $P(t)$[1]. In case of a linear response function, it is accomplished by an integral relation:

$$P(t) = \int_0^\infty \chi^{(1)}(\tau)E(t-\tau)d\tau. \tag{B.1}$$

One may examine by inspection that (B.1) guarantees that values of $E(t)$ at times earlier than t_0 do not contribute to $P(t_0)$. It also allows for response $P(t_0)$ to persist for all times $t > t_0$ even if field $E(t)$ is zero at these times. For example, taking time profile as delta function for $E(t) = E\,\delta(t)$, and taking $\chi^{(1)}$ as being non-zero only on an interval $0 < t < t_M$ leads to the following Response $P(t)$:

$$P(t) = \begin{cases} E\chi^{(1)}(t) & \text{if } 0 < t < t_M \\ 0 & \text{if } t > t_M \end{cases} \tag{B.2}$$

Multiplying (B.1) by $e^{i\omega t}$, integrating in time t from $-\infty$ to ∞, changing variable in left hand side (LHS) $t' = t - \tau$ and using definition of Fourier Transforms one gets frequency domain representation of linear response:

$$P(\omega) = \chi^{(1)}(\omega)E(\omega), \tag{B.3}$$

---

[1] Both $P(t)$ and $E(t)$ are assumed to be observable (i.e. real)

where linear response function is:

$$\chi^{(1)}(\omega) = \int_0^{\infty} \chi^{(1)}(t) e^{i\omega t} dt. \tag{B.4}$$

Sometimes it is convenient to replace (B.4) by a conventional Fourier Transform by multiplying $\chi^{(1)}(t)$ by step function $\theta(t)$ and extending limits of integration to $-\infty$. Generalizations of (B.1) and (B.3) to higher order response are:

$$P^{(n)}(t) = \int_0^{\infty} \dots \int_0^{\infty} \chi^{(n)}(\tau_1, \dots, \tau_n) E(t-\tau_1) \dots E(t-\tau_n) d\tau_1 \dots d\tau_n, \tag{B.5}$$

$$\begin{aligned} P^{(n)}(\omega) = \frac{1}{(2\pi)^{(n-1)}} \int_0^{\infty} \dots \int_0^{\infty} \chi^{(n)}(\omega; \omega_1, \dots, \omega_n) E(\omega_1) \dots E(\omega_n) \times \\ \times \delta(\omega - \omega_1 - \dots - \omega_n)\, d\omega_1 \dots d\omega_n. \end{aligned} \tag{B.6}$$

Delta function appearing in (B.6) enforces conservation of energy.

B.2 Kramers-Kronig

Causality of response functions leads to several properties that are intrinsic to this class of functions. For linear response, from (B.4) follows that $\chi^{(1)}(-\omega) = (\chi^{(1)}(\omega))^*$. For complex values of ω it turns into:

$$\chi^{(1)}(-\omega^*) = (\chi^{(1)})^*(\omega). \tag{B.7}$$

Kramers-Kronig (KK) dispersion relations are the consequence of (B.7). KK connect real and imaginary parts of $\chi^{(1)}$ *via* a Hilbert Transform:

$$Re(\chi^{(1)}(\omega)) = \frac{1}{\pi} \mathcal{P} \int_{-\infty}^{\infty} \frac{Im(\chi^{(1)}(\xi))}{\xi - \omega} d\xi, \tag{B.8}$$

$$Im(\chi^{(1)}(\omega)) = -\frac{1}{\pi} \mathcal{P} \int_{-\infty}^{\infty} \frac{Re(\chi^{(1)}(\xi))}{\xi - \omega} d\xi. \tag{B.9}$$

These are routinely used both in calculations as well as in experimental work, where they are used for optical data inversion, for example for deducing dispersion from absorption spectra.

Analog of (B.7) for general nonlinear case exists for real frequencies

$$\chi^{(n)}(-\omega_1, \dots, -\omega_n) = (\chi^{(n)}(\omega_1, \dots, \omega_n))^*, \tag{B.10}$$

and for some nonlinear processes for complex frequencies. It has been shown that analogs of Kramers-Kroning (B.8,B.9) for nonlinear processes in form of multidimensional Hilbert Transforms do not generally exist. The cases for which they exist include all orders of higher harmonic generation, for which KK takes the following form:

$$Re(\chi^{(n)}(-n\omega; \omega, \dots, \omega)) = \frac{1}{\pi}\mathcal{P}\int_{-\infty}^{\infty} \frac{Im(\chi^{(n)}(-n\omega'; \omega', \dots, \omega'))}{\omega' - \omega} d\omega', \tag{B.11}$$

$$Im(\chi^{(n)}(-n\omega; \omega, \dots, \omega)) = -\frac{1}{\pi}\mathcal{P}\int_{-\infty}^{\infty} \frac{Re(\chi^{(n)}(-n\omega'; \omega', \dots, \omega'))}{\omega' - \omega} d\omega'. \tag{B.12}$$

A further discussion of application of KK relations to nonlinear optics could be found in [107].

B.3 Symmetry Relations

In this section we specialize to the response functions that describe electronic polarization by external electric fields $\vec{E}$. These functions are tensors of $(n+1)$ rank, where n is the order of nonlinearity. Besides symmetry relation (B.10) that follows from causality of Response, there are two other kinds of symmetries: one related to structural symmetry of material and another to permutation properties of response function.

B.3.1 Permutation Symmetries

The most general of permutation symmetries is Intrinsic Permutation Symmetry (IPS). It follows from the fact that one can not distinguish physical order of the fields appearing in expressions of the following form:

$$\chi^{(n)}_{ij_1j_2\dots j_n}(-\omega_\sigma;\omega_1,\omega_2,\dots,\omega_n)E_{j_1}(\omega_1)E_{j_2}(\omega_2)\dots E_{j_n}(\omega_n).$$

From this follows property that allows us to permute indices j_k simultaneously with the corresponding frequency ω_k:

$$\chi^{(n)}_{ij_1j_2\dots j_n}(-\omega_\sigma;\omega_1,\omega_2,\dots,\omega_n)=\chi^{(n)}_{ij_2j_1\dots j_n}(-\omega_\sigma;\omega_2,\omega_1,\dots,\omega_n). \tag{B.13}$$

As a result, number of distinct permutations enters as a factor for the series of equivalent terms in calculations of polarization response. For example, $\chi^{(2)}_{ijk}(-\omega_\sigma;\omega_1,\omega_2)=\chi^{(2)}_{ik_1}(-\omega_\sigma;\omega_2,\omega_1)$ and second order polarization will become:

$$P^{(2)}_i(-\omega_\sigma)=\frac{1}{2\pi\,2!}\sum_{jk}D\int\chi^{(2)}_{ijk}(-\omega_\sigma;\omega_1,\omega_2)\,E_j(\omega_1)E_k(\omega_2)\,\delta(\omega_\sigma-\omega_1-\omega_2)\,d\omega_2,$$

where $D=2$ is a number of distinct permutations of fields $E(\omega)$, 2! - coefficient of Taylor expansion, and 2π is Fourier Transform factor.

In case of lossless media $Im(\chi^{(n)})=0$ and IPS becomes Full Permutation Symmetry (FPS), where all indices can be permuted simultaneously with corresponding frequencies:

$$\begin{aligned}\chi^{(n)}_{ij_1j_2\dots j_n}(-\omega_\sigma;\omega_1,\omega_2,\dots,\omega_n)&=\chi^{(n)}_{j_nj_2j_1\dots i}(-\omega_n;\omega_2,\omega_1,\dots,-\omega_\sigma)=\\&=\chi^{(n)}_{j_1j_2i\dots j_n}(-\omega_1;\omega_2,-\omega_\sigma,\dots,\omega_n).\end{aligned} \tag{B.14}$$

In case of lossles $Im(\chi^{(n)})=0$ and dispersionless media $Re(\chi^{(n)})=const.$ one has Kleinman Symmetry which allows one to permute indices without regard to frequencies:

$$\begin{aligned}\chi^{(n)}_{ij_1j_2\dots j_n}(-\omega_\sigma;\omega_1,\omega_2,\dots,\omega_n)&=\chi^{(n)}_{j_nj_2j_1\dots i}(-\omega_\sigma;\omega_1,\omega_2,\dots,\omega_n)=\\&=\chi^{(n)}_{j_1j_2i\dots j_n}(-\omega_\sigma;\omega_1,\omega_2,\dots,\omega_n).\end{aligned} \tag{B.15}$$

B.3.2 Structural Symmetries

Spatial arrangement of atoms in molecules and solids is frequently symmetric. The point group of material's structural symmetry $\mathcal{S}$ is a finite subgroup of the full symmetry group of Hamiltonian. It can be shown that the related response functions must also possess the same point group. Let $S^{(g)}_{nm}$ be a matrix representing g^{th} element of this group. Since a response function of n^{th} order is a tensor of $n+1$ rank, it transforms according:

$$\chi'^{(n)}_{p\,i\,\ldots,j} = \sum_{s\,k\,\ldots,m} \chi^{(n)}_{s\,k\,\ldots,m} S^{(g)}_{ps} S^{(g)}_{ik} \ldots S^{(g)}_{jm}. \tag{B.16}$$

If the order of the group is N_g then, there exist N_g constraints of type (B.16) that can be used to reduce the number of independent elements. As an illustration consider inversion symmetry that is an element of T_h, O_h and other point groups. Its matrix representation is $S^{(inversion)}_{ij} = -\delta_{ij}$. In case of even order (nonlinear) response function, from (B.16) follows:

$$\chi'^{(2n)}_{p\,i\,\ldots,j} = -\sum_{s\,k\,\ldots,m} \chi^{(2n)}_{s\,k\,\ldots,m} \delta_{ps}\delta_{ik}\ldots\delta_{jm} = -\chi^{(2n)}_{p\,i\,\ldots,j} = 0. \tag{B.17}$$

Therefore even orders of nonlinear response vanish if the material possess inversion symmetry. The tables indicating non-vanishing elements for the first, second and third order response functions for several point groups may be found in [26].

B.4 QFT Response Formalism

To underline the quantum mechanical nature of nonlinear optical response we need to extend the textbook theory of linear response [108] to higher orders. The many-body Hamiltonian is taken in second quantization:

$$\hat{H} = \int d^3x\, \hat{\psi}^\dagger(x)\, T(x)\, \hat{\psi}(x) + \frac{1}{2}\int\!\!\int d^3x\, d^3x'\, \hat{\psi}^\dagger(x)\hat{\psi}^\dagger(x')\, \frac{e}{|\vec{r}-\vec{r'}|}\, \hat{\psi}(x')\hat{\psi}(x) + \hat{H}^{ext} \tag{B.18}$$

where $x = (\vec{x},\, t,\, spin)$, c_k, $c_k^\dagger$ are field creation and annihilation operators, $\psi_k(x)$ are single particle states and $\hat{\psi}$, $\hat{\psi}^\dagger$ are field operators: $\hat{\psi}(x) = \sum_k \psi_k(x)\, c_k$, $\hat{\psi}^\dagger(x) = \sum_k \psi_k^\dagger(x)\, c_k^\dagger$. The external interaction is described in general by $\hat{H}^{ext} = \int d^3x\, \hat{n}(x)\, \phi^{ext}(x)$, where $\hat{n}(x)$ is density operator $\hat{n}(x) = \hat{\psi}^\dagger(x)\hat{\psi}(x)$. Taking external potential as $\phi^{ext}(x) = e\, \vec{r}\cdot\vec{E}(t)$ leads to one of the forms of dipole approximation for photon-electron interaction:

$$\hat{H}^{ext} = e\sum_{ij} \langle i|\, \vec{r}\cdot\vec{E}(t)\, |j\,\rangle c_i^\dagger c_j = \int d^3x\, \hat{\psi}^\dagger(x)\, e\vec{r}\cdot\vec{E}(t)\, \hat{\psi}^\dagger(x) = e\int d^3x\, \hat{n}(x)\, \vec{r}\cdot\vec{E}(t). \tag{B.19}$$

Next, we expand the many-body state vector $|\Psi_S(t)\rangle$ in terms of time ordered products of external interaction $T(H^{ext}(t')\dots H^{ext}(t'^{\dots\prime}))$

$$|\Psi_S(t)\rangle = e^{-\frac{iHt}{\hbar}}\,(1 - \frac{i}{\hbar}\int dt'\, H^{ext}(t') - \frac{1}{2!\,\hbar^2}\int dt'\, dt"\; T(H^{ext}(t')H^{ext}(t")) + \dots)\,|\Psi_S(0)\rangle \tag{B.20}$$

and use it to compute the density fluctuation $\delta\langle\hat{n}(x)\rangle$:

$$\delta\,\langle\hat{n}(x)\rangle = \langle\Psi_S(t)|\hat{n}_S(x)|\Psi_S(t)\rangle - \langle\Psi_S(0)|\hat{n}_S(x)|\Psi_S(0)\rangle = \langle\hat{n}(x)\rangle - \langle\hat{n}(x)\rangle_0. \tag{B.21}$$

We observe that the density fluctuation could be represented as a series with k-th term being a function of k-th power of external potential ϕ^{ext}:

$$\delta\langle\hat{n}(\vec{x},t)\rangle = \sum_k \delta\langle\hat{n}^{(k)}(\vec{x},t;(\phi^{ext})^k)\rangle. \tag{B.22}$$

The non-linear response starts with the second order contribution

$$\delta\langle\hat{n}^{(2)}(x)\rangle = \frac{1}{2!\,\hbar^2}\int d^4x' d^4x"\; \phi^{ext}(x')\phi^{ext}(x")\langle\Psi_S(0)|[[\hat{n}_H(x'),\hat{n}_H(x)],\hat{n}_H(x")]|\Psi_S(0)\rangle. \tag{B.23}$$

Introducing the second order density-density response function $\Xi^{(2)}$

$$\Xi^{(2)}(x;x',x") = \theta(t-t')\theta(t'-t")\frac{\langle\Psi_S(0)|[[\hat{n}_H(x'),\hat{n}_H(x)],\hat{n}_H(x")]|\Psi_S(0)\rangle}{\hbar^2\,\langle\Psi_S(0)|\Psi_S(0)\rangle}, \tag{B.24}$$

the second order density fluctuation could be written as

$$\delta\langle\hat{n}^{(2)}(\vec{x},\omega)\rangle = \frac{1}{4\pi}\int \Xi^{(2)}(\omega;\omega',\omega",\vec{x},\vec{x'},\vec{x"})\phi^{ext}(\omega',\vec{x'})\phi^{ext}(\omega",\vec{x"})\delta(\omega-\omega'-\omega")d^3x'd^3x"\,d\omega'd\omega". \tag{B.25}$$

For the finite systems, such as molecules, we can use the density fluctuation to directly compute polarization $\vec{P}$ (in practice only a change in polarization $\Delta\vec{P}(t)$ is relevant)

$$\vec{P} = \int d^3x\,\vec{x}\,\delta\langle\hat{n}(x)\rangle, \tag{B.26}$$

which could also be written as a series analogous to (B.22) :

$$\vec{P}(t) = \sum_k \vec{P}^{(k)}(t,(E)^k). \tag{B.27}$$

The second term corresponds to the second order nonlinear optical response:

$$\vec{P}^{(2)}(t) = \int d^3x\,\vec{x}\,\delta\langle\hat{n}^{(2)}(\vec{x},t)\rangle = \frac{1}{2!}\int \chi^{(2)}_{ijk}(t;t',t")E_j(t')E_k(t")dt'dt", \tag{B.28}$$

where $\chi^{(2)}_{ijk}$ is the first hyperpolarizability. Fourier transforming (B.28) yields

$$P_i^{(2)}(\omega) = \mathcal{K}\int \chi^{(2)}_{ijk}(\omega;\omega',\omega")E_j(\omega')E_k(\omega")\delta(\omega-\omega'-\omega")d\omega'd\omega", \tag{B.29}$$

where , and $\mathcal{K}$ is factor from Table 2.2. Comparing (B.25) and (B.29) we see that optical susceptibilities could be obtained directly from density-density response function:

$$\chi^{(2)}(\omega;\omega',\omega") = \int \Xi^{(2)}(\omega;\omega',\omega",\vec{x},\vec{x'},\vec{x"})\,\vec{x}\,\vec{x'}\,\vec{x"}\;d^3xd^3x'd^3x".$$

B.5 Diagrammatic Technique for Susceptibilities

In this section we present rules that facilitate drawing pictorial representation of n^{th} order of polarization expansions of type (B.29) and writing down corresponding expressions for matrix elements $\chi^{(n)}_{ij\ldots k}$. This diagrammatic technique is analogous to construction of non-relativistic Feynman Diagrams. The resulting expressions for $\chi^{(n)}$

are essentially the same as those one would obtain from matrix elements of electric dipole operator using wavefunctions calculated to n^{th} order of perturbation theory. For n^{th} order process

1. Draw a (vertical) line. On the line draw $n+1$ vertices.

2. This will partition line into $n+2$ segments. Label first and the last segments with initial $|g\rangle$ and final states $|g'\rangle$. Label remaining segments with intermediate (generally virtual) states: $|m\rangle, |m'\rangle, \ldots$

3. Each vertex corresponds to a matrix element of external potential, that in case of electric dipole interaction becomes $\langle m'|e\, r_j|m\rangle = e\, r^j_{m'm}$. Here r_j is j^{th} Cartesian component of position operator $\hat{r}$. Distribute components over vertices.

4. Draw a (horizontal) arrow in/out of each vertex. Label arrows pointing to vertex with $+\omega$. This corresponds to absorption of photon with energy $\hbar\omega$. Label arrows pointing out of vertex with $-\omega'$. This corresponds to emission of photon with energy $\hbar\omega'$.

5. For each intermediate state $|m\rangle$ write down propagator $\frac{1}{\Delta_{mg}-i\Gamma_{mg}}$ where Δ_{mg} is energy of state $|m\rangle$: $\Delta_{mg} = E_m - E_g + \hbar\sum_i \pm\omega_i$, and Γ_{mg} is line width of $|m\rangle \rightarrow |g\rangle$ transition

6. Write down expression corresponding to the diagram by summing up over all intermediate states m products of $n+1$ vertices with n propagators.

7. Repeat the steps above for all permutations of frequencies ω_i, sum up resulting expressions.

For example, for a second order process that starts at ground state, then absorbs two photons with energies $\hbar\omega_1$ and $\hbar\omega_2$, then emits a photon with energy $\hbar\omega_3 = \hbar(\omega_1+\omega_2)$ and ends at ground state one gets diagram (B.1) with corresponding expression:

$$-\frac{e^3}{\hbar^2}\sum_{mm'}\frac{r^i_{gm}r^j_{mm'}r^k_{m'g}}{(\omega_{gm}+\omega_1+i\Gamma_{gm})(\omega_{gm'}+\omega_3+i\Gamma_{gm'})}. \tag{B.30}$$

Diagrams resulting in permutation of ω_1,ω_2 and ω_3 are shown on diagram (B.2), and the summed expression is

$$\begin{aligned}\chi^{(2)}_{ijk}(-\omega_3;\omega_1,\omega_2) = -\frac{e^3}{\hbar^2}\sum_m\sum_{m'}\Big(&\frac{r^i_{gm}r^j_{mm'}r^k_{m'g}}{(\omega_{gm}+\omega_1+i\Gamma_{gm})(\omega_{gm'}+\omega_3+i\Gamma_{gm'})}+\\
+\frac{r^j_{gm}r^k_{mm'}r^i_{m'g}}{(\omega_{gm}+\omega_1+i\Gamma_{gm})(\omega_{gm'}-\omega_2+i\Gamma_{gm'})}+&\frac{r^k_{gm}r^j_{mm'}r^i_{m'g}}{(\omega_{gm}-\omega_3+i\Gamma_{gm})(\omega_{gm'}-\omega_2+i\Gamma_{gm'})}+\\
+\frac{r^j_{gm}r^i_{mm'}r^k_{m'g}}{(\omega_{gm}+\omega_2+i\Gamma_{gm})(\omega_{gm'}+\omega_3+i\Gamma_{gm'})}+&\frac{r^i_{gm}r^k_{mm'}r^j_{m'g}}{(\omega_{gm}+\omega_2+i\Gamma_{gm})(\omega_{gm'}-\omega_1+i\Gamma_{gm'})}+\\
+&\frac{r^k_{gm}r^i_{mm'}r^j_{m'g}}{(\omega_{gm}-\omega_3+i\Gamma_{gm})(\omega_{gm'}+\omega_1+i\Gamma_{gm'})}\Big).\end{aligned} \tag{B.31}$$

Diagrams with corresponding expressions are useful tool in analysis of various nonlinear processes. However, the expressions obtained are virtually useless for calculations of susceptibilities of real materials. The reason is that it requires summation over an infinite number of states $m, m', \ldots$. These obviously include excited states, which are difficult to obtain for any except very few simple atoms and molecules[2]. Actual application of this technique is known as Sum Over States (SOS) approach, and involves additional approximations. A typical approximation is a truncation of infinite summation to just a few states, sometimes as little as two or three.

---

[2] Hydrogen is one of them

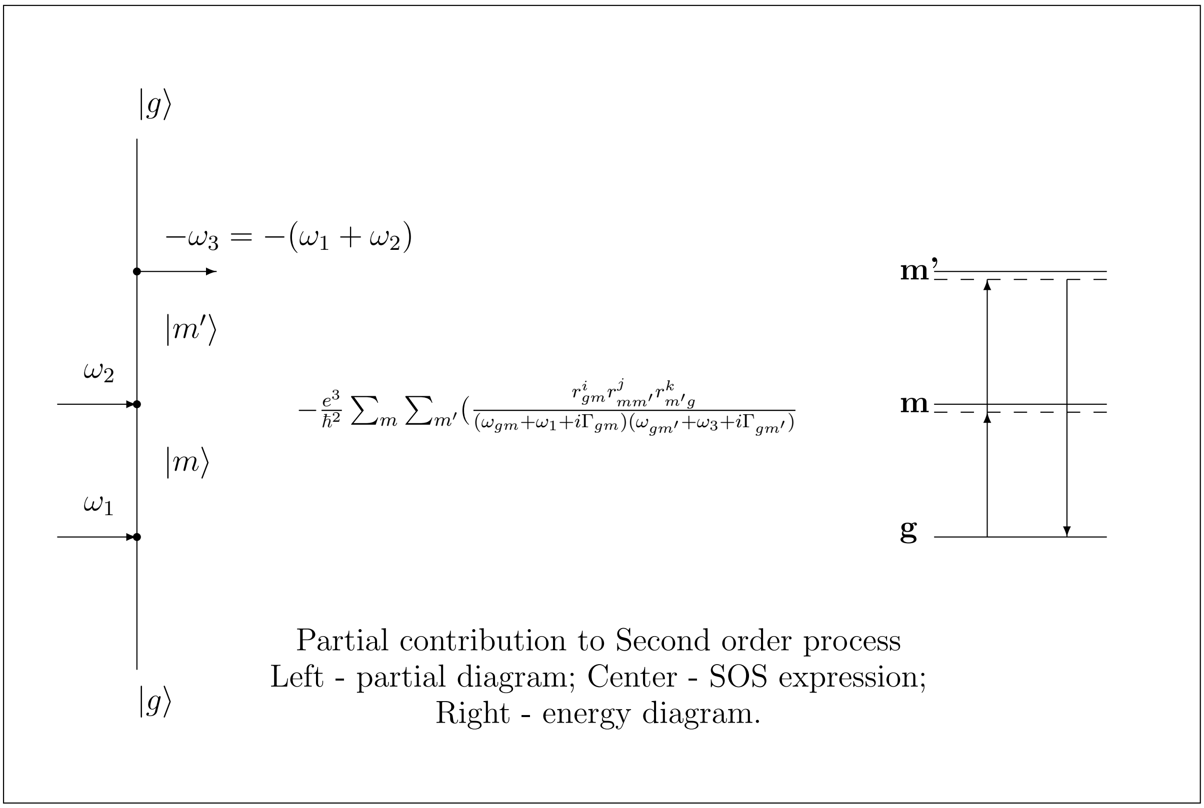

Figure B.1: A partial diagram for second order process: $\chi^{(2)}(-\omega_3; \omega_1, \omega_2)$. $|m\rangle$ and $|m'\rangle$ are virtual states.

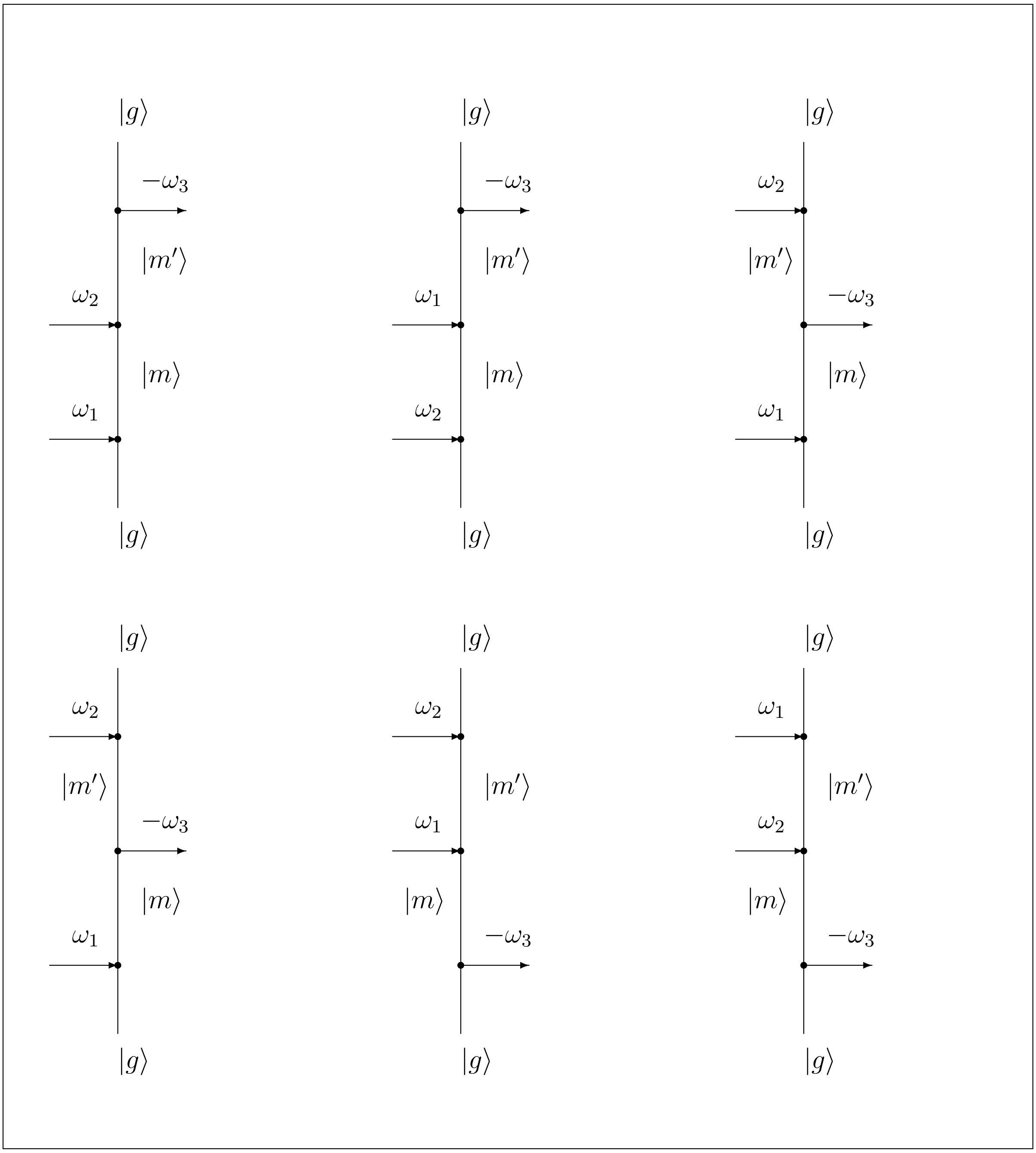

Figure B.2: Non-equivalent Diagrams for second order process: $\chi^{(2)}(-\omega_3; \omega_1, \omega_2)$.

REFERENCES

[1] D. P. Shelton and J. E. Rice, Chem. Rev. **94**, 3 (1994).

[2] J.-I. Iwata, K. Yabana, and G. F. Bertsch, J. Chem. Phys. **115**, 8773 (2001).

[3] Y. Takimoto, *PhD Thesis* (University of Washington, 2008).

[4] P. Salek *et al.*, Mol. Phys. **103**, 439 (2005).

[5] M. D. Levenson and N. Bloembergen, Phys. Rev. B **10**, 4447 (1974).

[6] J. J. Wynne, Phys. Rev. **178**, 1295 (1969).

[7] K. Yabana, T. Nakatsukasa, J.-I. Iwata, and G. F. Bertsch, Phys. Stat. Sol. (b) **243** (2006).

[8] R. van Leeuwen and E. J. Baerends, Phys. Rev. A **49**, 2421 (1994).

[9] X. Andrade, S. Botti, M. A. L. Marques, and A. Rubio, J. Chem. Phys. **126**, 184106 (2007).

[10] V. BonacicKoutecky, L. Cespiva, P. Fantucci, and J. Koutecky, J. Chem. Phys. **98**, 7981 (1993).

[11] N. M. Tam, T. B. Tai, V. T. Ngan, and M. T. Nguyen, J. Phys. Chem. A **117**, 6867 (2013).

[12] E. D. Palik., *Handbook of Optical Constants of Solids* (Elsevier, 1998).

[13] J. D. Pritchard, A. Gauguet, K. J. Weatherill, and C. S. Adams, J. Phys. B **44**, 184019 (2011).

[14] C. Ates, S. Sevinçli, and T. Pohl, Phys. Rev. A **83**, 041802 (2011).

[15] J. D. Pritchard *et al.*, Phys. Rev. Lett. **105**, 193603 (2010).

[16] M.-H. Shih, Nat. Photon. **8**, 171 (2014).

[17] A. Facchetti and et al., Nat. Mater. **3**, 910 (2004).

[18] L. Chen, K. Preston, S. Manipatrini, and M. Lipson, Opt. Express **17**, 15248 (2010).

[19] M. Paniccia, Nat. Photon. **4**, 498 (2010).

[20] H.-T. Chen and et al., Nat. Photon. **3**, 148 (2009).

[21] Y. Enami and et. al., Nat. Photon. **1**, 180 (2007).

[22] Z. L. Samson *et al.*, Appl. Phys. Lett. **96**, 143105 (2010).

[23] C. Videlot-Ackermann *et al.*, Synth. Met. **156**, 154 (2006).

[24] G. T. Reed, G. Mashanovich, F. Y. Gardes, and D. J. Thomson, Nat. Photon. **4**, 518 (2010).

[25] M. Kauranen and A. V. Zayats, Nat. Photon. **6**, 737 (2012).

[26] R. W. Boyd, *Nonlinear Optics* (Elsevier, 2008).

[27] M. Foster, K. Moll, and A. Gaeta, Opt. Express **12**, 2880 (2004).

[28] C. C. Koos and et al., Opt. Express **15**, 5976 (2007).

[29] J. Leuthold, C. Koos, and W. Freude, Nat. Photon. **4**, 535 (2010).

[30] M. Hayden, Nat. Photon. **1**, 138 (2007).

[31] Y. Takimoto, F. D. Vila, and J. J. Rehr, J. Chem. Phys. **127**, 154114 (2007).

[32] K. Yabana, T. Sugiyama, Y. Shinohara, T. Otobe, and G. F. Bertsch, Phys. Rev. B **85**, 045134 (2012).

[33] J. Ducuing and N. Bloembergen, Phys. Rev. Lett. **10**, 474 (1963).

[34] N. Bloembergen, *Nonlinear Optics* (W. A. Benjamin Inc., 1965).

[35] C. Fiolhais, F. Nogueira, and M. Marques, *A Primer in Density Functional Theory* (Springer-Verlag, 2003).

[36] R. Dreizler and E. Gross, *Density Functional Theory: An Approach to the Quantum Many-Body Problem* (Springer-Verlag, 1990).

[37] H. Eschrig, *Fundamentals of Density Functional Theory* (EAG.LE, 2003).

[38] E. Runge and E. Gross, Phys. Rev. Lett. **52**, 997 (1984).

[39] J. P. Perdew and A. Zunger, Phys. Rev. B **23**, 5048 (1981).

[40] S. H. Vosko, L. Wilk, and M. Nusair, Can. J. Phys. **58**, 1200 (1980).

[41] A. Castro, M. A. L. Marques, and A. Rubio, The Journal of Chemical Physics **121**, 3425 (2004).

[42] J. Crank and P. Nicolson, Proc. Camb. Phil. Soc. **43**, 50 (1947).

[43] V. A. Goncharov and K. Varga, J. Chem. Phys. **137**, (2012).

[44] J. R. Chelikowsky, N. Troullier, K. Wu, and Y. Saad, Phys. Rev. B **50**, 11355 (1994).

[45] Y. Saad, J. Chelikowsky, and S. Shontz, SIAM Rev. **52**, 3 (2010).

[46] J. L. Alonso *et al.*, Phys. Rev. Lett. **101**, 096403 (2008).

[47] K. Yabana and G. F. Bertsch, Phys. Rev. A **60**, 3809 (1999).

[48] V. V. Kresin, Phys. Rev. B **51**, 1844 (1995).

[49] J. Tiggesbäumker, L. Köller, K.-H. Meiwes-Broer, and A. Liebsch, Phys. Rev. A **48**, R1749 (1993).

[50] K. Nobusada and K. Yabana, Phys. Rev. A **70**, 043411 (2004).

[51] M. L. Tiago, J. C. Idrobo, S. Öğüt, J. Jellinek, and J. R. Chelikowsky, Phys. Rev. B **79**, 155419 (2009).

[52] H. Ehrenreich and H. Philip, Phys. Rev. **128**, 1622 (1962).

[53] K. Baishya *et al.*, Phys. Rev. B **78**, 075439 (2008).

[54] P. B. Johnson and R. W. Christy, Phys. Rev. B **6**, 4370 (1972).

[55] G. Mie, Ann. Phys. **25**, 377 (1908).

[56] R. Gans, Ann. Phys. **37**, 881 (1912).

[57] D. Lu, G. Chen, and W. A. Goddard, J. Chem. Phys. **101**, 4920 (1994).

[58] M. Chandross, Y. Shimoi, and S. Mazumdar, Phys. Rev. B **59**, 4822 (1999).

[59] N. Troullier and J. L. Martins, Phys. Rev. B **43**, 1993 (1991).

[60] D. E. Aspnes, Phys. Rev. B **6**, 4648 (1972).

[61] D. J. Moss, E. Ghahramani, J. E. Sipe, and H. M. van Driel, Phys. Rev. B **41**, 1542 (1990).

[62] E. Ghahramani, D. J. Moss, and J. E. Sipe, Phys. Rev. B **43**, 8990 (1991).

[63] J. E. Sipe and E. Ghahramani, Phys. Rev. B **48**, 11705 (1993).

[64] Z. H. Levine, Phys. Rev. B **49**, 4532 (1994).

[65] A. Dal Corso and F. Mauri, Phys. Rev. B **50**, 5756 (1994).

[66] C. Aversa and J. E. Sipe, Phys. Rev. B **52**, 14636 (1995).

[67] J. E. Sipe and A. I. Shkrebtii, Phys. Rev. B **61**, 5337 (2000).

[68] E. Luppi, H. Hübener, and V. Véniard, Phys. Rev. B **82**, 235201 (2010).

[69] H. Hübener, Phys. Rev. A **83**, 062122 (2011).

[70] C. Attaccalite, M. Grüning, and A. Marini, Phys. Rev. B **84**, 245110 (2011).

[71] X. Gonze, P. Ghosez, and R. W. Godby, Phys. Rev. Lett. **74**, 4035 (1995).

[72] G. Ortiz, I. Souza, and R. M. Martin, Phys. Rev. Lett. **80**, 353 (1998).

[73] G. F. Bertsch, J.-I. Iwata, A. Rubio, and K. Yabana, Phys. Rev. B **62**, 7998 (2000).

[74] A. D. Corso, F. Mauri, and A. Rubio, Phys. Rev. B **53**, 15638 (1996).

[75] R. D. King-Smith and D. Vanderbilt, Phys. Rev. B **47**, 1651 (1993).

[76] Y. Shinohara *et al.*, Phys. Rev. B **82**, 155110 (2010).

[77] G. H. Wannier, Rev. Mod. Phys. **34**, 645 (1962).

[78] N. T. Maitra, T. N. Todorov, C. Woodward, and K. Burke, Phys. Rev. A **81**, 042525 (2010).

[79] K. Yabana and G. F. Bertsch, Phys. Rev. B **54**, 4484 (1996).

[80] J. R. Chelikowsky, N. Troullier, and Y. Saad, Phys. Rev. Lett. **72**, 1240 (1994).

[81] M. P. Teter, M. C. Payne, and D. C. Allan, Phys. Rev. B **40**, 12255 (1989).

[82] Y. P. Deng and et. al., Opt. Express **13**, 3096 (2005).

[83] K. Varga, Z. Zhang, and S. T. Pantelides, Phys. Rev. Lett. **93**, 176403 (2004).

[84] E. L. Briggs, D. J. Sullivan, and J. ¡Bernholc, Phys. Rev. B **54**, 14362 (1996).

[85] T. L. Beck, Rev. Mod. Phys. **72**, 1041 (2000).

[86] A. Tsolakidis, D. Sánchez-Portal, and R. M. Martin, Phys. Rev. B **66**, 235416 (2002).

[87] K. Varga, Phys. Rev. B **in press** (2009).

[88] T. Ozaki and H. Kino, Phys. Rev. B **69**, 195113 (2004).

[89] J. Junquera, O. Paz, D. Sánchez-Portal, and E. Artacho, Phys. Rev. B **64**, 235111 (2001).

[90] V. Blum *et al.*, Comp. Phys. Comm. **180**, 2175 (2009).

[91] O. F. Sankey and D. J. Niklewski, Phys. Rev. B **40**, 3979 (1989).

[92] M. Gusso, J. Chem. Phys. **128**, 044102 (2008).

[93] K. Yabana and G. F. Bertsch, Phys. Rev. B **54**, 4484 (1996).

[94] M. A. L. Marques, A. Castro, G. F. Bertsch, and A. Rubio, Comp. Phys. Comm. **151**, 60 (2003).

[95] cp2k development group, cp2k.berlios.de/ (2010).

[96] Y. Fu, K. A. Chao, and R. Osório, Phys. Rev. B **40**, 6417 (1989).

[97] G. Kodis, P. A. Liddell, A. L. Moore, T. A. Moore, and D. Gust, J. Phys. Org. Chem. **17**, 724 (2004).

[98] S. Saha, A. H. Johansson, E.and Flood, H.-R. Tseng, J. I. Zink, and J. F. Stoddart, Chem. Eur. J. **11**, 6846 (2005).

[99] N. Spallanzani and et. al., J. Phys. Chem. B **113**, 5345 (2009).

[100] C. Jamorski, M. E. Casida, and D. R. Salahub, J. Chem. Phys. **104**, 5134 (1996).

[101] V. Fock, Z. fr Phys. **61**, 126 (1930).

[102] D. R. Hartree, Proc. Cambr. Phil. Soc. **24**, 328 (1928).

[103] J. C. Slater, Phys. Rev. **91**, 528 (1953).

[104] J. C. Slater, *Quantum Theory of Molecules and Solids* (McGraw-Hill, 1974).

[105] W. Kohn and L. J. Sham, Phys. Rev. **140**, A1133 (1965).

[106] L. Treffethen and D. Bau, *Numerical Linear Algebra* (SIAM, 1997).

[107] K.-E. Peiponen and J. J. Saarinen, Rep. Prog. Phys. **72**, 056401 (2009).

[108] A. Fetter and J. Walecka, *Quantum Theory of Many-Particle Systems* (McGraw-Hill, 1971).